Growth and Characterisation of Thin Films of CuCl and Related Materials

by

Barry Foy

B.Sc in Applied Physics

School of Physical Sciences

Dublin City University

A thesis submitted for the degree of

Doctor of Philosophy

to

Research Supervisor

Dr. Enda McGlynn

I hereby certify that this material, which I now submit for assessment on the programme of study leading to the award of Doctor of Philosophy is entirely my own work, that I have exercised reasonable care to ensure that the work is original, and does not to the best of my knowledge breach any law of copyright, and has not been taken from the work of others save and to the extent that such work has been cited and acknowledged within the text of my work.

Signed: ____________ (Candidate)   ID No.: 52021692

Date: _______

Abstract

Growth and Characterisation of Thin Films of CuCl and Related Materials

Barry Foy

CuCl thin films grown on (100) Si by thermal evaporation are studied by means of low temperature photoluminescence (PL) and reflectance spectroscopies. Spatially and wavelength resolved room temperature cathodoluminescence (CL) imaging of the surface of the CuCl samples in a scanning electron microscope (SEM) has also been performed.

Investigation of the effect of mixing KCl with the CuCl has been performed. The samples produced by the liquid phase epitaxy (LPE) machine use this element to lower the boiling point of CuCl so it is important to understand the effect they have on the resultant thin films. P-type doping has also been performed with oxygen.

Characterisation of these doped and undoped γ-CuCl samples has been performed. Reflectance and X-ray diffraction measurements show the effect the oxygen doping has on the structural and optical properties of the material. The exciton positions in the undoped samples have been repeatable, but deteriorate as oxygen doping levels increase. A suitable capping method for use in x-ray diffraction has been found. Nail varnish applied to the samples was shown to prevent structural decay of the CuCl thin films due to their hygroscopic nature.

Cathodoluminescence work on undoped and doped samples (doped with both oxygen and KCl) has been performed showing the effect of these techniques on the electrical properties. Digital CL has also been performed, but with limited results due to the low resolution of the digital CL camera.

EDX has been used to analyse the atomic structure of the thin film samples. Traces of K were found in the KCl-CuCl samples with little change in the Cl levels. This gives further credence to the idea that the K^+ atom within the material is responsible for the increase in conductance produced by KCl doping.

The Reflectance of the various CuCl samples was tested at different angles of incidence using a Deuterium light source. The reflectance spectra are modelled using a dielectric response function with various models involving dead layers and reflected waves in the thin film and the exciton-polariton structure obtained is compared to other studies of CuCl. The modelling is shown to match the experimental data quite well with the dead layer having little effect on the modelled spectra. KCl-CuCl samples prove to have a consistently higher reflectance signal than undoped CuCl.

Photoluminescence (PL) tests of doped CuCl reveal the emergence of an unknown peak centred at 3.187 eV. This peak has not been previously identified to the best of our knowledge and steadily increases to become the maximum in the PL spectrum as doping levels are increased. A combination of PL and reflectance scans have been used to locate an ideal doping level which provides p-type doping attribute of CuCl without a corresponding significant decrease in the optical properties. This ideal region is between 3-4 minutes of exposure at the settings detailed herein.

Acknowledgements

There are a number of people I'd like to thank for their input and support throughout this Ph. D. Without the contributions of every single one of these fine people, the completion of this thesis in its current format would not have been possible.

I would like to express my sincere gratitude to my supervisor, Dr. Enda McGlynn for his guidance and encouragement throughout the process of this research. Had it not been for the level of his knowledge, the amount of his support and having the depth of his experience to draw on, none of this work would have been possible.

Although a great deal of this work concerned the exploration of the CuCl material, I am indebted to the previous CuCl researchers in the NPL who established most of the procedures for deposition and investigation. Therefore I owe Dr. Lisa O'Reilly and Dr. Francis Olabanji Lucas a great deal of thanks for laying the foundations upon which my work can build upon. During this process, I am also grateful for working alongide fellow CuCl enthusiasts, Rajani, Monjarul and Aidan. Of these I owe Dr. Aidan Cowley even more kudos, clearing his schedule and donating his time to supervise the acid etching process during sample preparation which was suitably enlivened with his scientific banter.

To my fellow postgraduates I owe gratitude for their laboratory assistance and the discussion they provided which helped to shape my ideas. In this regard I would like to thank the ZnO group including my ex-officemate Dr. Mahua Biswas, Dr. James Fryar, Dr. Daragh Byrne, Joe Cullen, Seamus Garry and Ruth Saunders. I'd also like to thank the other postgraduates who have provided mental support such as John Beggan, Dr. Justin Bogan, Dr. Paddy Casey, Dr. Patrick Kavanagh, Conor Coyle and Dr. Vincent Richardson.

To my friends I owe my sanity and my thanks for enduring numerous rants at each of the various obstacles along the road to this doctorate without complaint!

To my girlfriend Órla, thank you for always being there with love and support, your understanding and compassion were the perfect companion throughout this adventure.

To my family; my sister Sinéad for being a constant source of witty banter and memes, despite her resistance to the field of science. Finally my mother Brigid and my father Desmond I am eternally grateful to. Without both of your love, support and belief in me, the endeavors throughout my life would have born little fruit. To both of you, I dedicate this thesis.

Table of Contents

Declaration i

Abstract ii

Dedication iii

Table of Contents v

List of Publications viii

Chapter 1 Introduction and Overview

1.1 Introduction 1

1.2 Wide Band Gap Materials 3

1.3 Previous research on CuCl 6

1.4 Physical Properties of CuCl 9

1.5 Electronic Properties of CuCl 12

1.6 Structure of thesis 16

Chapter 2 Methods of Characterisation

2.1 Introduction 20

2.2 Sample Preparation 20

2.2.1 Thermal Evaporation Deposition 21

2.2.2 Oxygen Doping of CuCl thin films 25

2.2.3 Liquid Phase Epitaxy 26

2.3 Structural analysis – X-Ray Diffraction 28

2.4 Optical properties

2.4.1 Photoluminescence 37

2.4.2 Fourier Transform Equipment 46

2.4.3 Reflectance 54

2.5 Electrical properties

2.5.1 Scanning Electron Microscopy 57

2.5.2 Cathodoluminescence SEM (CL-SEM) Imaging 61

2.5.3 Energy Dispersive X-Ray Diffraction 67

2.6 Summary 69

Chapter 3 Structural Properties

3.1 Introduction 73

3.2 XRD Measurements on the System Base Plate 74

3.3 CuCl Sample Composition 76

3.4 KCl Sample Composition 81

3.5 Protective Varnish Layer 84

3.6 CuCl Thin Film Samples 88

3.7 Glancing Angle X-Ray Diffraction 94

3.8 CuCl – KCl Samples 98

3.9 Decayed samples of CuCl and KCl 101

3.10 Oxygen Doping of CuCl 102

3.11 Summary 105

Chapter 4 CL and EDX imaging in the SEM

4.1 Introduction 108

4.2 Cathodoluminescence Results 109

4.3 KCl Samples 117

4.4 Oxygen Doping 120

4.5 EDX Imaging 123

4.6 Summary 130

Chapter 5 Optical Properties

5.1 Introduction 134

5.2 Photoluminescence

5.2.1 Undoped CuCl Photoluminescence 135

5.2.2 KCl-CuCl PL Analysis 141

5.2.3 Oxygen Doping PL Analysis 143

5.3 Reflectance Analysis

5.3.1 CuCl and KCl-CuCl Undoped samples 146

5.3.2 Oxygen Doping of CuCl and KCl-CuCl 150

5.4 Reflectance Modelling

5.4.1 Introduction 153

5.4.2 Model 1 (Air – Bulk CuCl) 159

5.4.3 Model 2 (Air – DL – CuCl) 161

5.4.4 Model 3 (Air – CuCl – Si) 161

5.4.5 Model 4 (Air – DL – CuCl – DL – Si) 163

5.4.6 Modelling Results 165

5.5 Summary 173

Chapter 6 Conclusion and Further Work

6.1 Conclusion 177

6.2 Further Work 180

References 184

Appendices

Appendix: Modelling Program for Reflectance 190

List of Publications

1. B. Foy, E McGlynn, A Cowley, P. J. McNally, MO Henry, *Spatially Resolved Investigation of the Optical and Structural Properties of CuCl Thin Films on Si.* AIP Conference Proceedings, 2010. **1292**(1): p. 209-212.

2. A. Cowley, B Foy, D Danilieuk, P. J. McNally, A. L. Bradley, E. McGlynn, A. N. Danilewsky. *UV emission on a Si substrate: Optical and structural properties of gamma-CuCl on Si grown using liquid phase epitaxy techniques.* physica status solidi (a), 2009. **206**(5): p. 923-926.

3. D. Danieluk, A. L. Bradley, A. Mitra, L. O'Reilly, O. F. Lucas, A. Cowley, P. J. McNally, B. Foy, E McGlynn. *Optical properties of undoped and oxygen doped CuCl films on silicon substrates.* Journal of Materials Science-Materials in Electronics, 2009. **20**: p. 76-80.

4. B.Foy, E. McGlynn. *Study of exciton-polariton modes in nanocrystalline thin films of CuCl using reflectance spectroscopy.* Manuscript in preparation.

1.1 Introduction

Recent years have seen the use of semiconductor devices in society expand thanks to the utilisation of both new applications and new materials. Wide band gap materials have been studied extensively for a range of applications such as UV light emitting diodes, diode lasers and detectors [1]. Light-emitting diodes (LEDs) have driven the progress in this area due their low-cost, the low-energy required to operate and their increasingly ubiquitous presence throughout modern society. Everything from home lighting to televisions now incorporates some form of LED technology. Similarly the pursuit of laser diodes (LDs) operating at energies of > 3 eV is an important one as the density of optical storage in optical disc systems increases as the wavelength of laser light is decreased [2]. To date LDs using semiconductor materials such as InGaN and GaAlAs have been implemented in technology as diverse as Blu-ray DVD Players, laser printers and even in medicine for soft tissue procedures involving homeostasis of the blood [3, 4].

This implementation of GaN material across multiple devices is the model to which competing materials aspire. ZnO in particular has seen a large level of research as one of the potential replacements for GaN, with one recent development being the increase in LED brightness by up to 400% through the use of ZnO nanowires [5].

This thesis concerns another semiconductor material, CuCl, and contains a detailed exploration of the properties of thin film samples of CuCl deposited to (100) Si substrates and the effects of doping on these characteristics. Unlike the other semiconductor materials mentioned, there is an absence of completed semiconductor devices using CuCl. The research is at an earlier stage due to a lack of interest until recent years and discussed further within this chapter. The key advantage CuCl offers compared to GaN, ZnO and other materials is its close lattice matching with Si. This causes a more uniform growth to occur at the Si-CuCl boundary leading to a reduction in the number of defects present. In optoelectronic devices defects effect the output from the circuit causing unexpected conductivity levels and affecting the light emission [6]. Therefore lower defect levels will lead to more reliable devices with reproducable results and ultimately an end product which is both cheaper and easier to manufacture.

Having completed a brief overview of the current optoelectronic research state and identified the main competing materials (GaN, ZnO and CuCl), this chapter will continue with a more detailed examination each of the competing wide band gap materials. In particular their physical properties and advantages/disadvantages as optoelectronic devices. This is followed by a detailed discussion of the previous research performed on CuCl before delving into the theory in the form of the physical and electronic properties of CuCl itself. Finally the chapter concludes with a summary of the thesis structure, briefly outlining each of the awaiting chapters of this work.

1.2 Wide Band Gap Materials

In this area of semiconductor research, most of the research to date has focused on III-nitride and II-VI material systems, with the former being the most productive for applications thus far. This section examines the forerunners for each of these systems, GaN for the III-nitride and ZnO for the II-VI. For comparison and reference, some of the key physical properties of each of the materials under discussion are shown in table 1.1.

A fundamental problem with the III-nitride system of GaN is the large lattice mismatch (~ 13% [7]) between GaN epitaxial layers and suitable substrates (e.g. SiC, α-Al_2O_3). This results in high levels of defect densities, in particular threading dislocations (TDs) of the order 10^8 cm^{-2} [8]. These dislocations and other defects have a drastic effect on the lifetime and performance of any prospective devices and stem from the residual biaxial compression caused by the lattice mismatch [9]. For comparison, homoepitaxially grown GaAs typically has a TD density of the order 10^2 – 10^4 cm^{-2} and homoepitaxial Si almost none [10].

Several different growth techniques have helped to reduce the dislocation density in GaN and related materials systems. Epitaxial lateral overgrowth (ELOG) [11], pendeo-epitaxial growth [12] and slight variations on these two procedures provide the most successful route to reduction of the density of TDs in GaN (on its most favourable substrate Al_2O_3) to date. ELOG is a two-step growth process where the highly dislocated GaN within the initial buffer layer is covered with a dielectric mask and selective area epitaxy performed on the uncovered area. This ensures the dislocated GaN cannot propagate within further layers which grow laterally over the mask and can reduce the TD density to the order of 10^7 cm^{-2} [13, 14]. Pendeo-epitaxy

Properties	CuCl	ZnO	GaN
Optical Band Gap (eV)	3.399	3.44	3.503
Exciton Binding Energy (meV)	190	63.1	26
Lattice Constant (nm)	0.541	0.3249	0.319
Mismatch to Si (%)	< 0.4	15	17
Structure	Zincblende	Hexagonal	Hexagonal
Melting Point (°C)	422	1975	> 2500
Boiling Point (°C)	1490	2360	N/A

Table 1.1 *Some of the characteristics of various wide band gap semiconductor materials [15]*

is an extension of this where the substrate itself is employed as a pseudo-mask with growth beginning in the sidewalls of microstructures etched into the surface of an initial GaN seed layer. This growth is continued until there is a consolidation of the material above these walls resulting in low defect density material as it is building upon a solid base of low defect material. The density is similar to that produced by ELOG, but pendeo-epitaxy is a simpler process [12]. Whilst these processes continue the reduction of the presence of TDs it still remains of the order 10^7 cm^{-2}. Although a significant figure, this has not prevent the production of GaN LDs, merely effected their performance and lifespan. The additional steps taken to reduce TDs also significantly increase the cost of the substrates and growth processes, limiting the appeal of such material and paving the way for a cheaper more reliable alternative.

One potential replacement is ZnO. This material is II-VI type and has some significant advantages over GaN such as its availability in bulk, single-crystal form and its larger binding energy (63.1 meV compared to GaN's 26 meV) and its wide direct band gap of 3.44eV [15]. In the last ten years there have been significant

improvements in the quality and the control of bulk and epitaxial ZnO which has increased the interest in the use of this material in the optoelectronics industry with its wide bandgap making it a candidate host for solid state blue to UV optoelectronics, including laser development. It has been demonstrated that the bandgap of ZnO is tunable down to ~3.0 eV by Cd substitution and up to ~4.0 eV by Mg substitution [16]. However to date homoepitaxial growth on ZnO bulk substrates has proved quite difficult and for hetero-epitaxy, similar to the problems of GaN, the lattice mismatch of ZnO with the target substrates leads to a significant number of threading dislocations within the ZnO thin films [17]. These problems are compounded by the fact that it has been impossible to achieve reproducible p-type doped ZnO samples [18]. Each of these factors contributed to the earlier production and proliferation of GaN optoelectronic devices.

This brings us to CuCl a I-VII type material. CuCl is in possession of some very competitive material properties and does not suffer from the same issues of lattice mismatch and thus offers the possibility of lattice-matched and TD-free growth on Si without the need for techniques such as ELOG and pendeo-epitaxy to reduce TD presence. Furthermore, CuCl is closely lattice-matched to both Si and GaAs and is an ideal candidate for the development of hybrid electronic-optoelectronic platforms. The optical properties of CuCl thin films, their detailed understanding and optimization, are therefore key to realizing the potential uses of this material in optoelectronic devices and comprise the main content of this thesis.

1.3 Previous research on CuCl

In the 1960's, 1970's and early 1980's the optoelectronic properties of CuCl were studied as part of a general broad-based effort in the study of potential lasing materials [19-24]. This work set the stage in terms of the underlying material properties for further work in the more recent past. As we can see from figure 1.1, there was somewhat of a stagnation or lull in activity (or at least rate of increase of activity) on CuCl after the early to mid-1980s as attention switched to III-V materials and quantum well structures.

Figure 1.1 also shows in the last twenty years a renewed interest in CuCl and related materials emerged and much of the more recent research on copper halides has focussed on a number of different areas due to interest generated in the late nineties by the large excitonic binding energies (190 meV for CuCl and 108 meV for CuBr)

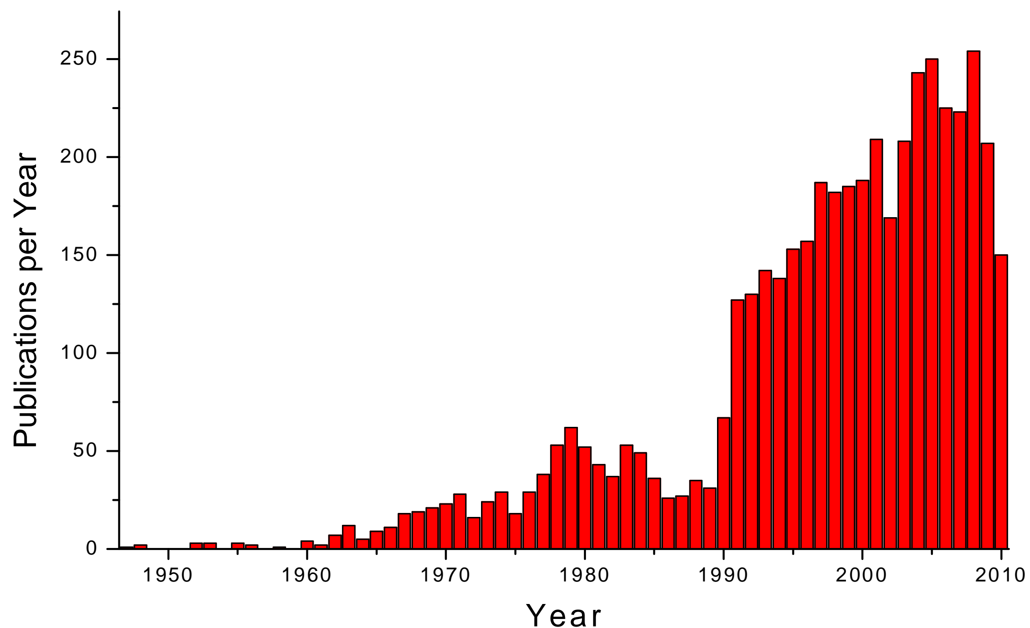

Figure 1.1 *Graph showing the number of publications per year under the topic CuCl or Copper Chloride [25]*

compared to those of group III-V and II-VI semiconductors [26]. Binding energies of such magnitude further lead to advantages in the observation of multi-exciton effects under intense excitation due to the high stability of the exciton itself. The formation of exciton molecules or biexcitons is a phenomenon typical of intense excitation effects meaning that the copper halides are ideal for investigations into the behaviour of e.g. biexcitons. Spectroscopic and theoretical studies of this excitonic behaviour and the band structure in the copper halides have been undertaken using a simpler method of band structure calculation [27] and applying different methods of characterisation to analyze the lattice modes within CuCl and CuBr at both high and extremely low temperatures [28].

Due to the quantum size effect on electrons and holes, semiconductor quantum dots are expected to show distinctive optical properties such as super-radiance and enhancement of optical nonlinearities which may have application in optical devices [29]. Studies performed in 2000 on CuCl quantum dots on both glass matrices [29, 30] and NaCl [31, 32] discovered many interesting properties: a blue shift in the positions of the $Z_{1,2}$ and Z_3 excitons, the first observation of photostimulated luminescence (PSL) in CuCl quantum dots, the temperature dependence of the broadening of the homogenous exciton spectral linewidth and the formation of nonlinear layers attributed to the migration of the Cu^+ and Cl^- ions. Experiments with CuCl quantum dots had been previously performed in the late 1980s and the optical properties investigated [33, 34], particularly the aforementioned exciton linewidth broadening [35, 36]. However some of these samples were prepared by a liquid-phase synthesis where the CuCl is dissolved in molten glass or NaCl which allows surface atoms of the microcrystals to react with impurities which can hinder the

validity of the intrinsic optical properties of the CuCl material itself due to the interference from the impurities in question.

Surface studies of the growth mechanisms involved in the heteroepitaxy of CuCl single crystals on a number of different substrates such as MgO (001) and CaF_2 (111) [37] and the reconstructed surface of α-Fe_2O_3 (0001) haematite [38] were also performed in this period. These studies showed the preferential epitaxial growth with (111) texture of the CuCl layer which matched previous studies using the molecular beam epitaxy (MBE) method of growth on MgO (001) [39]. Heteroepitaxial growth of CuCl on both Si and GaAs structures was also examined by one group of researchers in 1995 [40] by MBE. Rather than pursue the possible use of CuCl as a light emitter or for other applications, this study focussed on the fundamental physics of the island growth processes and the nature of the interfacial bonding at the CuCl/GaAs and CuCl/Si interfaces.

There has been relatively little previous work on growth of CuCl on Si substrates. One group of researchers, Inoue et al [41], found that in a growth containing CuCl and KCl the precipitation of CuCl out of the melt occurred below the phase transition temperature. This was an important development for the evaporation of CuCl on Si as there is a known reaction between CuCl and Si at 250˚C [42] and the melting temperature of CuCl is 422˚C [15] so for any kind of liquid phase epitaxy (LPE) to occur the melting temperature issue would have to be dealt with. However at the time this opportunity for LPE growth was never explored in detail.

Doping of CuCl to influence its properties has also not received much attention from researchers prior to the work of our group in DCU. Previously, the main focus was the doping of KCl films with Cu to determine the off-centre position of Cu^+ ion impurities within the lattice of alkali halides [43, 44], to examine their potential

development as ultra-violet (UV) absorbing optical filters [45] and to investigate the band structure changes, density and liquid phase properties of KCl-CuCl melts [46].

The proposal for CuCl growth on Si and its possible use in optoelectronics in 2005 [47] and associated recent papers published by the group within DCU on n-type doping [48] and LPE growth systems both concerning thin films on Si [49] appear to be the first of their kind. Because of the very recent development and interest in such thin film CuCl samples on Si and their potential for doping, and the lack of much previous work, there is consequently an element of open-ended exploration involved in this research topic. This is manifested within this work by the structure of this thesis, discussed in the next section. Much of these techniques and methods have already been previously explored for other semiconductor materials, but this is not the case with CuCl due to the previous low level of interest in this material. Investigating previously pursued avenues of research with updated techniques and characterisation methods applied to this new material allows us to build upon existing knowledge in this previously less popular field which is the principle the majority of work in this thesis is based upon.

1.4 Physical Properties of CuCl

CuCl is a cuprous halide and a wide, direct bandgap (energy gap between the valence and conduction band at 2K is 3.3990eV [15]) highly ionic I-VII compound (compared to other materials already mentioned, e.g. GaN, ZnO and the other copper halides) with a cubic zinc-blende lattice structure at room temperature. As temperature is increased the zinc-blende structure undergoes a phase transition to the wurtzite structure. This transition occurs at ~407˚C [47] slightly before the material's melting

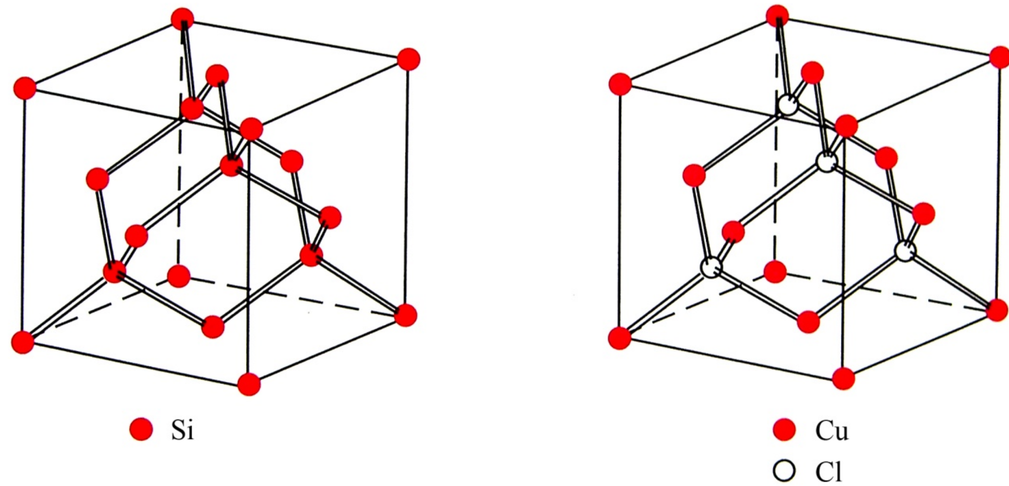

Figure 1.2 *(a) Diamond structure of Si. (b) Cubic Zincblende Lattice structure of CuCl. The red atoms represent Cu, the white Cl [50]*

point. The cubic zinc-blende lattice is comprised of two interpenetrating face-centred-cubic (FCC) unit cells occupied by Cu and Cl. As we can see in figure 1.2, the structure is equivalent to that of the diamond-like structure of Si except that Si has the same atom at each lattice point. Each of the atoms in the lattice is surrounded by a tetrahedron consisting of four atoms of the other element in the compound (i.e. Cu is surrounded by four atoms of Cl, whilst Cl is surrounded by four atoms of Cu). The distance between these atoms is $\frac{a\sqrt{3}}{4}$ where a is the lattice constant. The difference between the lattice constant of CuCl (0.541 nm) and Si (0.543 nm) is only ~0.4% at room temperature [40]. This is much closer to Si than other compounds used in optoelectronic devices such as GaN (with a mismatch of ~17%, see table 1.1 for a comparison of other values).

It is hoped that by using this low lattice mismatch one may avoid the high dislocation densities which reduce the emission lifetime and reliability problems of Group III nitrides on Si. However, there is a large difference in the coefficients of

thermal expansion of CuCl and Si (these being 13.8×10^{-6} K^{-1} [51] and 2.6×10^{-6} K^{-1} [52], respectively at room temperature). This difference might cause difficulties for stress-free lattice-matched growth, but the potential effect of this difference on the heteroepitaxial growth of CuCl on Si is reduced due to the aforementioned low melting point of CuCl, which limits the possible range of growth temperatures for epitaxial growth.

Furthermore, the melting point of CuCl is ~422 ºC and its boiling point is ~1490 ºC [53] while the melting point of Si is 1414 ºC. In liquid phase epitaxy (LPE), if the melting point of the material being deposited is close to the melting point of the substrate this can lead to warping effects in the resultant thin films. But with such a significant difference between their melting points it would appear that CuCl is an excellent candidate for deposition on Si via LPE (LPE is discussed in more detail in Chapter 2.1.2). Thus CuCl appears in many respects to be a strong candidate with potential for LPE lattice-matched growth on Si substrates.

As well as a wide direct bandgap CuCl also has a large exciton binding energy (190 meV for the Z_3 exciton) which is much larger than those of III-V (e.g. GaN = 26 meV [15]) and II-VI (e.g. ZnO = 63.1 meV [15]) semiconductors [26]. Such a large exciton binding energy means that excitonic species (including free and bound excitons) will be stable at room temperature and above. Excitonic transitions are efficient radiative transitions compared to band to band transitions due to the strong overlap of electron and hole wavefunctions in the bound pair state and thus the interaction of CuCl with photons (absorption and emission) is expected to be very strong up to room temperature and beyond. Furthermore, the stability of the free exciton also influences the stability and hence the observation of multi-exciton molecules (e.g. so-called biexcitons, the binding energies of which in CuCl are

34meV) and these species are of interest for e.g. quantum computing and photon entanglement experiments [54, 55].

Oxidation of CuCl occurs at a similar rate to that of Cu, with the Cu and Cl having oxidation numbers of +1 and -1 respectively. However, instead of oxygen exposure the main practical materials drawback of CuCl is its strongly hygroscopic nature [56]. The material will degrade in an atmosphere containing water vapour (i.e. in normal ambient) and this degradation proceeds via the formation of hydrated oxyhalides of Cu^{++} which can be recognized by the greenish colour of the Cu^{++} ions. This degradation of the sample can have a drastic effect upon the structure of the thin film with a large change observed in optical and other properties (e.g. a decrease in the intensity of optical reflectance and cathodoluminescence (CL) signals and changes in structural properties as evidenced by X-ray diffration (XRD) scans) for any samples left exposed in ambient for a significant length of time. It is therefore imperative that raw CuCl powder and thin film samples of CuCl are stored inside an evacuated chamber or a chamber filled with a dry gas other than natural air (i.e. helium) or that the surface is treated in order to prevent this effect. For example, most of the CuCl powder used in the thin film deposition process to be described later was transported to DCU inside a glass ampoule which was shattered to access the powder within, thus ensuring an airtight seal during transit.

1.5 Electronic Properties of CuCl

The electronic band structure of CuCl is quite unique in comparison to other semiconductor compounds. As CuCl is a I-VII semiconductor, the valence bands originate from the full d^{10} shell of the positively charged metal ions and the s^2p^6 gas

configuration of the negatively charged halogen ions [22, 57]. We can see this from the electronic configurations of the constituent atoms; Cu is [Ar] $3d^{10}$ $4s^1$ and Cl [Ne] $3s^2$ $3p^5$. In III-V and II-VI compounds the valence bands also originate from a s^2p^6 configuration but with metal d-levels of much lower energy meaning a much smaller interaction with the s^2p^6 valence levels which dominate the topmost valence bands. This is in contrast to CuCl and other I-VII compounds where the energy range of the d-level is quite large and much closer to the p-levels of the halogen (Cl). This has the effect of hybridising the p-levels of Cl with the d-levels of Cu in the upper valence bands which significantly alters the electronic and other properties of these compounds. In more detail, upon CuCl bond formation, the loosely bound s orbital passes from Cu to the Cl atom. This leaves the Cu with a completely filled outer d shell and the chloride with a noble gas configuration. This behaviour is illustrated in

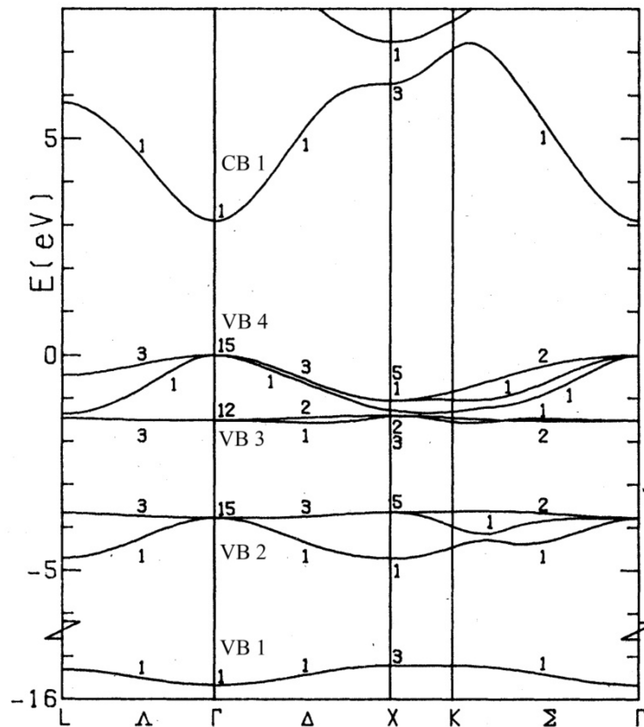

***Figure 1.3** The energy band diagram of CuCl [22]*

figure 1.3, where the degeneracies of each band are shown also. There are nine occupied valence bands (due to the Cl s & p levels and the Cu d levels, grouped as VB 1, VB 2, VB 3 and VB 4) occupied by 18 electrons. Each of these bands are characterised by the different spin orbitals attributed to each. The lowest band, VB 1, almost entirely originates from the 3s Cl orbital, VB 2 is largely derived from the 3p Cl orbitals with the highest bands VB 3 and VB 4 both characterised by the 3d electrons of Cu [58]. The conduction band CB 1 is defined by the 4s Cu orbital.

This process is illustrated in figure 1.4. Column (a) shows the relevant atomic states of copper and chlorine prior to incorporation in the compound. Once the crystal field of tetrahedral rotational symmetry is applied, the Cu d orbital levels and Cl p orbital levels hybridise and split into two Γ_5 levels and one twofold degenerate Γ_3 level as shown in column (b). This hybridization of the d and p orbital levels increases the

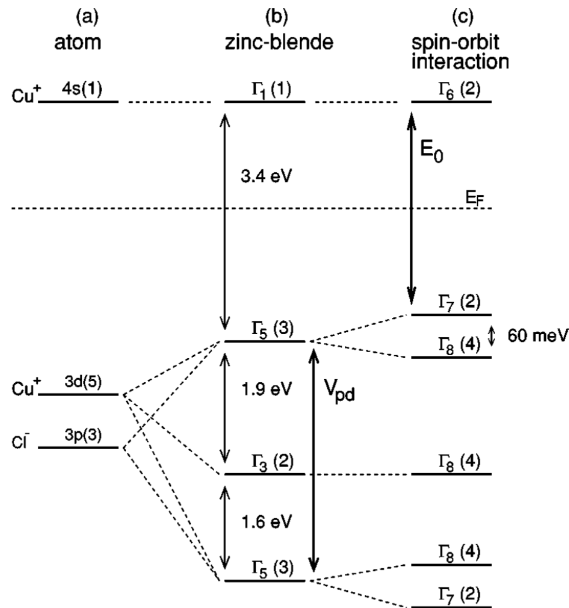

Figure 1.4 *Schematic derivation of the conduction and valence bands at the Brillouin Zone Centre Γ in CuCl. Energies given are the derivated values. The numbers in brackets indicate the level of degeneracy of the corresponding state. [59]*

top of the valence band relative to the Cl p-level which in the absence of the Cu d-orbital would determine the valence band maximum [59]. This effect is the same for all copper halides and causes the band gap to be much smaller than expected if the sequence of group IV (Ge 0.67eV), III-V (GaAs 1.43eV) and II-VI (ZnSe 2.7eV) semiconductor materials is extrapolated for I-VII materials (CuCl 3.399eV) [15]. Another sign of the importance of the Cu d-levels is that the p-levels of the halides Cl, Br, and I differ by about 2 eV but the band gaps of CuCl, CuBr and CuI differ by less than 0.3 eV. This shows that the anions have only a small influence on the band gap [60].

When the spin-orbit interactions are taken into account as shown in column (c), the p and d orbital mixed Γ_5 states split into levels of Γ_7 and Γ_8 symmetry. The d-states contribution to the spin-orbit splitting is of opposite sign to the p-orbitals which causes the Γ_7 states to be higher in energy than the Γ_8 states which results in a reversal of the order of uppermost valence states in CuCl [60-62]. This effect does not occur for CuBr and CuI as the increase in atomic weight causes an increase in the splitting of the atomic p orbitals which leads to the regular zinc-blende splitting scheme to be observed.

The coupling of the lowest conduction band state Γ_6 to both the holes in the uppermost levels Γ_7 and Γ_8 gives rise to the Z_3 and $Z_{1,2}$ edge excitons respectively. Due to the reversal of the order of the valence states Γ_7 and Γ_8 the Z_3 exciton appears at a lower energy than the $Z_{1,2}$ exciton. This was shown by an examination of the energy of the exciton peaks as a function of concentration in the CuBr-CuCl system [61]. The energy values and temperature dependencies of these peaks will be studied throughout this thesis.

1.6 Structure of Thesis

This thesis describes experimental and modelling work on the characterization of CuCl and related thin films for possible optoelectronic applications. The methods of characterization used previously in our laboratory for ZnO thin film characterization were applied to analyse the behaviour of CuCl thin films on Si. Due to the low level of previous interest in the development of CuCl thin films the characterization of this material using updated equipment and methods should provide a wealth of previously undocumented information about their properties and prospective uses. The other sections in this thesis begin with a section for a theory and literature review of each of the methods of characterization with further chapters divided by the method of analysis in question so that the results obtained from each method can be focussed upon. Each of these chapters begins with a brief introduction and concludes with a summary of the key points discussed.

Chapter 2 provides a comprehensive detailing of the theory behind each of the experimental methods used throughout our research and a summary of the previous papers published relating to CuCl in each field. This literature overview is intended to provide a reference point for knowledge in each of the methods used leaving later chapters free to focus on the results obtained and how they have contributed to and extended the existing research in each field. This chapter also contains a thorough description of each of the system parameters of the actual experimental systems used to characterize the CuCl samples; reflectance, cathodoluminescence (CL), x-ray diffraction (XRD), scanning electron microscopy (SEM) imaging, energy dispersive x-ray spectroscopy (EDX) and photoluminescence (PL). The equipment used and the

procedure of analysis for each will be discussed. The cleaning procedure and method of preparation of the samples are also detailed in this chapter.

Chapter 3 contains detailed results from our XRD analysis of the structural properties of our nominally undoped CuCl on Si thin films samples, our doped CuCl samples which were doped with both oxygen and potassium, and CuCl samples surface coated to protect them from degradation in air. The information this supplies us about the crystallinity and preferred orientation of the growth of the samples is then discussed.

Chapter 4 contains the results obtained by SEM imaging, energy-dispersive X-ray spectroscopy (SEM-EDX) and cathodoluminescence (CL-SEM), focusing on the electrical properties of the material and the information the excitonic spectra provide about the thin films. This is accompanied by data and analysis of doped CuCl samples and a comparison of how the doping affected the electrical properties and atomic structure of the samples.

Chapter 5 begins with the results of our reflectance and photoluminescence (PL) experiments which provide a more detailed analysis of the exciton-polariton behaviour within CuCl and the optical properties of the material. To aid the analysis of our reflectance data, a MATLAB simulation using Maxwell's equations, with suitable electromagnetic and additional required boundary conditions (ABCs, specifically the Pekar ABC's including dead layers) was developed. This allows us to obtain further information about the thin films by matching the shape of the simulated plot with our experimentally obtained data. Each of our CuCl/Si thin film samples was analysed

using this method with a focus on the influence of altering fit parameters on our sample optical properties.

Chapter 6 is the final chapter and contains the conclusions that can be drawn from our work as well as outlining further avenues for future research on this subject.

Chapter 2

Methods of Characterisation

2.1 Introduction

During our research many different experimental techniques were utilized to characterize the CuCl samples which were grown. This chapter contains the details of the sample preparation, a summary of each of the types of characterization, the theory behind them and the information about the CuCl substrates that each of these methods provide. We begin with the sample preparation, then the structural analysis provided by x-ray diffraction, followed by the microscopic and other aspects of analysis using the SEM with various attachments and finally the optical properties of the material obtained by reflectance and photoluminescence. This will provide an understanding of the core principles in each of these areas and specifically their use in relation to CuCl.

2.2 Sample Preparation

The CuCl and related thin films studied in this thesis are grown on Si substrates with (100) surface orientation approximately 2 cm by 1.5 cm in size cut from a 4 inch silicon wafer. These wafers are single-sided, polished, p-type boron-doped (100) silicon with a resistivity in the range of 0 – 20 Ω cm. Prior to deposition the substrates are degreased using Decon neutral (Decon Laboratory Ltd.) solution and

organic solvents. This involves placing the substrates in the Decon solution inside an ultrasonic bath for 7 minutes. Upon completion the substrates are rinsed with deionised water and then Decon directly applied using cotton buds. This is rinsed once more using deionised water and the substrates are then placed into an ultrasonic bath with deionised water for a period of 20 minutes. Finally they are removed from the water and dried using a hairdryer.

The native silicon oxide is then removed using a diluted hydrofluoric acid solution which it is immersed in for a period of 1 minute. This procedure passivates the surface with H and creates a long-term stable oxide-free Si surface [63]. In time an alternative etch, called a dash etch, was used as this generated smoother, cleaner samples to the extent that the difference is visible to the naked eye. The substrates are dipped in an acidic solution comprised of 50 ml nitric acid, 30 ml hydrofluoric acid and 30 ml acetic acid for 30 seconds. Following this the substrate is immersed in 2 beakers of deionised water sequentially, one containing acetone and one with isopropyl, each for 30 seconds. Finally the substrates were stored in methanol for up to 10 minutes whilst the remaining samples in the batch completed the dash etch process.

2.2.1 Thermal Evaporation Deposition

Once the sample cleaning and etch processes are completed, the substrates are dried off and placed inside the vacuum chamber of an Auto 306 Edwards evaporation system. This is an automated thermal resistance evaporation system which is a form of physical vapour deposition. The system has a base pressure of 1×10^{-6} mbar and an evaporation pressure of $\sim 3.0 \times 10^{-6}$ mbar. An FTM6 thickness monitor works in tandem with a water-cooled crystal holder to output the nominal thin film thickness as the evaporation is performed. CuCl powder with 99.999% purity (Alfa Aesar) is placed

inside a quartz crucible. Throughout the course of this work these were in powder and beaded form arriving in both sealed ampoules and sealed glass jars. No significant difference was recorded between these configurations and once this was established glass jars were used from that point on as a means of convenience. This is evaporated by resistive heating of the crucible and results in CuCl deposition onto the substrate. The substrate is positioned approximately 10 cm above, held firmly in place by metal clasps coated with aluminium foil. To ensure an even deposition the substrate remains covered (but not in-contact) with a layer of metal coated in aluminium foil which masks the substrate until the rate of evaporation stabilizes. The schematic of this is shown in figure 2.1.

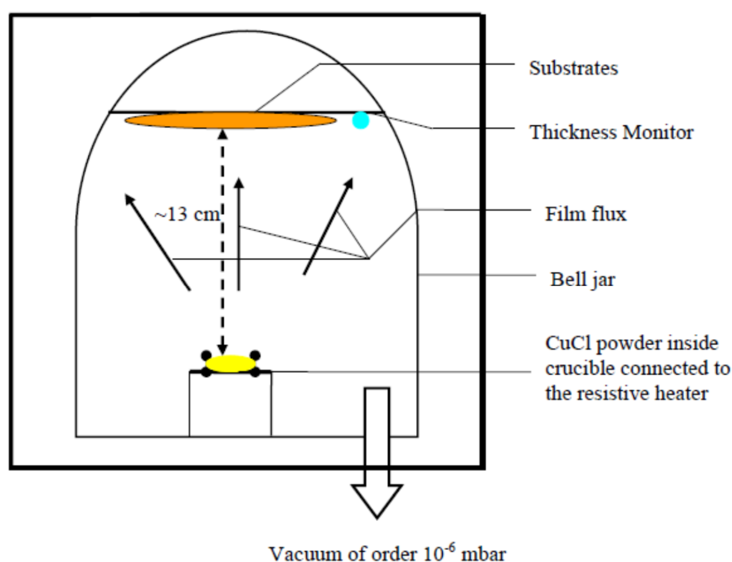

***Figure 2.1** Schematic diagram showing the growth of CuCl thin films using the vacuum evaporation technique [64]*

The thickness of the deposited CuCl is calculated using the measured crystal resonant frequency, the deposition material density and tooling factors as follows:

$$T_c = \frac{FD_qN_q(P_q - P_6)}{D_e}$$

Eqn. 2.1

where T_c is the calculated thickness, F is the tooling factor, D_q is the density of quartz, N_q is the frequency constant of quartz, P_q is the period of a loaded crystal, D_e is the density of the deposition material and P_6 is the period of a 6 MHz crystal used in the thickness monitor. The density of the film material is calculated from:

$$D_e = D_a \frac{T_i}{T_m}$$

Eqn. 2.2

where D_a is the accepted value of the density of the deposition material (which for CuCl is 4.136 g cm^{-3} [15]), T_i is the thickness measured by the thickness monitor and T_m is the average actual thickness. T_m is determined by depositing several different samples and determining their thickness through experimentation. The tooling factor F is calculated by dividing the average actual thickness by the thickness measured by the thickness monitor,

$$F = \frac{T_m}{T_i}$$

Eqn. 2.3

This is used to compensate for the difference in the distance of the substrate from the source compared to the distance of the crystal from the source. A tooling factor of 3.13 was previously calculated for the CuCl samples [65] indicating that the substrate receives a larger deposit than the crystal, which is to be expected due to its placement directly above the evaporation source.

The CuCl was evaporated from within the crucible at a rate ~0.5 nm s^{-1} via a current of ~2.5 A passing through the resistively heated part of the crucible containing

the powder. This rate was chosen as previous work in our group has shown 0.5 nm s^{-1} to be optimum for sample quality and reproducibility with faster rates causing particulates on the surface of the film and slower rates resulting in a non-uniform deposition and providing no justification for the increase in time required [65].

Typically layers of ~500 nm of CuCl were deposited with some small variance due to the nature of the equipment as it was observed that the CuCl film is not uniform in its distribution across the surface of the substrate. Directly above the crucible shows the thickest CuCl deposition with a decrease in thickness as the distance from this centre point is increased. The thicknesses quoted in the thesis thus are in all cases an average or "nominal" deposit thickness. This can be observed visually by the different colours present on the substrate and interior of the evaporation chamber illustrated by the picture in figure 2.2 of the CuCl thin film surface.

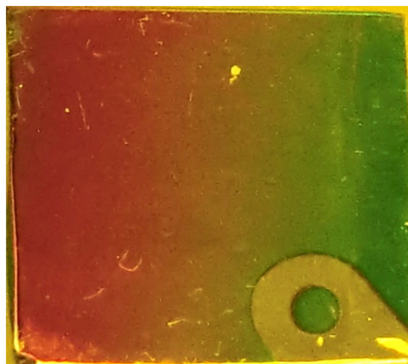

Figure 2.2 *Digital CCD image of the surface of a freshly deposited 500 nm thin film sample showing the variation in the colour across the surface of the sample. The region in the bottom right is due to clamps holding the sample in place during deposition*

Due to the hygroscopic nature of CuCl commented upon earlier, upon removal from the deposition vacuum system it is essential that some form of capping

layer is applied if the samples are not to degrade very quickly (without such a layer the samples decay noticeably in 1-2 days as detailed in later chapters). For samples to be tested via X-ray diffraction, a protection layer of long-lasting nail varnish is applied to prevent the decay of the samples [66]. The nail varnish is an amorphous coating and so has no effect on the x-ray diffraction measurements and to show this a comparative study is detailed in the results section for reference (see chapter 3). This brand was the only one tested as there was no need to change this once a working solution was found.

However, for samples where optical measurements such as PL, CL and reflectance are intended, the capping layer caused some problems. Exposure to low temperatures as part of PL or reflectance measurements at cryogenic temperatures, caused the entire thin film (including the CuCl deposit) to delaminate from the substrate. Since this didn't happen with uncapped samples it is clear that it was caused by the varnish, probably associated with differential thermal expansions giving rise to a bimetallic strip type of effect. In addition, the results of some room temperature PL measurements showed that the capping layer significantly lowered the intensity of the UV bandedge emission signal. Since the wavelength of the CL emission is essentially identical to that of the PL emission (around 385 nm at room temperature) this would affect these measurements as well. Samples were thus left uncapped for the reflectance, PL and CL measurements as these take place in a helium filled chamber (reflectance and PL) and a vacuum chamber (CL), which ensures that the samples do not decay as in all cases there is no significant water vapour present.

2.2.2 Oxygen Doping of CuCl thin films

To improve the electronic conductivity of some of the samples of CuCl, oxygen was introduced as a p-type dopant once the samples had been grown by

evaporation. This doping was carried out by plasma treatment in an Oxford Instruments Plasma Lab Plus 80 Reactive Ion Etcher (RIE). Oxygen and argon were pumped in via dedicated channels with flowmeters at flow rates of 80 sccm and 20 sccm; the RF power was 300 W, while the chamber pressure was held at 50 mTorr. The argon was present to aid the penetration of the oxygen into the samples. Different durations of treatment were performed for different samples, with times of exposure ranging from 30 seconds to 4 minutes to compare the effects of the treatment. Upon completion of this treatment the samples were handled in the same manner as the undoped samples, i.e. they were taken for immediate characterization, sealed with varnish or placed within a sealed vacuum chamber for storage until use.

2.2.3 Liquid Phase Epitaxy

DCU has recently completed the construction of a liquid phase epitaxy (LPE) growth system [49]. LPE can be used to grow a single crystal semiconductor layer on a substrate. In this technique, CuCl powder and a solvent are heated until melted and a eutectic solution of semiconductor material is formed. The silicon substrate is also heated but to a slightly lower temperature and then brought into contact with the semiconductor material. The solution and the substrate are then cooled below the eutectic temperature to deposit a layer of the semiconductor material onto the silicon. After a predetermined interval, the silicon and the solution are separated from each other and allowed to settle.

CuCl undergoes a transition from zincblende to wurtzite structure when the temperature is increased above 408 ℃ [67] and prior to the melting point at 422 ℃. As temperature is increased there is also an exothermic CuCl-Si reaction which occurs once the temperature is increased above 250 ℃ [42]. To avoid the influence of these

factors on the deposited samples the addition of a salt to the melt must be used to reduce the mixture eutectic. There are several candidates for this, such as potassium chloride (KCl), strontium chloride ($SrCl_2$) and barium chloride ($BaCl_2$) [65]. Of these candidates KCl seemed the best because it possesses the lowest eutectic temperature [68]. While my work was not centred on single crystal LPE growth, I was involved in growing samples of KCl/CuCl alloy thin films on CuCl films using thermal evaporation to study the properties of such alloys which are likely to form in the LPE system and thus support the LPE growth efforts.

Firstly, a 450 nm layer of CuCl was deposited as previously described, after which a 50nm layer of KCl-CuCl alloy (with a molar ratio of KCl to CuCl of 20:80) was deposited. The KCl-CuCl powder mixture used in the crucible of the thermal evaporator is measured with an electronic mass balance to ensure the ratio is accurate and the powders mixed and ground with a mortar and pestle until a suitable consistency is achieved. The ratio was chosen to encourage formation of the random

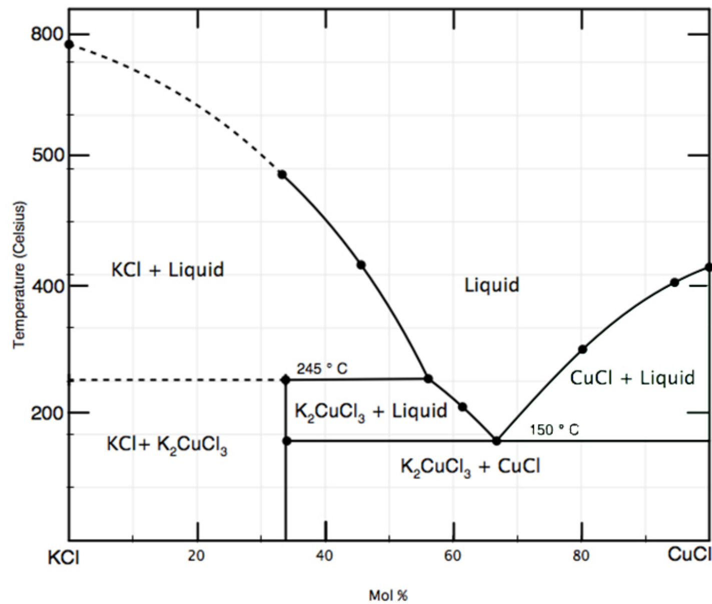

Figure 2.3 *Phase diagram for KCl – CuCl [69]*

alloy mixture K_2CuCl_3 which, as shown in figure 2.3, forms below 245ºC when the ratio is 20:80 with CuCl [69]. The evaporation temperature of the K_2CuCl_3 was not considered an issue due to the similarity of KCl and CuCl's individual evaporation temperatures (1420 ˚C and 1490 ˚C) i.e. the temperature of the system will be sufficient to evaporate KCl, CuCl and the K_2CuCl_3 compound if formed inside the quartz crucible used in the deposition process. The results of the characterization of this material are shown in Chapter 3. In later experiments a complete 500 nm layer of CuCl mixed with KCl in the 20:80 ratio was used instead and will be discussed as such in future chapters. The preparation method was similar to that described above.

2.3 Structural Analysis – X-ray Diffraction

Because of the similarity of the wavelength of x-rays (~0.1 nm) to interatomic spacings in most crystals (~0.5 nm), it was realised rather early on in the development of x-ray science and technology that x-ray diffraction might enable scientists to map the atomic structure of a molecule or crystal. This was discovered as early as 1912 by Max von Laue [70]. In the same year W. H. Bragg and his son W.L Bragg analysed von Laue's experiment and were able to express the necessary conditions for diffraction in a considerably simpler form than that used by von Laue. The following year they used these conditions to solve the structures of NaCl, KCl, KBr and KI, all hexagonal in nature, which were the first complete crystal-structure determinations ever made [71]. It will be noticed that these crystals are all I-VII compounds similar to CuCl and KCl, and this makes a nice historical link to the present research work.

A Bruker Advanced X-Ray Solutions D8 X-Ray Thin Film Texture Diffractometer was used for our studies of the crystal structure of our samples, which is available in the National Centre for Plasma Science and Technology (NCPST) laboratories in DCU. All x-ray generation tubes work on a similar principle, i.e. using a source of electrons accelerated through a high voltage incident on a metal target to generate characteristic x-rays of the target material [72]. The metal target in the D8 Diffractometer is a Cu target which acts as the anode and the filament source of the electrons as the cathode. The anode is held at a 40 keV potential difference to the cathode and a current of 40 mA is passed through the filament which heats the filament and releases electrons by thermionic emission, and these electrons are then accelerated towards the target leading to the emission of characteristic x-rays of wavelength 0.15406 nm and 0.15444 nm, i.e. the Cu $K_{\alpha1}$ and Cu $K_{\alpha2}$ respectively. The source has some filtering using e.g. Ni films to remove other characteristic x-ray lines (Cu K_{β}) and the underlying bremsstrahlung continuum emission.

When the x-rays are incident on the atoms in the sample they are scattered in all directions. In some of these directions the scattered beams are completely in phase and reinforce each other to form diffracted beams. Figure 2.4 demonstrates this technique. If we examine the rays 1 and 1a it is clear that they strike the atoms K and P in the first plane. In the directions 1' and 1a' the beams scattered from the plane are completely in phase. This is because the difference in the length of path between the two wavefronts is equal to:

$$QK - PR = PK\cos\theta - PK\cos\theta = 0 \qquad \textit{Eqn. 2.4}$$

due to the symmetrical nature of the scattering (equal incidence and reflection angles).

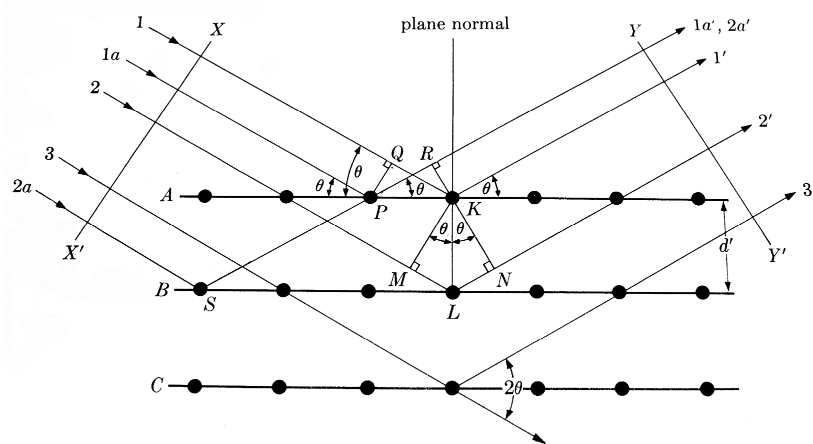

Figure 2.4 *Diffraction of x-rays by a crystal [73]*

This is true for rays scattered from all atoms along the first plane, they emerge in phase and add their contribution to 1'. From the second layer of atoms the path difference for rays 1 and 2 which are scattered from K and L is given by:

$$ML + LN = d'\sin\theta + d'\sin\theta \qquad \textit{Eqn. 2.5}$$

The scattered rays will be in phase if the path difference is equal to a whole number of wavelengths. This relation was first formulated by W.L. Bragg in 1913 and is known as Bragg's Law [74]. It is the requirement which must be met if diffraction is to occur and is:

$$n\lambda = 2d'\sin\theta \qquad \textit{Eqn. 2.6}$$

where d' is the distance between the planes, n the order of diffraction and θ the angle of incidence of the x-ray beam.

The basic setup of the diffractometer is the parallel beam geometry mode (also referred to as the θ/2θ scan mode) shown in figure 2.5. The sample is rotated at a set angular velocity representing θ with the detector rotating at twice the velocity thus maintaining 2θ. The x-ray beam strikes the sample and each time the Bragg condition is met the x-rays are diffracted onto the detector. The electronics inside the detector

measure the intensity of the diffracted beams and uploads the data to an attached computer so that the diffraction patterns can be digitally recorded.

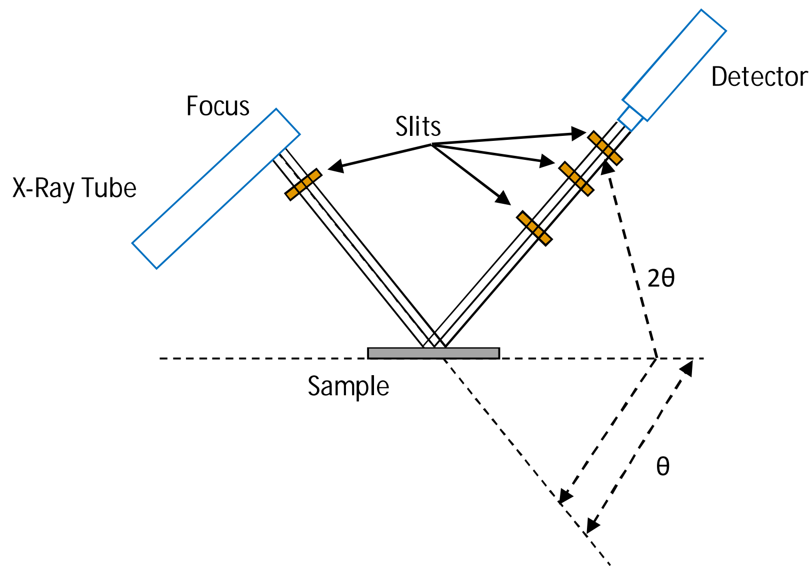

Figure 2.5 *Parallel beam geometry setup for the Bruker D8 Advance Diffractometer*

To control the quality of the results a series of slits along the x-ray beam's path can be altered with different slides provided by the manufacturer. An aperture slide is placed in front of the beam to control the area of the sample exposed to the x-rays. Starting from the sample, there are 3 slits; the first to block any undesired scattered radiation, the second to reduce the intensity of any Cu K_β rays reflected by the sample and the third to align the x-rays with the detector. The thickness of the slide blocking the Cu K_β rays can be adjusted depending on the results of the scans. Typically it is removed completely once the θ/2θ scans are started but it is useful in aligning the beam with the detector upon initial setup.

For a sample of normal incidence, as is the case in the θ/2θ scans, the penetration depth of the x-rays is defined by $1/\mu$, where μ is the attenuation coefficient. These are typically in the range of 10^4 – 10^5 m^{-1} with the corresponding $1/\mu$, values in the 10 – 100 μm range. Since our samples are

considerably thinner than this, in order to eliminate interference from the CuCl/Si boundary and Si substrates and obtain information from purely the upper layer of the thin films, glancing angle x-ray diffraction is occasionally used (GAXRD).

To perform this, the angle of the incident x-ray beam is set to a very shallow angle. With the angle of the beam held at this fixed glancing angle, the diffraction profile is recorded using a detector-only scan. The resulting diffracted and scattered signals arise mainly from a limited depth beneath the surface of the material and arise from misoriented crystallites at the film surface. The setup for GAXRD is shown in figure 2.6.

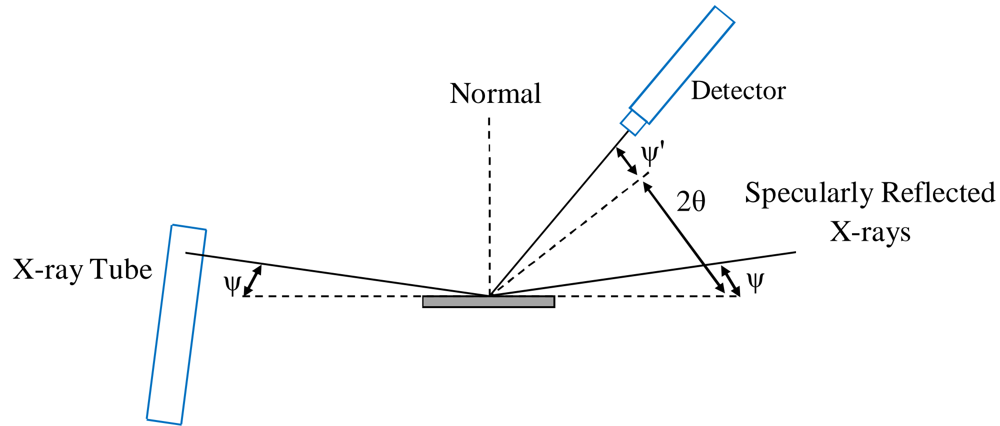

Figure 2.6 *Glancing Angle X-ray Diffraction schematic*

Using glancing angles, refraction at the surface of the sample can be described by $\cos\psi = n\cos\psi_1$ where ψ_1 is the glancing angle inside the material. When the angle of incidence (ψ) of the x-ray beam decreases, so that the refractive index is less than unity, total external reflectance of the x-rays occur below the critical angle of incidence (ψ_c) [75]. The critical angle required for total external reflection is defined by $\cos\psi_c = n$, where n is the refractive index. According to James [76], the refractive index can be determined from:

$$n = 1 - \frac{r_{el}\lambda^2}{2\pi}\sum_i (Z_i + \Delta f_i)\, N_i = 1 - \delta - i\beta$$

Eqn 2.7

where r_{el} = 2.818 x 10^{-13} cm is the classical electron radius, λ is the x-ray wavelength, Z_i the atomic number of the atom i, N_i the number of atoms i per unit volume, δ and β represent the real and imaginary parts of the complex quantity $(1 - n)$ and $\Delta f_i = \Delta f_i' + i\Delta f_i''$ which is the dispersion correction of the atomic scattering factor for zero scattering angle. Values for the dispersion correction can be found in the International Tables for X-Ray Crystallography [77]. However if we approximate the equation by neglecting the dispersion, the real part of the refractive index can be expressed as:

$$\delta = \frac{r_{el}\lambda^2}{2\pi} N\rho \frac{\sum Z_i}{\sum A_i} = 2.70 \times 10^{10}\lambda^2\rho\frac{\sum Z_i}{\sum A_i}$$

Eqn. 2.8

with N representing Avogadro's number, ρ the density, and A_i the atomic weight of the atom i. This can be solved for CuCl using the known values for each of the quantities, ρ_{CuCl} = 4.136 g cm^{-3}, A_{CuCl} = 98.999 g/mol, giving a value of δ = 12.32 x 10^{-6}. Since ψ, $\delta \ll 1$ the relation between them can be written as $\psi_c = \sqrt{2\delta}$. This allows us to calculate the value of ψ_c which comes to 0.28° for CuCl. This is the point of total external reflection within CuCl, ideal for GAXRD. However, the x-ray beam divergence angle of the equipment in DCU is too broad to set an angle this shallow. The penetration depth for an incidence above the critical angle can be determined from the absorption coefficient, μ, in the following manner:

$$t_p = \frac{\sqrt{\psi^2 - \psi_c^2}}{2\mu}$$

Eqn. 2.9

where t_p is the penetration depth. μ for CuCl can be calculated from the x-ray diffraction beam intensity.

The particle size of the crystallites measured by x-ray diffraction can be determined from the θ/2θ scans and the GAXRD scans by examining the width of each of the diffraction curve peaks. These widths increase as the crystallite size of the deposit decreases because the angular range increases as the order of diffraction decreases [73]. The width is usually measured in radians at an intensity equal to half of the maximum peak intensity, referred to as the full width at half maximum (FWHM). If we approximate the shape of the diffraction peaks to be triangular we can take half the distance between the two angles for which the intensity is zero to be the FWHM. The relation between crystallite size and the experimentally measurable values known as the Scherrer formula is given by:

$$t = \frac{0.9\lambda}{B\cos\theta_B}$$

Eqn 2.10

where we let B represent the FWHM and θ_B the Bragg angle. In deriving this relationship we let θ_1 and θ_2 be the angles of zero intensity. Expressing the FWHM in terms of the zero intensity angles gives us:

$$B = \frac{1}{2}(2\theta_1 - 2\theta_2) = \theta_1 - \theta_2$$ *Eqn 2.11*

If we write the path-length difference for these angles, similar to the Bragg Law equation already shown in equation 2.6, but relating it to the entire thickness of the crystal we get:

$$2t\sin\theta_1 = (m + 1)\lambda$$ *Eqn 2.12*

and

$$2t\sin\theta_2 = (m - 1)\lambda$$ *Eqn 2.13*

By subtracting each of these we get

$$t(\sin\theta_1 - \sin\theta_2) = \lambda \qquad \textit{Eqn 2.14}$$

$$2t\cos\left(\frac{\theta_1 + \theta_2}{2}\right)\sin\left(\frac{\theta_1 - \theta_2}{2}\right) = \lambda$$

Eqn 2.15

Since θ_1 and θ_2 are almost equal to θ_B we can approximate:

$$\theta_1 + \theta_2 = 2\theta_B \qquad \textit{Eqn 2.16}$$

and similarly

$$\sin\left(\frac{\theta_1 - \theta_2}{2}\right) = \left(\frac{\theta_1 - \theta_2}{2}\right)$$

Eqn 2.17

So substituting these into the previous equation gives us:

$$2t\left(\frac{\theta_1 - \theta_2}{2}\right)\cos\theta_B$$

Eqn 2.18

$$t = \frac{\lambda}{B\cos\theta_B}$$

Eqn 2.19

A more exact treatment of this problem gives us the aforementioned Scherrer formula:

$$t = \frac{0.9\lambda}{B\cos\theta_B}$$

Eqn 2.10

The 0.9 factor is based on refined assumptions made for the shape of the crystals and of the diffraction peaks themselves [78]. The Scherrer formula was used to estimate the crystal size of the CuCl samples measured by both GAXRD and θ/2θ XRD. To confirm epitaxial growth of the samples a φ scan is used by setting the sample to a fixed Bragg angle and to a fixed χ angle to bring one of the equivalent

(0,1,2) planes into the path of incidence of the x-rays. This is shown in figure 2.7 with the sample position represented by the imposed square section.

The sample is then rotated about its φ axis and the diffraction peaks will be detected at fixed intervals if the crystal is symmetrical or just a uniform signal if there is no plane order at all. For example if the structure exhibits four-fold symmetry then the signal should occur every 90º, if it exhibits hexagonal symmetry every 60º etc. In the case of the CuCl thin films, both CuCl and Si exhibit four-fold symmetry so two signals from each of the layers separated by 90º are expected. The overlap between the two layers will be investigated in Chapter 3.

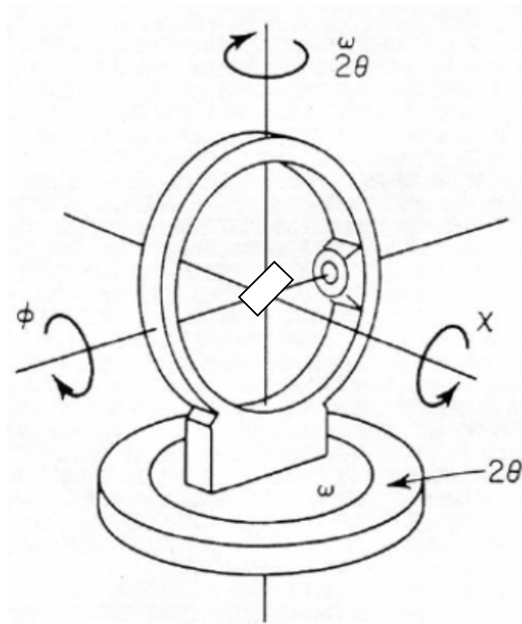

Figure 2.7 *X-ray diffractometer display showing the motion and orientations of the ω, φ and χ angle x-ray diffraction scans [79]. Square in the centre represents the sample position. The sample should be considered to be facing the ϕ direction in this graph*

2.4 Optical Properties

2.4.1 Photoluminescence

Photoluminescence (PL) can be defined as the emission of light from a material illuminated by photons. Luminescence emission involves radiative transitions between electronic energy levels in an excited material with the resulting photonic emission characteristic of that material.

The transition originates in an excited electronic level within the material and after the emission of a photon a lower electronic level is occupied. This process is non-contact and generally non-destructive and therefore extremely useful in semiconductor characterisation. The cause of the initial excitation determines the term given to the luminescence. Luminescence excited by a bombardment of electrons is termed cathodoluminescence and luminescence excited by electromagnetic radiation is termed photoluminescence. These are the two types of luminescence used to analyse CuCl throughout the course of this work.

The three key processes involved in luminescence are:

- Excitation
- Energy transfer and thermalisation
- Radiative transition of the carriers

The incident photons will normally be of a higher energy than the band gap as this will result in a large number of free electron-hole pairs being generated. In semiconductor materials the absorption of photons of higher energy than the bandgap results in the creation of free electrons and holes, a non-equilibrium distribution of the

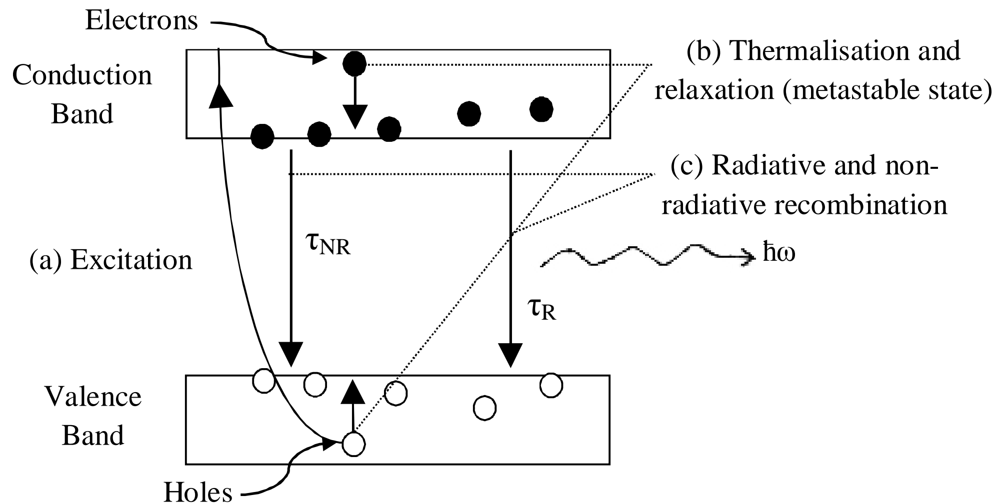

Figure 2.8 *Schematic diagram of the general process of luminescence. (a) Excitation by external source (b) thermalisation and relaxation to create metastable e-h pairs denoted as excitons (c) recombination which can be of two types; radiative (τ_R) and non-radiative (τ_{NR}). The emission of a photon due to radiative recombination is known as luminescence*

electron-hole (e-h) pairs. These will quickly thermalise (~5 ps) to reach thermal equilibrium amongst themselves, thus reaching the quasi-thermal equilibrium described by quasi-Fermi levels in a short time compared to that taken for e-h recombination (typically > 200 ps). This thermalisation creates a population of electrons and holes close to the conduction and valence band edges, respectively. At low temperatures in relatively pure materials, where the effect of the stray electric field effects is minimal, the Coulomb attraction between the electron and hole causes their motion to be correlated. The resultant Coulombically bound e-h pair is known as an exciton.

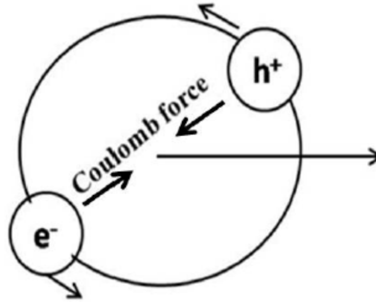

Figure 2.9 *Exciton showing the electron and hole Coulombic attraction. The centre-of-mass motion of the exciton is indicated by the arrow pointing to the right [80]*

Due to the exciton being a bound electron and hole pair, the formation energy is slightly less than that for an unbound electron and hole pair. This excitonic particle can be considered as an electron and hole pair orbiting around a common centre-of-mass and bound together in a Bohr atom-like fashion as shown in figure 2.9. This means the binding energy, Bohr radius and other factors of the exciton can be calculated using the Bohr model equations, taking into account the effective masses of the particles and the dielectric constant of the semiconductor.

There are two main types of exciton, the Frenkel exciton and the Mott-Wannier exciton. Frenkel began the study of these excitations in 1931 when he proposed the model of this quantum of excitation propagation in insulating crystals [81]. His type of excitons is tightly bound with a small radius. When the dielectric constant is very small in a material, the Coulomb interaction between electron and hole becomes very strong. This causes the exciton radius to be quite small, of the same order as a unit cell. As a result of this the electron and hole can be viewed as occupying the same cell, allowing the exciton to hop from cell to cell. The typical binding energy of this Frenkel exciton is of the order 1.0 eV. These excitons are typically realized in alkaline halide crystals and in many crystals of aromatic organic

molecules. So for the Frenkel exciton in an alkaline halide or strongly ionic insulators, the excitation dimension is limited to a single atom or molecule.

The Mott-Wannier exciton model deals with insulators and semiconductors possessing larger dielectric constants. This means the exciton radius is much larger than in the Frenkel model and the electron can be considered to orbit many unit cell distances from the hole. These excitons have a much larger radius than the lattice spacing meaning the electron and hole are separated by a large degree of interatomic spacing. The larger dielectric constant in these materials reduces the Coulomb interaction between the electrons and holes. This means the effect of the lattice potential can be incorporated into the effective masses of the electron and hole. Because of the lower masses and the screening of the Coulomb interaction the binding energy is much less than the Frenkel exciton, being typically of the order 0.1 eV or below. There also exists a charge-transfer exciton, being the intermediate form between the Frenkel and Mott-Wannier exciton models.

For CuCl the exciton binding energy is 190 meV and the Bohr radius is 0.7 nm. These factors mean it can be considered a Mott-Wannier exciton. In a pure material at sufficiently low temperatures (where $kT <$ exciton binding energy), the exciton is a stable particle and will not become thermally disassociated.

In an intrinsic semiconductor free of any defects or impurities, the exciton centre-of-mass is free to move within the material and is known as a **free exciton** (FE) [82]. Most materials contain finite quantities of defects and impurities. Disruption of the periodicity of the lattice may either destroy the exciton or localize it. This can be caused by a number of factors including: impurities, vacancies, dislocations and even large scale defects such as the surface of the material. The localization of Mott-

Wannier excitons on impurities was predicted by Lambert in 1958 and observed by Haynes in 1960 in the form of narrow peaks below the free exciton level in Si [83].

The impurities can trap the FE, binding the exciton to the defect location with a certain and impurity specific localization energy. These trapped excitons are known as **bound excitons** (BE). The localization energy is dependent on the nature of this defect; factors such as the chemical identity, symmetry, defect charge state, etc. can affect it. The localization energy of the exciton on an impurity, measured from the FE line, is usually a fraction of the ionization energy of the impurity which localizes the exciton. At low temperatures most of the FEs in real materials are trapped and bound at defects due to the thermalisation effects. As the temperature is increased these are gradually released to form FEs once more.

The quantum mechanical states between which the main transitions studied in this thesis occur are the conduction and valence bands. In the first instance we will consider the case of a pure crystal with no impurities and with no electron-hole interaction.

The transition process is generally described by showing the valence and conduction bands on an E-K diagram. When the valence band maximum and the conduction band minimum in a material are at the same value of the wave vector k such materials are referred to as direct gap semiconductors (symmetry considerations often constrain the value of k at which this occurs to be at the centre of the Brillouin zone, $k = 0$, and we assume this in further discussions). When the valence band maximum and the conduction band minimum are at different values of k, the material is an indirect gap semiconductor. CuCl is a direct gap semiconductor, so the illustration in figure 2.10 (a) will apply.

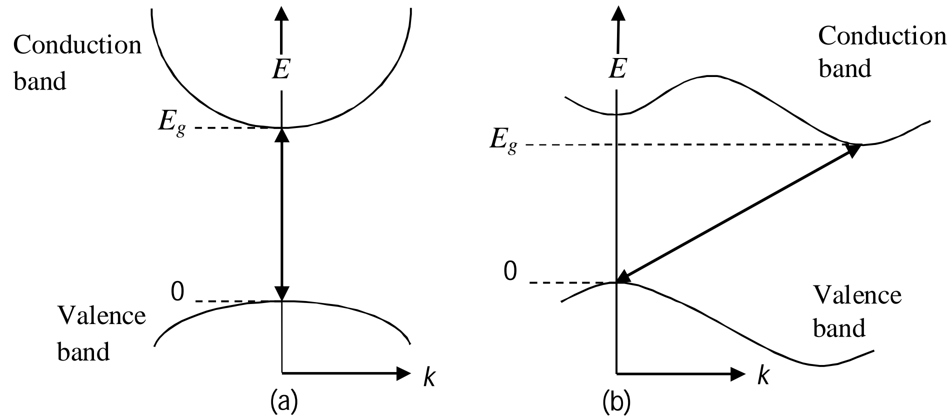

***Figure 2.10** Part of the E versus k curves for (a) direct semiconductors and (b) indirect semiconductors. The band gap transitions are indicated by the arrows.*

Because the *k*-vector of the photon ($2\pi/\lambda$ with $\lambda \sim 350$ nm, yielding a value of approximately 2×10^7 m^{-1}) is so much smaller than the dimensions of the Brillouin zone (π/a, with $a \sim 0.5$ nm, yielding a value of approximately 6×10^9 m^{-1}) the conservation of *k*-vector required in the matrix element for the conduction band to valence band transitions means that (when viewed on the scale of the Brillouin zone) that transitions involving photons only correspond to vertical "jumps" on an *E*-*k* diagram, as shown in figure 2.10 (a). Thus transitions from the valence band maximum to the conduction band minimum can occur involving only a photon of appropriate energy and thus are strongly allowed. Direct bandgap materials such as GaAs, GaN, ZnO and CuCl tend to be strong optical absorbers and emitters close to the bandgap energy and are thus useful for device applications.

By contrast, in an indirect gap material such as Si the transition between the valence band maximum and the conduction band minimum requires another particle to conserve *k*-vector and thus is less strongly allowed due to the three-body nature of the process (electron, photon and phonon). Hence the quantum mechanical matrix element

for transitions in indirect gap materials is reduced compared to direct gap materials and becomes dependent on the phonon population. The radiative transition probability for indirect gap materials is far less than direct gap materials and competing non-radiative transitions are much more prominent. This means indirect bandgap materials are less efficient optical emitters and absorbers and a poor choice for device applications.

The discussed *k*-vector conservation applies to free electron, free hole and FE transitions and also to transitions of loosely BE or carriers, possessing wavefunctions similar to FE or free carriers. Tightly bound species result in a relaxation of the k-vector conservation rules, but these transitions are not the focus of this thesis.

Indirect band gap semiconductors are typically used as the material substrate onto which direct band gap semiconductors are deposited by various methods. Si and Ge are good examples of this, with CuCl and ZnO being good examples of direct bandgap semiconductors. The strong exciton binding energy of CuCl combined with a direct bandgap means it is a very efficient optical emitter and absorber as these factors create a strong e-h wavefunction overlap and thus a large quantum mechanical optical transition matrix element.

Impure materials, such as doped material or one possessing lattice defects, can acquire new states in the forbidden gap. Carriers can relax or be trapped in these states with a recombination dominating the luminescence spectra at low temperatures. Radiative recombination from such levels cause a photon with an energy level equal to that of the difference in energy between the initial and final states to be emitted. This emitted photon is detected as PL light.

There are many different types of radiative recombination processes. Figure 2.11 shows the electron-hole radiative recombination processes across the band gap. Each of these transitions will result in a photon being emitted from the substrate. These

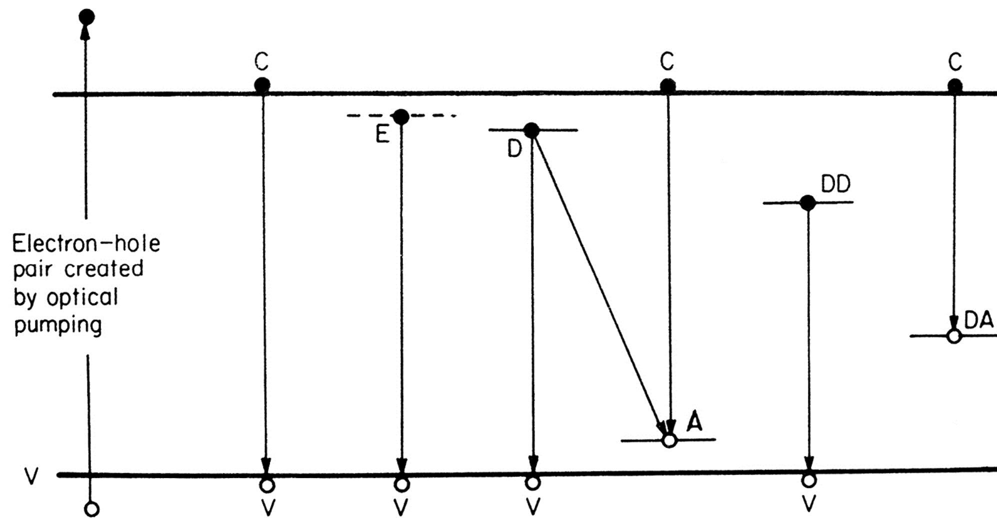

Figure 2.11 *Electron-hole pair recombination processes across the band gap where C is the conduction band, V is the valence band, E is the exciton position, D is neutral donors, A is neutral acceptors, DD is deep donors and DA is deep acceptors [84]*

transitions are:

C → V processes. Transitions from the conduction band to the valence band within the material. These are typically seen at high temperatures, sometimes at room temperatures as well.

E → V processes. Exciton decay which is only seen in very pure materials and at low temperatures when kT is less than the exciton binding energy. There are two types of decay which can occur, decay of free excitons and the decay of excitons bound to impurities. For free excitons it is the polariton states which decay. Polariton states occur when there is an interaction between the radiation and the free exciton which causes these resonant states to couple together. Two states are formed, slightly separated in energy, each of which contains some exciton characteristics and some photon characteristics. Each of these states has two levels which are slightly separated

in energy and in the energy of the emitted photon upon decay. Bound excitons occur if an exciton stays localized in the vicinity of an impurity. The energy will be less than the energy of the free exciton by the amount of the binding energy of the exciton to the impurity. This is typically quite small of the order of 0.001 eV and can be determined by the energy gap between the emitted photon and the free exciton position.

D → V processes. This transition takes place when the loosely bound electron on a neutral donor recombines with a hole in the valence band. The energy of such a transition is the band gap energy minus the donor energy (E_g – E_D). Transitions on donors with large ionization energies will occur well below the energy of the band gap and are illustrated as DD → V processes in figure 2.11.

C → A processes. An electron in the conduction band of the semiconductor drops to an acceptor atom, ionizing the acceptor. Similar to the previous process, the energy of such a transition is the band gap energy minus the acceptor energy (E_g – E_A). Transitions from the conduction band to deep acceptor centres will occur well below the band gap and are illustrated by the C → DA processes in figure 2.11.

D → A processes. Provided both donors and acceptors are present within the material at sufficient quantities, it is possible for transitions to take place where an electron leaves a neutral donor and moves to a neutral acceptor. After this transition both the donor and the acceptor will be ionized and the binding energy will be related to the Coulombic interaction between donors and acceptors in the following manner [84]:

$$E_b = -\frac{e^2}{\varepsilon_S \varepsilon_0 r}$$

Eqn 2.20

where r is the distance between the donor and acceptor, e is the magnitude of the electric charge, ε_0 is the permittivity in a vacuum and ε_S is the dielectric constant of the

semiconductor. The energy of this transition will be $E_g - E_D - E_A - E_b$. There will be different allowed values of r which should result in a series of several sharp lines, sometimes with phonon sidebands accompanying these transitions. These characteristic features will be discussed in the results section for PL in chapter 5.

In addition to the radiative recombination processes there is another type of recombination known as non-radiative (NR) recombination. NR recombination consists of the excited state energy being converted to the vibrational energy of lattice atom, i.e. phonons. This causes the electron energy to be converted to energy forms other than light at the desired photon energy. NR processes are not desired for photonic applications and have two common causes, defects in the crystal structure and multi-phonon emission. Defects include unwanted foreign atoms, native defects, dislocations and any complexes of such defects. Each of these may cause one or more energy levels to form in the forbidden gap of the semiconductor. If close to the middle of the gap, these energy levels can be efficient NR recombination centres. These deep levels can result in luminescence quenching [81]. At higher temperatures trapped excitons/carriers are thermally released from defects and become mobile. They can diffuse through the crystal and encounter various defects, each of which increase the probability of NR recombination at such defects. Thus at higher temperatures the material's optical emission efficiency generally reduces.

2.4.2 Fourier Transform Equipment

To observe the photoluminescence spectroscopy (and the reflectance discussed in the next section) of the CuCl thin films, the samples were cooled for several hours from 300 K to 20 K in a Janis CCS-500 closed-cycle cryostat. The temperature was controlled using an Oxford Instruments ITC-4 controller, resistive

heater and a 27 Ω rhodium-iron resistance sensor located on the sample holder. The source of excitation is the 325 nm HeCd line of a Kimmon IK Series laser with a power level of ~40 mW left unfocused on the sample. Photon detection was provided by a Bomem DA8 FT spectrometer which was previously fitted with a Hamamatsu R1913 photomultiplier (PM) tube and the PM output subsequently matched to the spectrometer using a Bomem variable gain preamplifier.

The spectrometer is a Fourier Transform (FT) spectrometer based on a Michelson Interferometer. Unlike prism or grating spectrometers, FT spectroscopy does not spatially disperse different wavelengths. As shown in figure 2.12, from the entrance aperture the light is split into two beams by a beamsplitter. A fixed mirror is used to reflect one beam and the other beam is reflected by a moving mirror to produce a phase difference between the beams. When the two beams recombine at the beamsplitter the resultant interference pattern caused by the phase difference is detected as a function of mirror position.

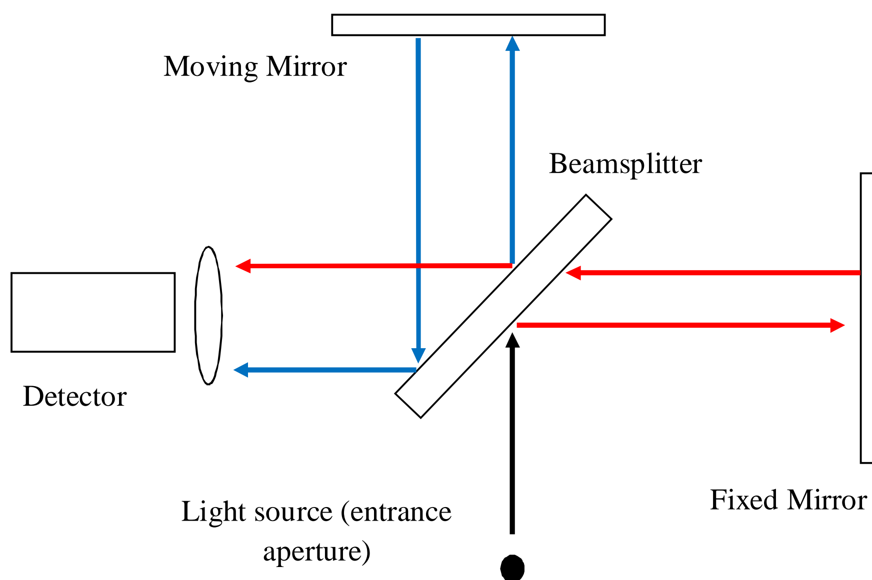

Figure 2.12 *Michelson interferometer setup used inside the FT spectrometer*

For a monochromatic light source, after passing through the beamsplitter the electric field of the separated light waves can be described by:

$$E_1 = E_0 \sin(kx - \omega t) \qquad \textit{Eqn 2.21}$$

$$E_2 = E_0 \sin(kx - \omega t + \phi) \qquad \textit{Eqn 2.22}$$

where ϕ is the relative phase of the two waves, E_0 is the electric field amplitude and k is the wavenumber related to λ by:

$$k = 2\pi/\lambda \qquad \textit{Eqn 2.23}$$

ω can be expressed as $2\pi f$ where f is the frequency of light. If we refer to the position of the moving mirror *A*, relative to the fixed mirror *B*, as *D/2* and define *D/2=0* when the path lengths are equal (known as the Zero Path Difference (ZPD) point), the number of additional wavelengths travelled by the light in path *A* as the mirror is can be expressed as:

$$N = \frac{2D}{\lambda}$$

Eqn 2.24

To convert this to a phase angle in radians, we multiply by 2π, and obtain the phase angle in terms of D as:

$$\phi = \frac{2\pi . D}{\lambda} = k . D$$

Eqn 2.25

Addition of the two light beams given by the equations 2.21 and 2.22 gives us the equation of the electric field of the resultant wave and can be expressed as:

$$E_T = E_1 + E_2$$

$$E_T = E_0[\sin(kx - \omega t) + \sin kx - \omega t + \phi]$$

$$E_T = 2E_0 \sin\left(kx - \omega t + \frac{\phi}{2}\right) \cos\left(\frac{\phi}{2}\right)$$

Eqn 2.26

By taking the time average of the electric field squared the light intensity can be obtained:

$$I = \langle E_T^2 \rangle = E_0^2 + E_0^2 \cos(k.D) \qquad \textit{Eqn 2.27}$$

where the phase ϕ has been converted to *k.D* as in equation 2.25. This shows us that the detector intensity varies in a cosinusoidal manner as a function of mirror movement *D* with a period determined by the wavelength of the source (through *k*).

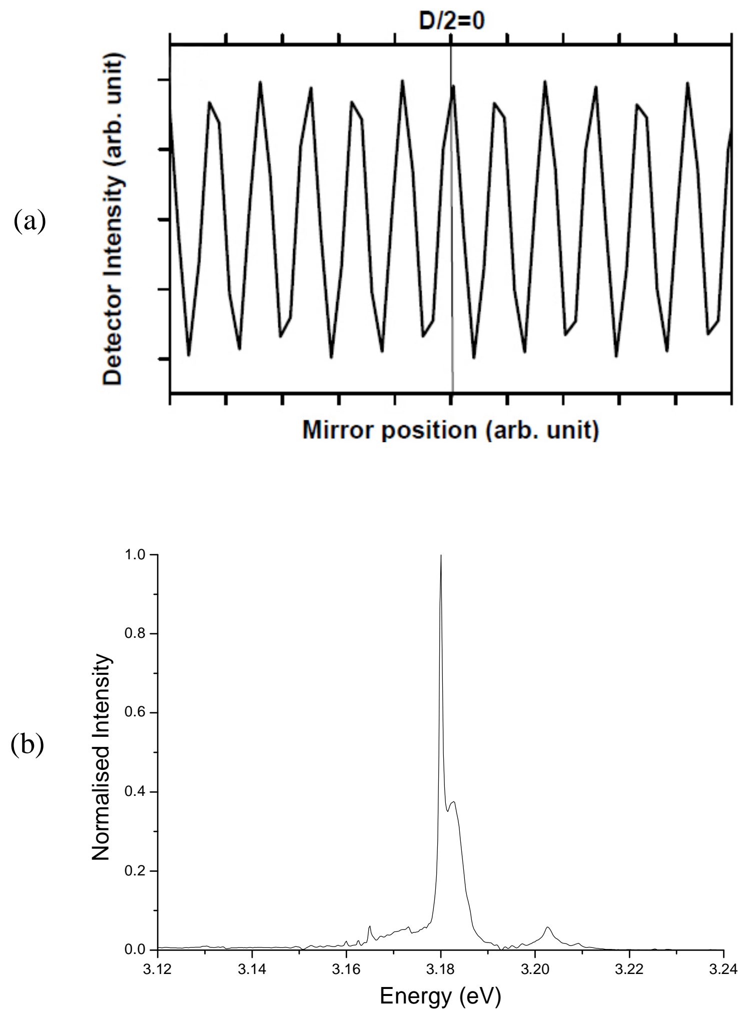

Figure 2.13 *(a) Example of the interferogram of CuCl thin films at 20 K (b) Spectrum obtained from (a) by performing FT on the interferogram*

The plot of detector intensity versus the mirror position is called the interferogram. We can see an example of this in figure 2.13 (a) for quasi-monochromatic light. If the light source contains more than one monochromatic light output then each of the wavelengths will produce a cosinusoidal signal in the interferogram with each having characteristic periods as the mirror moves. Hence the total interferogram is obtained by adding or integrating each of the cosinusoidal contributions over the entire source spectrum, all of which add coherently.

So for a continuous wavelength distribution in the source across the spectrum we obtain:

$$I(D) = \int_{-\infty}^{+\infty} I(k)\,(1 + \cos(kD))\mathrm{d}k$$

Eqn 2.28

where *I(k)* represents the source spectrum. Decomposing this interferogram into its cosinusoidal signal will give us the source spectrum. By using FT we can decompose an arbitrary interferogram into its cosinusoidal components. If we perform FT on the varying section of equation 2.28 we obtain:

$$I(k) = \int_{-\infty}^{+\infty} I(D)\cos(2\pi k.D)\,\mathrm{d}D$$

Eqn 2.29

This equation will decompose the interferogram into its constituent cosinusoids and give the original spectrum, an example of which is shown in figure 2.13 (b).

In the above description it is assumed that the limits of the FT integral extend from $-\infty$ to $+\infty$ i.e. that mirror *A* has an infinite range of motion. Practically however this is impossible and so the integral must be confined and is performed over the actual range the mirror can travel. As a result the minimum resolvable linewidth the

instrument would yield when illuminated by an ideal monochromatic source is given by:

$$\Delta k \cong \frac{\pi}{D_{max}}$$

Eqn 2.30

with D_{max} being the maximum distance the mirror can move.

As computing technology has progressed, the systems available are capable of calculating the resulting FT spectra in mere seconds. The data is stored in digital form with different functions offered by the attached software. The user can choose to record multiple interferograms of a given sample which are then averaged to increase the signal to noise ratio of the resultant spectra. Crucial throughout this process is the dynamic alignment of the mirrors. The fixed mirror must remain parallel, to within a fraction of the wavelength of light under study, to the moving mirror as it is scanned. At wavelengths typical of semiconductor luminescence, a separate light source must be used for alignment. In this equipment this is a single mode He-Ne red laser of 633 nm wavelength. The interference pattern of the laser is incident on a photodiode array with the signal from this array used to control two servo motors. These in turn adjust the angle of the fixed mirror to maintain system alignment throughout the scan.

The instrument must also determine the zero path difference (ZPD) position. To accomplish this, a broadband ‘white’ light source is used and introduced along a similar optical path as the external light, though it is detected separately. Although this broadband light source will theoretically introduce a virtually infinite number of cosinusoidal patterns to the interferogram, each with a different period due to the different wavelengths entering the spectrometer, at the ZPD position *all* wavelengths will undergo constructive interference. This is caused by the path lengths from each

arm of the interferometer being identical. A burst of signal will be detected at the ZPD point enabling its location to be established with a high level of accuracy.

Since reflectance spectra are obtained by shining a high intensity light source onto the sample and collecting the reflected light through the spectrometer, high intensity input will cause the ZPD position to be lost. This can be overcome by limiting the range of wavelengths incident using an optical filter, but this in turn limits the spectral range capable of being detected by the equipment. Throughout the course of the reflectance testing a Xe light source was used for reflectance. The high intensity this emitted caused the ZPD to be lost frequently and eventually proved unworkable as the optical filters required to obtain spectra using this light source restricted the range of detectable light to the extent that detail at lower energy values was being omitted, specifically the Fabry-Perot fringes discussed in later sections. A lower intensity Deuterium light source was used instead, with no filters required.

The system does have some key advantages over dispersive or grating monochromators. The multiplex advantage means the entire spectrum can be observed throughout the measurement of the FT spectrum, with only a fragment of this capable of being measured in a normal monochromator. This is because the detector samples all of the wavelengths of emission simultaneously, whilst scanning dispersive techniques sample one signal channel at a time. This also gives the FT spectrum a signal-to-noise advantage of $\sqrt{N}$ for spectra with N spectral elements if only noise other than the photon noise is considered in the detector. Although photon noise can be significant, the ability to quickly take a snapshot of the spectra can be very useful, especially if measuring the exciton positions as temperature is changing.

Another advantage of the system is the throughput advantage which means the solid angle of collection for the interferometer is much larger than that for a

monochromator of the same spectral resolution. This is because the width of the entrance slit must be two to three orders of magnitude smaller than the diameter of the aperture used in the interferometer to obtain the same high spectral resolution.

Other advantages of the system include the ease of calibration and use. A broad spectral range can be measured, the machine has a high degree of spectral accuracy and a high level of resolution. Each of these settings can be changed within the software or gauges on the device with no other setup required. This allows multiple spectra focussing at different wavelength positions and at varying resolutions to be recorded with a minimum of configuration changes, ideal for fine tuning spectrum output to a high standard.

The setup used to record PL data is shown in figure 2.14 with the method of illumination in this case being the 325 nm HeCd line of a Kimmon IK Series laser with a power level of ~40 mW unfocused on the sample. The aperture shown in front of the laser itself is for safety purposes only, closing upon room entry if a security code is not entered. The laser is reflected onto the sample via a mirror but is otherwise uninhibited until contact with the sample. At the exit window of the cryostat a collimating lens is

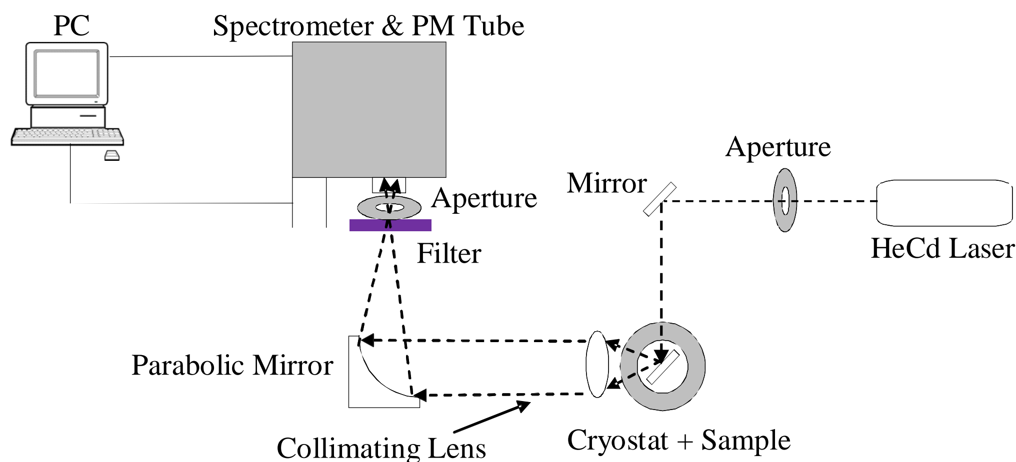

Figure 2.14 *Experimental arrangement for photoluminescence spectroscopy*

in place to collect the luminescence with a parabolic mirror bringing the light into focus at the spectrometer entrance aperture. The sample is positioned at such an angle that the effect of directly reflected laser light is negated. Samples were tested from room temperature down to approximately 20 K.

2.4.3 Reflectance

Reflectance spectroscopy is another useful technique in the study of thin films as it allows one to deduce exciton energies, resonant damping/broadening parameters and understand the effects of strain and other perturbations [85]. The dielectric constant of semiconductor films varies strongly close to the free exciton energies and thus can lead to characteristic reflectance anomalies. These effects are of major importance in characterising the CuCl samples and determining their suitability as optoelectronic devices.

Figure 2.15 shows the experimental setup for the reflectance spectroscopy measurements. The intensity of the light from the Xenon lamp is controlled by the adjustable aperture placed in front of the light source. To concentrate the intensity to a

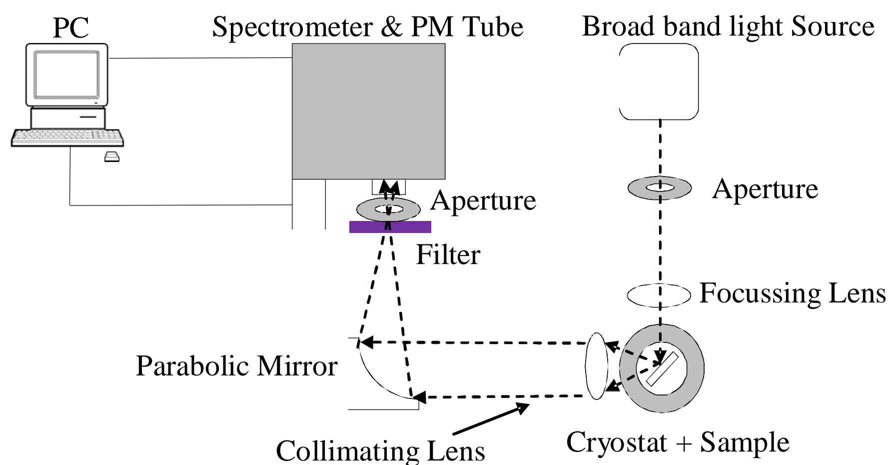

Figure 2.15 *Experimental arrangement for reflectance spectroscopy*

small area on the sample a focussing lens with a short focal length is used. The reflected light is collected by the collimating lens and a parabolic mirror brings the light into focus at the aperture of the entrance to the spectrometer.

To examine the exciton region of CuCl which has photon energies corresponding to wavelengths of around 380 nm an ultraviolet bandpass glass filter (in this case UVG-5) was used for scans using the high intensity Xe lamp. This restricted the wavelength of the light incident on the entrance aperture to the region of importance. Due to the 45º angle of incidence, both transverse and longitudinal sample modes affect reflections from the sample. Although this complicates the analysis of the spectra, there is enough separation between the transverse and longitudinal resonances in CuCl that they can be clearly distinguished on the resultant graphs. The use of focussing optics further increases the signal to noise ratio.

The cryostat sample holder can hold up to three samples at once provided the samples are either cut or grown to a width of 5 mm as this is the width of the triangular holder the samples are affixed to. This enables each of the three samples to be tested with the same optical (and other) conditions. The holder is not perfectly central in the cryostat and thus there are small misalignments upon changing samples meaning that the reflected light may not be focussed onto the entrance slit of the spectrometer. Provided the relative distance between the aperture in front of the Xe light source, the focussing lens and the collimating lens remains unchanged, the reflected light can be steered by making minor adjustments to the horizontal and vertical positions of each of lenses to ensure the maximum signal is incident on the entrance aperture. Upon running several scans at different horizontal and vertical lens positions it was found that the exciton energy positions remained unchanged with the only variance being the signal to noise ratio and reflected intensity.

The spectral characteristics of the Xenon light source are similar to that of the internal white light source used by the spectrometer to locate the zero path difference (ZPD) of the system. The PM tube is easily saturated by the high intensity of the light coming from the Xe lamp. A bandpass filter is used to limit the range of the wavelength of light entering the machine which alters the spectral characteristics enough so that it won't cause any interference, but the level of intensity can still be too great for the machine to cope with. The variable apertures in front of the source and at the entrance to the spectrometer are used to attenuate the signal. A voltmeter is attached to the spectrometer to display the current intensity entering the spectrometer as the adjustments are made. A suitable level on the voltmeter was found so that the optical signal will not saturate the PM tube cross leakage with the ZPD source requires constant vigilance and attention. To combat these issues, in later work the xenon light source was replaced with a deuterium source which has a similar spectral range. This operates at a much lower intensity but still sufficient to produce the reflectance spectrum with the required signal to noise ratio.

When reflectance is to be performed using the deuterium lamp, adjustments must be made to the setup to account for the reduction in intensity. Instead of an aperture being used to limit the light incident on the sample, the light source is placed much closer to the cryostat and a focusing lens used to maximize the intensity further. The collimating lens at the exit slit must be adjusted quite carefully to ensure the signal remains as high as possible. The filter used for the Xe lamp was removed to maximize the intensity of the reflected deuterium light. The important features of the spectra of CuCl could still be determined with a similar resolution and scan number used for all samples once these alterations were made.

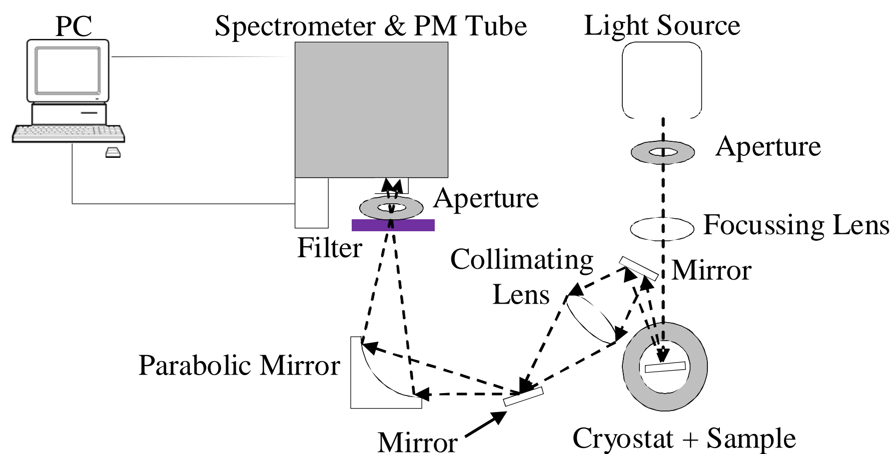

Figure 2.16 *Experimental arrangement for reflectance spectroscopy at normal incidence*

For comparison scans were also performed at normal incidence using the setup shown in figure 2.16. After impinging on the sample, the light is reflected back towards the source but at a slight angle, hitting a mirror positioned slightly off-centre (~5˚). This mirror reflects the light through a collimating lens and onto another mirror. The light is then directed towards the parabolic mirror which focuses the light through the aperture and into the spectrometer. Despite the addition of several mirrors to the setup, intensity was not an issue and spectra of similar quality to those obtained from the 45˚ setup were obtained.

2.5 Electrical Properties

2.5.1 Scanning Electron Microscopy

The scanning electron microscope (SEM) functions by directing a beam of electrons at the specimen and observing the various outputs from the sample and their spatial variation as the beam scans, which is used to build the image. The SEM is

primarily used to study the surface, or near surface structure of bulk or thin film specimens. The technique is suitable for thin film analysis as the accelerating voltage of the incident electrons can be altered to restrict the penetration depth to the film and not the host material.

The electron source is usually of the tungsten filament thermionic emission or lanthanum hexaboride type. The electrons are accelerated to energy between 1 keV and 30 keV which is considerably lower than the other major category of electron microscopy, transmission electron microscopy (TEM), which typically uses electrons with energies in the range of 100 – 300 keV. Several condenser lenses demagnify the electron beam until it hits the specimen with a spot size of diameter 2 – 10 nm, which can be altered by the user within certain bounds.

As shown in figure 2.17, this incident electron beam causes a variety of different signals to be outputted from the specimen. Incident electrons may be backscattered from the sample with little or no energy loss or they may lose some

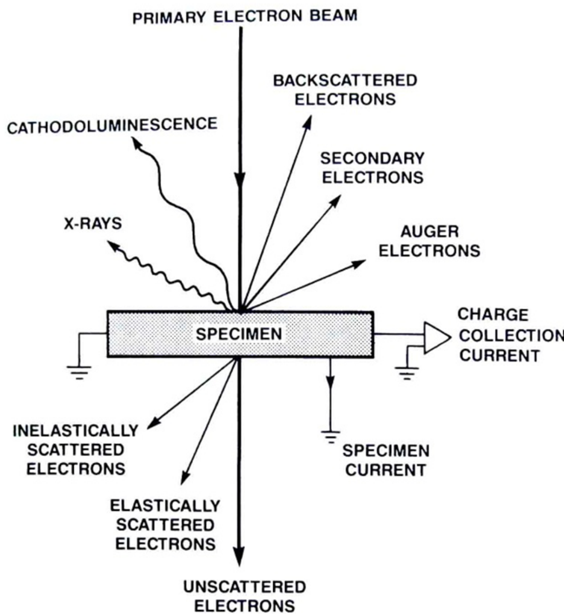

***Figure 2.17** – Schematic diagram of the types of signal resulting from an electron beam interacting with a solid [86]*

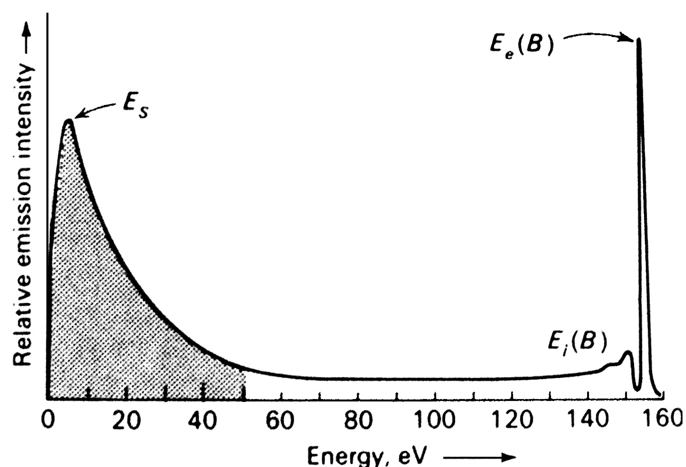

Figure 2.18 *Energy distribution of electron emission from Ag. E_s represents the secondary electron peak, E_i (B) the inelastically scattered near surface emissions such as Auger electrons and E_e (B) the elastically scattered (backscattered) energies [87]*

energy and produce secondary electrons by knocking out electrons from atoms in the sample. These secondary electrons are characterized by their relatively low energy in comparison with the incident electron energy and the energy of the backscattered electrons. As a general rule electrons are classed as secondary electrons if their energy is less than about 50 eV. The scale of these energies is shown in figure 2.18 for Ag, but is of a similar scale for CuCl and other materials as well.

The excess energy introduced by primary electrons into the material may also lead to electronic excitation, including inner shell excitations and excitations across the bandgap. The former mode of excitation leads to the emission of characteristic X-rays which allow the material chemical composition to be studied by energy dispersive x-ray spectroscopy (EDX), detailed in section 2.5.3. The latter mode of excitation results in the generation of electron-hole pairs and the subsequent emission of photons in the ultra-violet, infrared and visible spectral ranges and is commonly known as

cathodoluminescence (meaning luminescence generated by a cathode ray, i.e. electrons, CL) and is detailed in section 2.5.2. Different detectors are used to record the signals from secondary electrons, backscattered electrons, CL etc.

The most common imaging mode of the SEM uses the secondary electrons emitted from the sample, and is an imaging mode used routinely in this work. The secondary emission yield for a solid is characterized as the ratio of secondary electron current to primary electron current as defined by:

$$\delta = \frac{I_S - I_B}{I_O - I_B}$$

Eqn 2.31

where I_S is the secondary emission current, I_B is the backscattered electron current and I_O is the primary electron current. The secondary electrons originate from the top few nm of the sample surface due to their low energy and consequent small escape depth of the < 50 eV electrons. The secondary emission yield depends almost solely on the

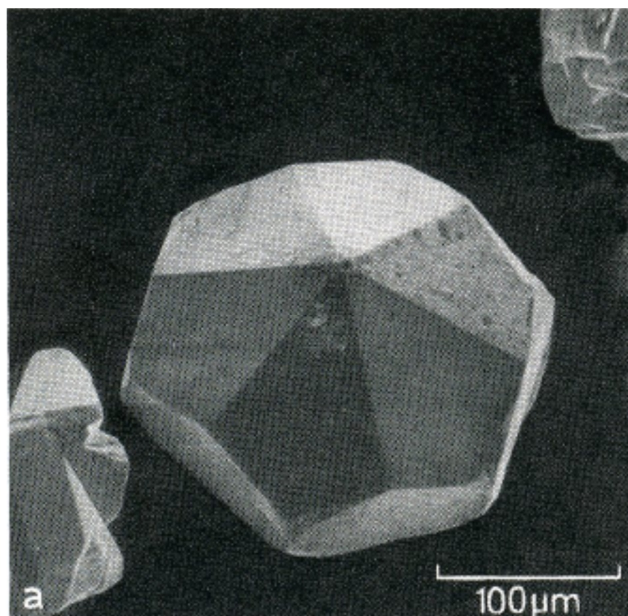

Figure 2.19 *Secondary electron image showing the detailed surface topography of an imaged sample*

primary electron energy, the density and, most importantly the sample surface topography (and to a lesser extent the crystallography of the emission surface as the work function changes). Thus, for a single scan across a reasonably homogeneous surface under constant primary beam energy, the secondary electron imaging mode depends mainly on local surface topography. An example of this is shown in figure 2.19. The other main mode in which the SEM system was used in the present work is the CL-SEM mode, as discussed next.

2.5.2 Cathodoluminescence SEM (CL-SEM) Imaging

This technique involves the analysis of photon emission from a luminescent material excited by a beam of high energy electrons due to bandgap excitations of excited electron hole pairs. This can provide both lateral, spatially resolved information due to the small electron spot size and scanning modality and also depth-resolved information on the structure of the solid by varying the primary electron beam energy and thus the penetration depth of the primary electrons in the material and the excitation volume. Various properties of a material can be investigated with a spatial resolution down to 1μm or less such as (a) the composition of the compounds, (b) the location of the luminescent centre concentrations, (c) electronic properties such as surface recombination velocity and carrier diffusion length via the dependence of cathodoluminescence (CL) intensity on electron beam voltage and related properties such as minority carrier lifetime using time-resolved CL measurements and (d) extended defects such as dislocations from CL maps of the surface of the material. As well as being used to characterize the properties of the material, CL gives a good indication of the overall luminescence efficiency of the material and thus the viability of the material as a component of light emitting devices.

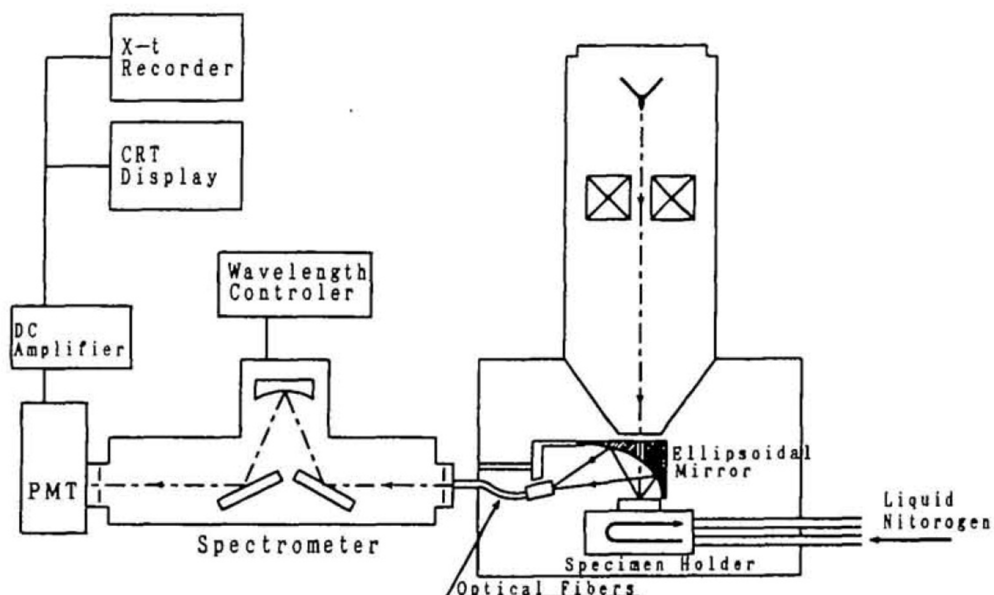

Figure 2.20 *Schematic showing the layout of an SEM with CL equipment attached [88]*

The technique of CL imaging may in principle be performed in a variety of electron microscopes, including scanning electron microscopes (SEMs), scanning transmission electron microscopes (STEMs), or transmission electron microscopes (TEMs) equipped with CL detecting systems. There are however significant differences between SEM, STEM and TEM-based systems due to the nature of the electron lens configurations and ease of optical access to the sample. For this reason the majority of CL systems are based on SEM instruments due to the larger sample chambers of such systems and the ease of installing larger optical collection systems. The CL of the samples discussed in this report was performed using an SEM with a mirror and monochromator attached to collect the outputted CL signal [86]. A schematic diagram of this setup is shown in figure 2.20.

The number of electron-hole pairs generated per incident beam electron is given by the generation factor [89]:

$$G = \frac{E_b(1-\gamma)}{E_i}$$

Eqn 2.32

where E_b is the primary electron beam energy, E_i is the ionization energy and γ represents the fractional electron beam energy lost due to the generation of backscattered electrons or other excitations in the crystal such as inner shell excitations. E_b can be adjusted in the SEM software, E_i is typically 3.395eV at 4K for CuCl [26] and γ is ~0.66. [89]. Using these known parameters it is clear that the number of electron hole pairs generated is dependent on the beam voltage present in the electron beam as the other factors will remain constant for each sample.

The second aspect of the CL emission which is strongly affected by the primary beam voltage is the region from which the emission is generated, due to the varying penetration depth of the beam with beam voltage. A general equation for the penetration depth as a function of primary beam voltage was derived by Kanaya and Okayama [90] and found to agree well with experimental results for the penetration depth of the electron beam into a variety of materials. This equation is:

$$R_e = \left(\frac{0.0276A}{\rho Z^{0.889}}\right) E_b^{1.67} (\mu m)$$

Eqn 2.33

where E_b is the primary electron beam energy in keV, A is the atomic weight in g/mol, ρ is in gcm^{-3}, and Z is the atomic number. The atomic weight is 98.99 g/mol for CuCl, ρ is 1.90 gcm^{-3} (which was also used for the tooling factor as described in section 2.2.1), Z is the total atomic number which for CuCl is 46. The shape of the generation volume within the material is dependent on the atomic number, varying from a pear shape for a material with a low atomic number, to a spherical shape for $15 < Z < 40$ and a hemispherical shape for higher atomic numbers. With an atomic number of 14 Si

corresponds to a situation between the pear and spherical shapes, whilst with an atomic number of 46 CuCl should be better described by a hemispherical shape. This is quite difficult to see from the simulations below however, even when substrates of pure Si or CuCl are selected. CL emission occurs from the entire interaction volume of the electron beam with the sample, unlike the secondary electron or backscattered electron signal [91].

From these two equations we can see that the SEM can be used for depth-resolved CL studies as the penetration depth of the electron beam (E_b) and intensity of the CL signal can be varied by adjusting the charge of the electron beam. This allows changes in optical properties of the material to be probed as a function of distance from the surface.

Figure 2.21 shows the results of a Monte Carlo simulation program [92] for a 500 nm thin film of CuCl on a Si substrate using the density of 1.90 gcm^{-3} which is taken as previously mentioned. The primary electrons are represented by the blue lines in the material and the backscattered electrons by the red lines with the penetration depth calculated using the aforementioned Kanaya and Okayama equation. For 500nm of CuCl on Si the E_b required to fully penetrate the 500 nm was calculated to be 4.0778 KeV. The simulations, from (a) to (d), show the gradual increase and spread of the electrons within the surface of the thin film until they reach the boundary between CuCl and Si at 500 nm. The penetration depth from the Kanaya-Okayama equation represents the greatest extent of the interaction volume into the material. The simulation shows reasonable agreement with the equation. As the electron beam energy is further increased up to 15 KeV, we can see that most of the electron energy is deposited within the Si layer rather than the CuCl. At the higher beam energies the electrons are mostly bypassing the CuCl layer entirely to deposit in the Si substrate.

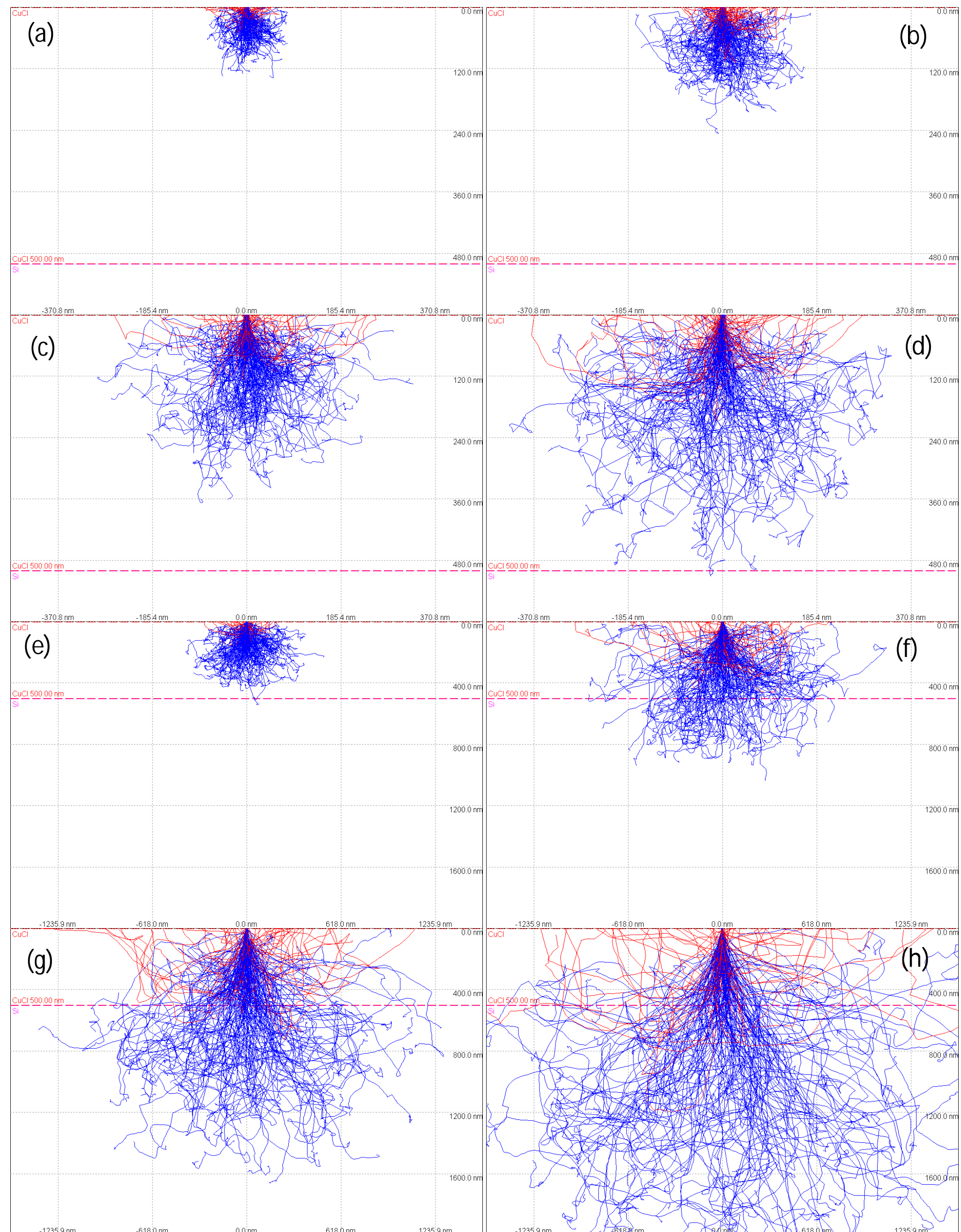

Figure 2.21 *Monte Carlo simulations for electron trajectories onto a 500nm CuCl sample at increasing accelerating voltages (keV); (a) 2 keV, (b) 3 keV, (c) 4 keV, (d) 5 keV (e) 5 keV, (f) 7.33 keV, (g) 11.67 keV, (h) 15 keV. The dotted line shows the border between CuCl and Si with the CuCl at the top. The total depth of the (a) – (d) is 600 nm and (e) – (h) is 2000 nm. [92]*

For the CL scans this will not affect the measured spectrum as there is a very low CL signal from Si (due to its indirect bandgap nature) and thus the measured emitted photons will still arise entirely from the CuCl layer as desired. However as the beam energy is increased, the broader interaction volume will degrade the resolution for imaging and thus generally the lowest possible beam energy which excites the entirety of the film is used to study CuCl thin films.

CL scans were performed at room temperature using a LEO Stereoscan 440 SEM with an attached CL mirror and micrometer shown in figure 2.22. The samples were excited with the electron beam set to < 15keV (chosen depending on the sample details) and a probe current of typically 1.1 nA.

Figure 2.22 *CCD image of the SEM system used for measurement. The attached CL and EDX equipment can be seen on the left side of the picture*

The CL mirror placed inside the vacuum chamber is parabolic in shape with a 1mm hole in the top which allows the electron beam to pass through. The electrons impinging on the sample excite luminescence and whilst some of this escapes through the entrance hole, the mirror has a large solid angle of collection and thus a high collection efficiency of ~75% [93]. The focal length of the mirror is also 1 mm so great care is taken when aligning it with the substrate to prevent contact with the SEM lens pole-piece. Once the photons are collected by the mirror they are transferred via optical fibre bundle to the Gatan MonoCL monochromator with a 1200 lines/mm grating and photomultiplier tube which captured the spectra. The resolution of this monochomator is approximately 1 nm. The samples analyzed using the SEM in DCU were all made using the deposition technique described in section 2.2.

2.5.3 Energy Dispersive X-ray Spectroscopy

Similar to CL, this technique involves the analysis of emissions from the surface of the substrate when an electron beam is focussed upon it such as within an SEM. In this case however, we are monitoring the characteristic x-rays emitted from the material rather than the UV/visible light monitored for CL. These x-rays are characteristic of the material they are emitted from and can thus be used to identify the element source. As shown in figure 2.23, the X-rays emitted from the sample come from the entire interaction volume, similar to CL and different from secondary electrons and thus there may be a large signal from the substrate, in many cases larger than from the thin film itself. Once again, similar to CL, in our case this does not cause difficulties because the elemental composition of the thin films does not overlap with that of the substrate, and the characteristic x-rays from the thin film have distinct energies/wavelengths.

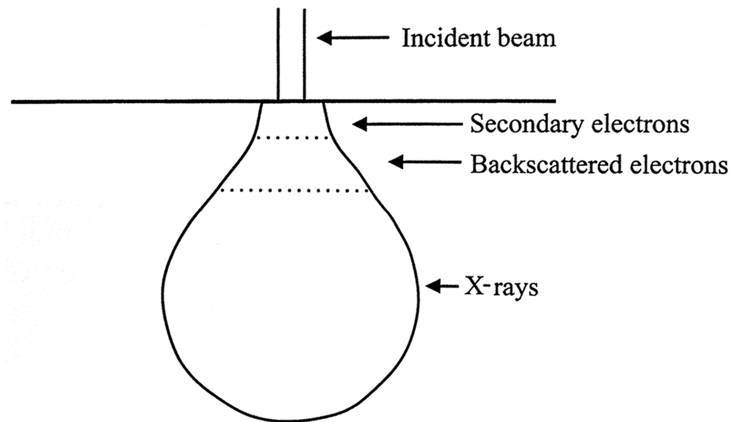

***Figure 2.23** The interaction volume and the regions from which secondary electrons, backscattered electrons and X-rays may be detected [94]*

The setup used for energy dispersive X-ray spectroscopy (EDX) was a scanning electron microscope and a Princeton Gamma Tech energy dispersive X-ray analyser with a silicon (Li) detector. The Li window covering the Si detector absorbs low energy X-rays and therefore light elements such as hydrogen cannot be detected by this technique. The high efficiency of the EDX detector coupled with the relatively large collection angle means that data can be collected quite rapidly at low beam currents, typically within only a minute or two.

There are a couple of disadvantages with this technique, one being that the energy resolution of the detector is quite poor, meaning that each X-ray line is not detected as a sharp line, but rather as a broad peak typically 100-200 eV wide. This makes it almost impossible to resolve closely spaced lines and sometimes results in quite a low peak to background ratio. Also, under certain circumstances erroneous peaks in the spectrum can be produced. The most common of these effects is the sum peak and the silicon escape peak. The sum peak is a result of two identical photons entering the detector simultaneously resulting in a single peak of their combined

energy being recorded instead of two counts of their actual energy. The silicon escape peak is due to an incident X-ray knocking out a K-shell electron within the silicon in the detector crystal. The original X-ray photon loses 1.74 keV in energy (the energy of the SiK_{α} X-rays) and a peak 1.74 keV below the actual X-ray peak is produced. However as long as the user is aware of these effects and considers them in subsequent analyses, this technique can be used to characterize the material structure of the samples quite effectively.

2.6 Summary

Throughout this chapter we have discussed the different types of deposition performed and the various methods of analysis used to characterise the resultant samples. Although both thermal evaporation deposition and LPE are detailed, each of the samples used for analysis in the following chapters were produced using the former technique. The LPE setup proved problematic with the CuCl melt failing to adhere to the surface in a uniform manner and instead forming globular clusters of material across the surface. For this reason the setup was not used for sample deposition but the KCl doping used by the process to lower the melting point of CuCl was investigated as initial experiments on the addition of the KCl salt showed an increase in the measured intensity at each of the exciton locations [95].

The theory behind the methods of characterisation used in the following chapters was also discussed. The X-ray diffraction process allows us to analyze the orientation and size of the CuCl crystallites within our thin films and to look for the presence of KCl material, either in KCl form or as part of the K_2CuCl_3 compound. Glancing angle scans can also be used to examine the polycrystalline nature of our

samples. The main disadvantage with this technique is the exposure of the material to the atmosphere throughout the process. Due to the hygroscopic nature of CuCl, the structural properties will be deteriorating as the scans are performed. A capping layer was found and will be discussed in the following chapter, but this effects the optical properties of the material and limits the testing of a single sample across multiple methods of characterisation.

The theory involved in the optical properties of CuCl follows this section. This includes both photoluminescence and reflectance, both of which are performed in the same low temperature cryostat setup using a Fourier transform spectrometer to record the resultant spectra. Both of these methods allow the values of the exciton energies to be measured. the distinction being that PL also records the biexciton positions which allows the binding energy to be calculated, whilst the reflectance process only records the main exciton peak values, but allows various exciton parameters to be calculated (damping, splitting, etc.) once the spectral shape has been modelled. Taking place within a controlled low temperature environment, the optical analysis should be non-destructive by nature. However, long-term exposure to the laser used in the PL measurements results in a visible scarring on the surface of the samples as well as a deterioration in luminescence intensity. Reflectance however is completely non-destructive. The results for this section are presented in chapter 5.

Finally the theory behind the analysis of the electrical properties is reviewed. Each of the methods used in this section involve the interaction of the CuCl thin films with the focussed electron beam within the SEM. Like the optical analysis, this occurs within a controlled environment, but remains at room temperature. This process provides us with a more detailed look at the surface structure of our samples in the secondary electron images and EDX imaging. SE shows us the physical structure with

the EDX supplementing these images by allowing us to determine the atomic structure of the regions imaged. CL allows us to record the Z_3 exciton location and the distribution of defects across the surface of the samples. Variance of the beam penetration depth allows us to determine whether these defects stem from the air-CuCl or CuCl-Si boundaries. This process is destructive due to the electron beam interaction, but the effects of this are confined to relatively small areas on the surface of the samples. The results of each of the methods used in this section are presented in chapter 4. This is prior to the optical property results because the SEM was also used for physical thickness analysis to confirm the reflectance modelling at the end of chapter 5.

Chapter 3

Structural Properties

3.1 Introduction

Our characterisation of the CuCl thin films begins with the structural and morphological properties which can be determined from x-ray diffraction (XRD) scans of the surface material. First we breakdown the constituents of the samples and the scanning process, showing the $\theta/2\theta$ XRD spectra of the base plate, pure CuCl beads, KCl powder and Si samples of (100) orientation. Knowing the growth orientation of each of the components prior to their combination during the deposition process allows us to observe the alterations in their crystallography due to their interactions with each other. This also provides a more appropriate frame of reference than the ICDD database since the ICDD diffraction patterns are the result of scans of powder samples, rather than textured films. Consequently, samples of CuCl on Si are compared to these initial scans immediately after growth and again once time has passed to illustrate the deterioration of the structure due to the hygroscopic nature of CuCl. This step was repeated for a number of samples to confirm the reliability of the deposition process before proceeding. To combat the fast deterioration of the sample and thus of the XRD peaks, a capping layer was required. Nail polish [66] was applied to each of the samples prior to XRD analysis. It was confirmed by various measurements that the varnish had negligible effects on the XRD pattern. Prior to doping, the analysis of

samples which had decayed due to the presence of both oxygen and moisture was performed to illustrate the difference between the decayed and doped samples.

With the reliability of the deposition and a method to preserve structural orientation established, analysis of the doping of CuCl with KCl and O could be performed. Each of the angular values and relative intensities are compared to their measured values from powder diffraction according to the International Centre for Diffraction Data (ICDD) provided by the XRD manufacturer. Various alternative setups and scan modes are also used to analyse particular aspects of the crystal structure. Glancing Angle X-Ray Diffraction (GAXRD) is used to diminish the influence of the Si layer on the XRD spectra, with various glancing angles used to investigate the structure at different depths within the specimen. Rocking curve scans show the favourable orientations of key diffraction peaks and φ scans the crystal symmetry of the CuCl layer.

3.2 XRD Measurements on the System Base Plate

There are some unavoidable factors with the XRD equipment which may contribute their own diffraction peaks and interfere with the analysis of our results. Due to our use of thin film samples, the base plate to which the sample is attached and the tape affixing it in place must be recorded and their characteristic diffraction patterns taken into account when examining our samples. Figure 3.1 shows the results of a locked coupled scan of the base plate, with no sample in place. A locked coupled scan is similar to a 2θ/θ scan except it does not take any differences in the θ positions

into account, i.e. if θ is set to 10˚ then 2θ will be at 20˚ rather than any slight fraction above or below to account for slight alterations in crystal orientation (i.e. a 2θ/ω scan). By using this scan all the diffraction peaks from the base plate were imaged with no bias in orientation. We can see that there are 4 significant sharp peaks at 38.3˚, 44.6˚, 64.9˚ and 78.1˚ with a smaller peak at 74.4˚. If these peaks appear on any of our subsequent scans and do not match the expected XRD patterns for the materials used they can be ascribed to the base plate and eliminated from our analysis.

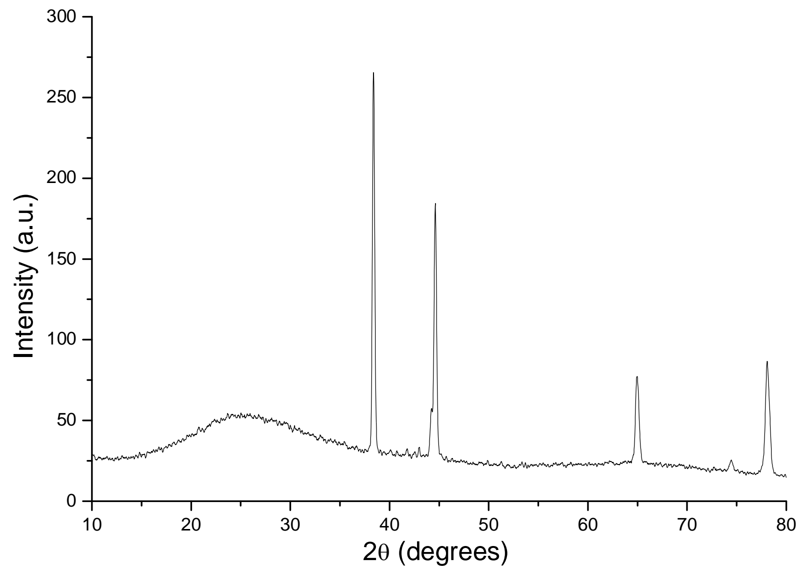

Figure 3.1 *Locked Coupled scan of the XRD machine's base plate*

With the base plate diffraction pattern established, we can add the additional elements which will be in the path of the X-ray during the analysis of our thin film samples and observe how they affect the base plate pattern. Figure 3.2 shows the effect of the double-sided tape on the base plate diffraction pattern. The four sharp peaks are unchanged, but there is an increase in the overall background reading at angles below the peak at 64.9˚ and a large broadband structure between approximately 15˚ and 27˚.

This broadband feature is quite prominent but does not directly cover the area of interest of our samples, given that the first CuCl peak of importance is at 28˚. This confirms that aside from the base plate, there will be no additional diffraction peaks formed by the tape in the region of interest so any peaks observed will be from the samples themselves.

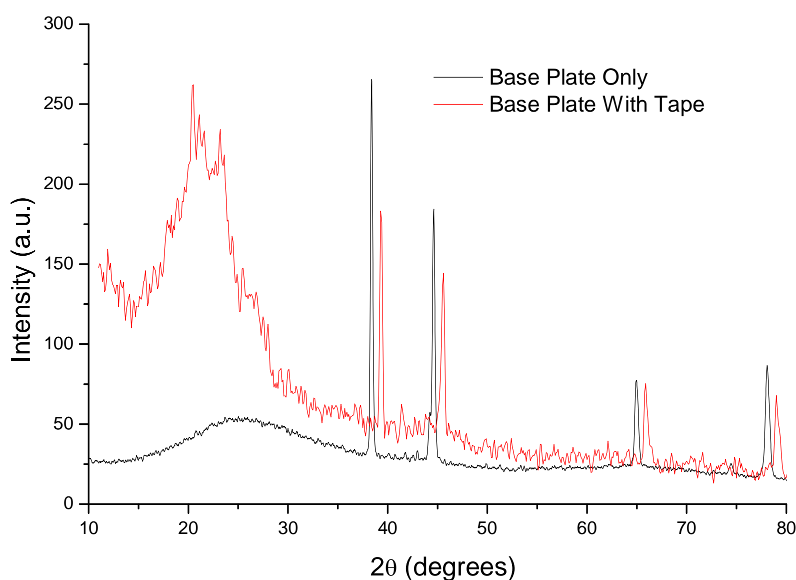

***Figure 3.2** Locked Coupled scans of the XRD machine's Base Plate with and without double-sided tape. An offset of 1 degree has been applied to distinguish the peaks. The increase in the background level is due to the samples being recorded at different exposure times. The exposure time was found to have a negligible effect on these peak values*

3.3 CuCl Sample Composition

To show the effect of the deposition process on the CuCl crystal structure, the constituent elements of the samples were examined separately. The source of CuCl used for deposition comes in miniscule pellet form, approximately 1 mm in diameter.

Several of these were attached to the stage using double-sided tape (the XRD pattern of which can be seen in figure 3.2) which will be used to attach all other samples unless otherwise stated. The diffraction pattern of the CuCl pellets was analysed using the parallel beam geometry setup in 2θ/θ mode and is shown in figure 3.3.

This graph clearly shows that the preferred orientation of the CuCl pellets is (111) which matches the orientation of peak intensity for powder samples recorded in the ICDD Diffraction Database. A comparison of the ICDD values with our recorded values is shown in table 3.1. The measured intensity percentage was calculated from the (220) peak as the (111) peak is of such a high intensity that the ratios of the other peaks are several orders of magnitude too small for a worthwhile comparison to be made with the ICDD values. For this reason they have been re-normalised to the (220) peak. The difference between the measured values and the ICDD values is probably

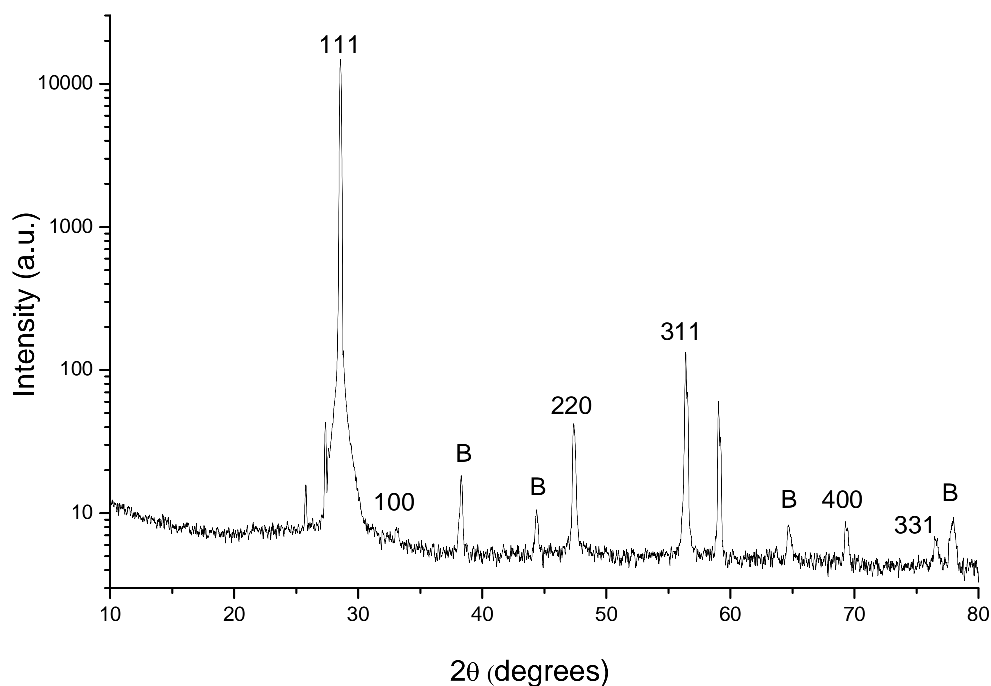

***Figure 3.3** θ/2θ XRD Diffraction Pattern for CuCl pellets. CuCl orientations are marked, with the known peaks from the base plate marked as B.*

Plane (hkl)	ICDD 2θ (degrees)	CuCl Pellet 2θ (degrees)	Diff (Exp – ICDD)	% Intensity ICDD	% Intensity Exp.	Crystallite Size (nm)
111	28.594	28.566	-0.028	N/A	N/A	62.4
100	33.027	33.094	+0.067	14	5	26.3
220	47.561	47.401	-0.16	100	100	46.1
311	56.441	56.401	-0.04	55	307	60.2
400	69.543	69.469	-0.074	11	10	67.4
331	76.813	76.603	-0.21	18	6	85.9

Table 3.1 *Expected positions and ratios of the CuCl diffraction peaks visible in figure 3.3 and their actual values.*

due to the quality of the material and the preparation involved. The ICDD diffraction values were performed on pure powdered samples. For best adhesion to the base plate the CuCl samples have been left in pellet form and not crushed into a powder. This could be a contributing factor to the disparity in these values as well as the inherent limitations of equipment accuracy.

From figure 3.3 and these calculations we can see that the (220) peak is of lower intensity than the (311) peak which disagrees with the expected ICDD values. This indicates a bias in the pellet structure, but should not affect the CuCl thin films once evaporation takes place. Of the remaining CuCl peaks there is a similar disagreement in the experimental intensity ratios between the (400) and (331) peaks.

There is one peak of note that remains unaccounted for. The peak at 58.9˚ is an anomaly and seems specific to the CuCl pellets themselves as it does not appear in scans of any other material, possibly related to impurity phases introduced during the

manufacturing process of the CuCl beads. It is also worth noting the presence of the reflected x-rays of Cu K_β that haven't been entirely filtered out to the left of the CuCl (111) peak. These are present in all of the θ/2θ scans to the left of the peak of maximum intensity no matter what material is being scanned. The higher energy value of the Cu K_β x-rays causes their appearance at lower degrees. Typically this intensity is expected to be 17% of the K_α energy [96] but in this case it is only 0.1% due to the filtering of the K_β in the x-ray source used. This indicates that it is highly unlikely Cu K_β x-rays will be detected for any other peaks. Overall the 2θ positions of the orientations are within 0.2˚ of the expected ICDD values indicating that the pellets are not significantly strained (the diffractometer angular resolution is ~ 0.1˚). The properties of the CuCl pellets can be compared to the values of our resulting thin film samples to show how the Si substrate effects the orientation of the CuCl material.

One of these properties that can be measured using these scans is the texture factor of the material. This can be used to quantify the orientation of a particular peak in the crystal structure when compared with the ICDD intensities. A value of 1 indicates complete agreement, higher values showing a degree of preferential growth and lower values a lack of preferential growth in the chosen orientation. In this case we shall calculate the texture factor for the peak of highest intensity, the (111) peak. This is calculated using the following formula:

$$T_{c(hkl)} = \frac{I_{(hkl)}/I_{0(hkl)}}{1/N\left[\sum_N I_{(hkl)}/I_{0(hkl)}\right]}$$

Eqn 3.1

where $T_{c(hkl)}$ is the texture coefficient of the (hkl) plane, I the measured intensity, I_0 the corresponding recorded ICDD intensity and N the number of preferred growth directions [97]. In this case N is 6 as the orientations (111), (100), (220), (311), (400) and (331) are all visible in figure 3.3. The texture factor is calculated to be 5.775 for

this peak. Future samples can be compared using this method to ascertain which has the most preferred orientation in the (111) plane.

The crystallite size (or more exactly the out of plane coherence length) of the orientations of CuCl orientations can be estimated by using the Scherrer formula:

$$t = \frac{0.9\lambda}{B\cos\theta_B}$$

Eqn 2.10

where t is the crystallite size in nm, λ is the wavelength of the incident x-ray (in this case 1.5405 Å), B is the full width at half the maximum height (FWHM) and θ_B is the diffraction angle (i.e. the θ angle instead of the 2θ angle). This formula is discussed in more detail in chapter 2. The size of the crystallites is such that the contribution of particle-size broadening will be too low to impinge on the accuracy significantly of this calculation. Similarly instrumental broadening due to the slit width and penetration depth can also be ignored since for the (111) peak of maximum intensity at 28˚ the $K_{\alpha 2}$ peak cannot be distinguished from the $K_{\alpha 1}$ peak meaning that the broadening due to this effect cannot be accounted for in the FWHM value. This effect will be constant for all samples so the crystallite size may be slightly larger than the calculated values but more importantly the changes in crystallite size throughout the different samples can be measured. Our values for the crystallite size are shown previously in table 3.1.

There are notably 2 peaks of extremely low intensity, the (100) peak at 33˚ and the (331) peak at 76˚. If the crystallite size of these peaks is excluded (due to their low intensity, the percentage error will be higher) we can see that for the CuCl pellets the crystallite size determined from the different XRD peaks remains rather consistent, varying between ~46 and 67 nm. The peak we're most concerned with is the (111) peak at 28˚ as this is the preferred orientation of the CuCl on the Si substrate. This value is estimated to be 62 nm for the CuCl pellets.

3.4 KCl Sample Composition

During the KCl-CuCl deposition, it is thought that the K_2CuCl_3 compound is formed and evaporated onto the surface. The phase diagram of KCl – CuCl is shown once again in figure 3.4. As the deposited material cools, it will go through the phases indicated there, along a vertical line resulting in a deposition of CuCl and K_2CuCl_3 due to the molar ratio used in the starting material (KCl 25% CuCl 75%). Even so it is likely that there would be some amount of pure KCl present in the resultant thin film and certainly the properties and preferred orientations of this source KCl material will have an effect. The source of KCl used for deposition in our KCl-CuCl samples was commercially available 99.99% purity (Sigma-Aldrich) and came in a fine powder form. A layer of this was attached to the tape in the same fashion as the CuCl pellets and the subsequent diffraction pattern recorded by parallel beam geometry setup in

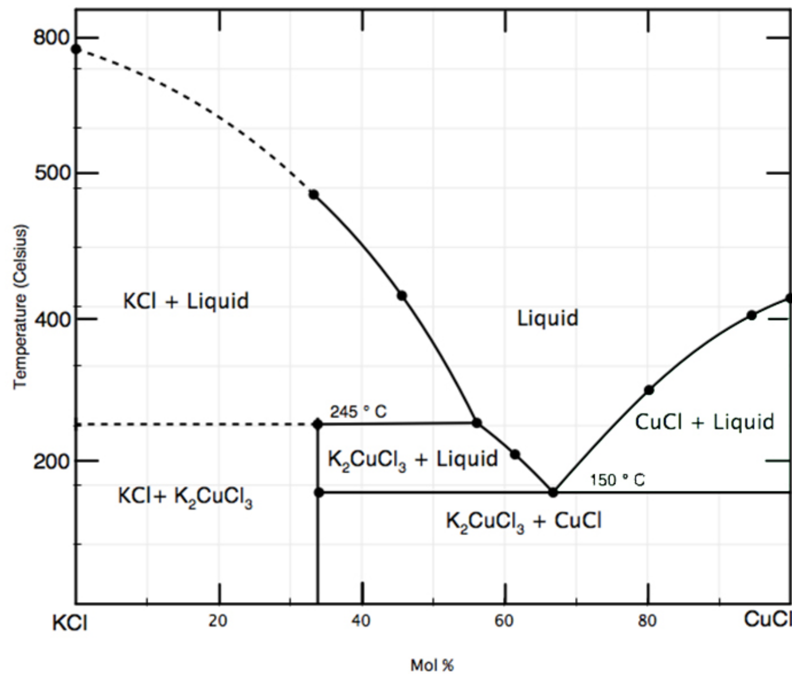

Fig 3.4 Phase diagram for KCl – CuCl

2θ/θ mode is shown in figure 3.5. As previously with the CuCl pellets, the angular positions are within 0.2˚ of the expected values and the intensity ratios are quite different from the expected ICDD values as can be seen in table 3.2. A lack of powdered samples is not the cause in this case, instead it is probably due to the exposure of the KCl material to moisture and oxygen itself. Although stored in a sealed plastic container, the KCl material was not freshly acquired. To combat this the powder was baked on a hot plate inside a glass container for several hours to reduce the levels of moisture and oxygen present before testing.

The most prominent KCl peak is the (200) peak. This has a similar angular position to the strongest CuCl pellet peak (differing by only ~ 0.25˚) but is of a different orientation to the (111) CuCl peak. If this peak was present in the KCl – CuCl

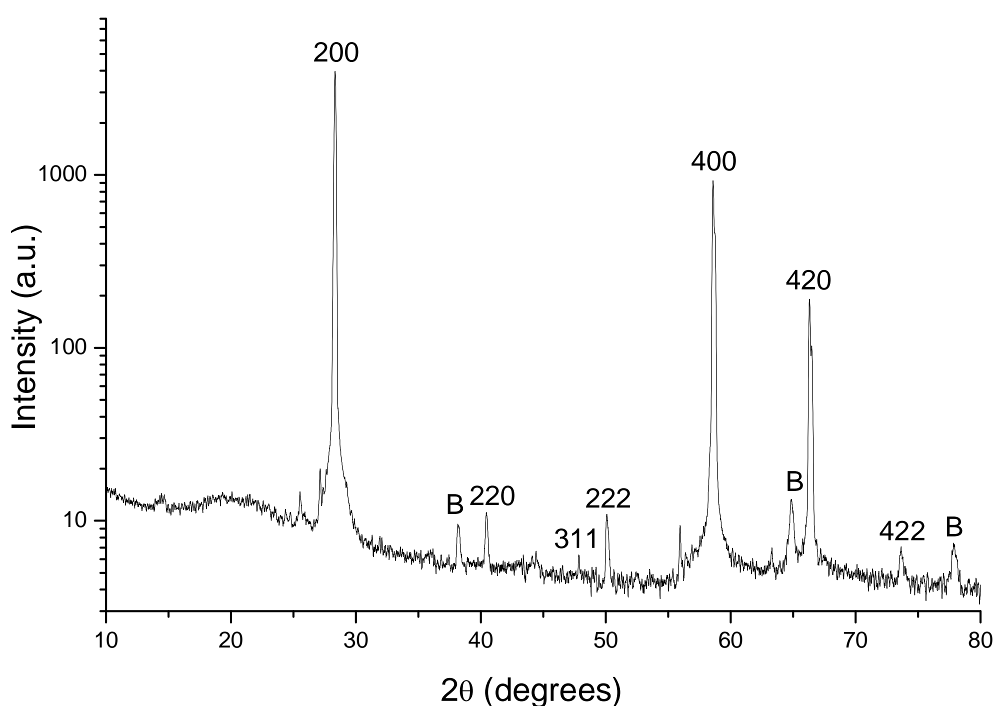

Figure 3.5 *2θ/θ XRD Diffraction pattern for the KCl pellets. The orientations of each of the peaks are marked and peaks ascribed to the base plate are labelled as B.*

thin films it is likely it will be indistinguishable from the CuCl (111) peak due to the accuracy of the instrument. Despite this being the peak of highest intensity, calculations of the KCl peaks show that the (400) peak has a texture factor of 5.221 greater than the (200) texture factor of 1.124. The crystallite size seems to vary, especially if we focus on the peaks of relatively large intensity ranging from 58 to 149 nm for the (200), (400) and (420) peaks. However the (400) and (420) $K_{\alpha2}$ peaks could be determined from the $K_{\alpha1}$ peaks meaning that the FWHM value was reduced and the calculated crystallite size increased. Therefore the actual (200) crystallite size is probably between 70 and 80 nm if we allow for the $K_{\alpha2}$ peak.

Plane (hkl)	ICDD 2θ (degrees)	KCl Pellet 2θ (degrees)	Diff (Exp – ICDD)	% Intensity ICDD	% Intensity Measured	Crystallite Size (nm)
200	28.346	28.334	-0.012	100	100	58.0
220	40.508	40.45	-0.058	37	0.301	46.0
222	50.170	50.05	-0.12	10	0.314	49.8
400	58.642	58.59	-0.052	5	24.210	112.0
420	66.383	66.307	-0.076	9	4.941	149.5
422	73.735	73.664	-0.071	5	0.202	92.5

Table 3.2 *Expected ratios of the KCl diffraction peaks visible in figure 3.5 and their actual values*

3.5 Protective Varnish Layer

Since the XRD scans are performed in an open atmosphere, to prevent very rapid deterioration of the CuCl structural properties the samples must be protected by a capping layer. A suitable capping layer must have certain qualities; be amorphous to prevent interference with XRD studies of the crystal structure in CuCl, have little to no effect on the structural properties of the material and protect the surface from moisture and oxidation. To test the suitability of clear varnish as a sealant it was applied to a series of different surfaces and diffraction analysis performed to confirm the varnish is not crystalline in nature. The addition of the varnish to the tape affixed to the base plate did produce any supplementary diffraction peaks. As figure 3.6 shows, there is little change in the addition of the varnish to distinguish the two, with a slight decrease

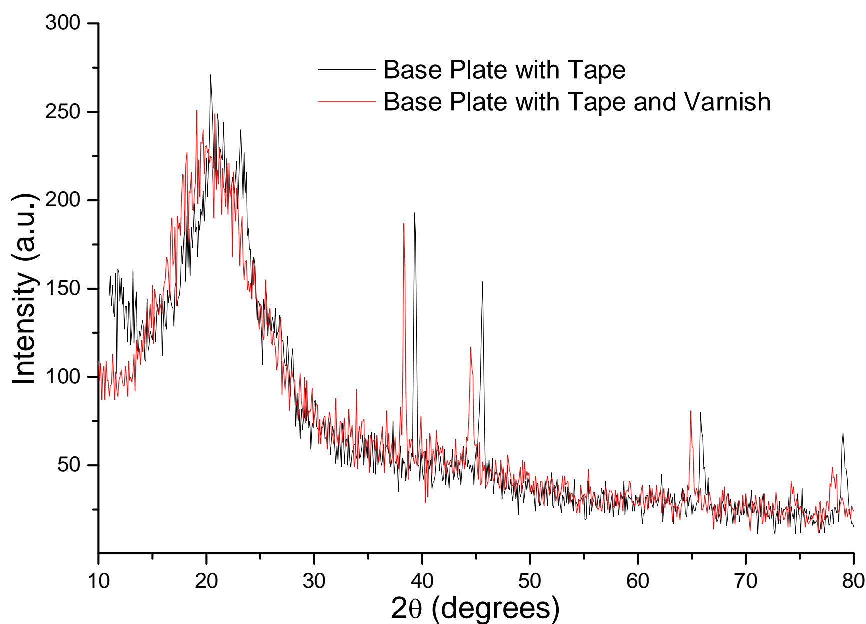

Figure 3.6 *Locked Coupled scans of the XRD machine's Base Plate with tape and with both tape and varnish. Scans were both recorded in increments of 0.1 degrees with 1 second at each. An offset of 1 degree has been applied to distinguish the peaks.*

in the intensity between 10˚ and 15˚ (but being outside the expected range of our CuCl and KCl peaks, this should not interfere with the diffraction analysis) and also in the intensities of the 44.6˚ and 78.1˚ peaks being the only alterations. This shows that the varnish does not have its own crystalline structure but is instead an amorphous surface which is one of the qualities a capping layer must possess.

To show how the clear varnish affects CuCl material it was applied to the CuCl pellets tested previously in section 3.3. Figure 3.7 shows the effect of the varnish on the 2θ/θ CuCl diffraction spectrum. The angular positions of the CuCl peaks are unaffected, but there is a slight decrease in their intensity. These two scans were performed on different setups to counter oxidising effects of the CuCl, with the varnish applied to the pellets as soon as they were affixed to the tape. This accounts for the increase in the broadband region around 20˚ as we have shown this to stem from the

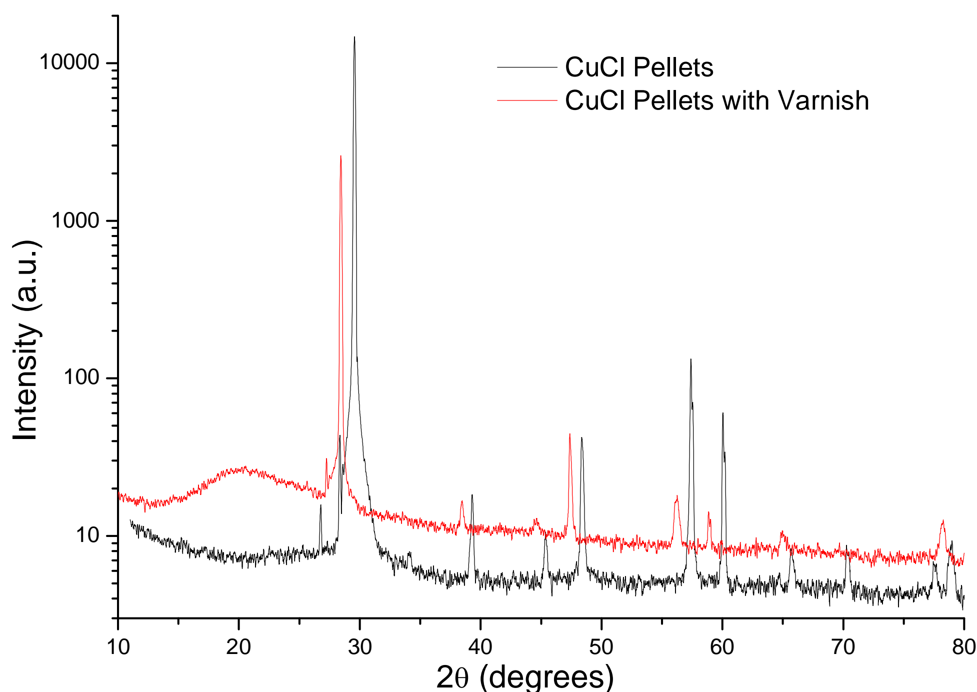

Figure 3.7 *2θ/θ XRD Diffraction pattern for the CuCl pellets with and without varnish. An offset of 1 degree has been applied to the diffraction patterns for clarity.*

tape rather than the samples themselves. Only the orientations of CuCl that showed a large signal to noise ratio were compared in table 3.3 to maximise the accuracy of our results. The overall difference in the intensities can be accounted for by the change in setup but the (311) peak at 56˚ shows a distinct change, deteriorating greatly from the unvarnished scan in both shape and intensity. This deterioration is quantified in table 3.3 by the crystallite size difference calculation which shows a decrease of almost 50% when compared with the values obtained in table 3.1.

Since the overall ratio of the peak intensities remains unchanged it is clear that the varnish does not have a large effect on the crystallinity of the CuCl material, but attention must be paid to the (311) peak to see if this deterioration is prevalent in all future scans. The final test of the influence of the clear varnish on the crystallinity of the materials, is to apply it to the thin film substrate (100) Si. Figure 3.8 shows the results for the (100) Si samples. Similar effects to the CuCl pellets were observed, the varnish causes a slight decrease in the intensity of the diffraction peaks and an overall increase in the background intensity. However the varnish has introduced a broadband region around 20˚ which we have previously observed to stem from the double-sided tape. It appears this is a feature common to both surfaces as no change to the setup

Plane (hkl)	**CuCl Pellet 2θ (˚)**	**Varnished CuCl Pellet 2θ (˚)**	**Difference (Varnished – CuCl)**	**FWHM CuCl (˚)**	**FWHM Varnished CuCl (˚)**	**Crystallite Size Diff (nm) (Var – CuCl)**
111	28.56571	28.43792	0.12779	0.14498	0.14404	0.33
220	47.39688	47.40955	-0.01276	0.25452	0.23342	4.18
311	56.42044	56.2242	0.19624	0.23858	0.44896	-28.37

Table 3.3 *Comparison of the diffraction peaks for CuCl prior to and after varnish application*

occurred between scans and is likely due to some degree of short range order with long periodicity in both systems. Whilst this affects the signal to noise ratio of the samples, it does not affect the angular position of the diffraction peaks. Therefore, when reading the FWHM of the diffraction peaks, the sides of the peaks could manually be extended to the background level prior to application of the varnish. This can be found by running the scan at the required settings on an unvarnished sample and recording the background level. These samples will then have significantly decayed, but since these levels were found to be consistent across multiple samples other samples need not be sacrificed in a similar fashion.

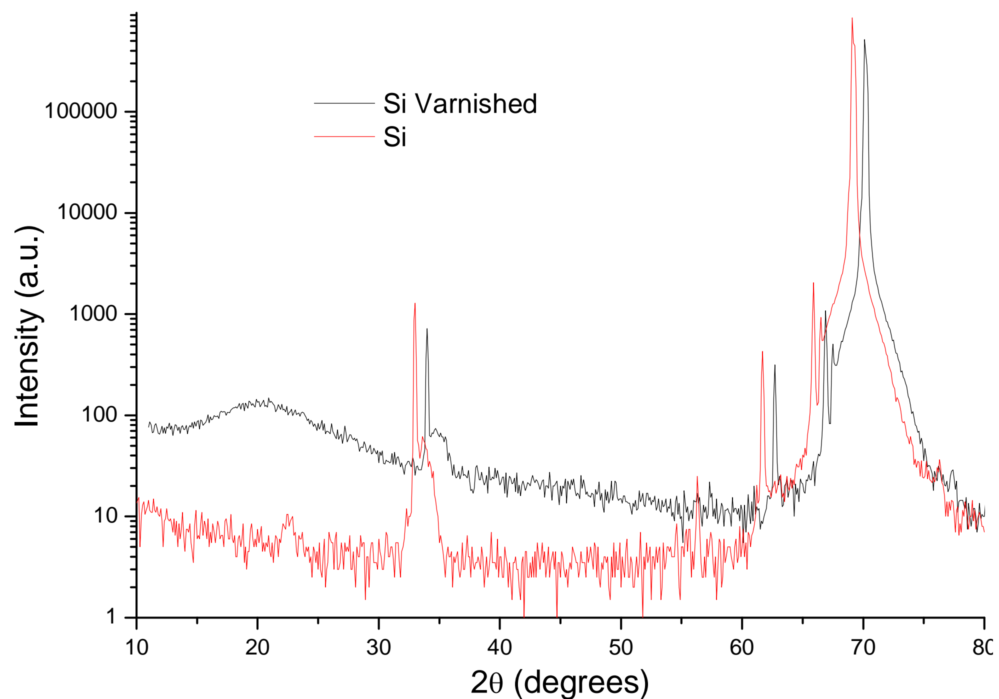

Figure 3.8 *θ/2θ scans of one Si sample. First untreated and then after the sample was coated with varnish. The spectrum of the varnished sample has been shifted to the right by one degree for clarity. The broad peak visible around 20˚ was sometimes found in both samples so is not specific to the varnish*

Once the capping layer was shown to have no significant effect on Si, further CuCl thin film samples were coated immediately upon completion of deposition when they were intended for XRD analysis. The resulting behaviour of the peaks was similar in effect to the pellet samples and can be seen in the next section. Application of the varnish layer did cause a slight shift in the rocking curve position for the (111) peak at 28˚ and a small decrease in intensity indicating that some kind of effect was taking place, or interference with the x-ray signal. However the optical and electrical methods of characterisation detailed in Chapters 4 and 5 require no barrier to be present between the CuCl thin film and atmosphere for reliable results to be obtained. Also in the process of oxygen doping our thin film samples, repeated doping of the same sample was found to yield more reliable results. This of course is not possible if there is a capping layer present, so this layer was used primarily for characterisation of the undoped 500 nm CuCl and KCl-CuCl thin film samples detailed in the following sections.

3.6 CuCl Thin Film Samples

To identify the crystalline nature and structural parameters of the deposited CuCl films the symmetrical reflections produced by $\theta/2\theta$ scans of the samples were studied. Several clearly defined Bragg peaks can be seen in figure 3.9 which show the polycrystalline nature of the films. The data is shown unprocessed to illustrate the differing diffraction positions of the Cu $K_{\alpha 1}$ and $K_{\alpha 2}$ peaks. The $K_{\alpha 1}$ and $K_{\alpha 2}$ peaks at 28˚ were too close to distinguish both visually and through processing so the values used are estimates. 2θ values of the diffraction peaks are in good agreement with the

accepted values of the International Centre for Diffraction Data (ICDD) powder diffraction database and are compared in table 3.4.

The first feature on the left of the scan is the large hump which has been shown to stem from the sellotape used to attach the substrate to the base plate of the XRD. This has a slightly crystalline structure with aligned long chain molecules, and can be ignored. Aside from the main (400) Si peak at 69º, the peak of highest intensity is at ~33º. These two peaks have been previously seen in our Si sample scans (figure 3.8) and the high intensity at these angular positions is due to the Si substrate rather than the CuCl layer.

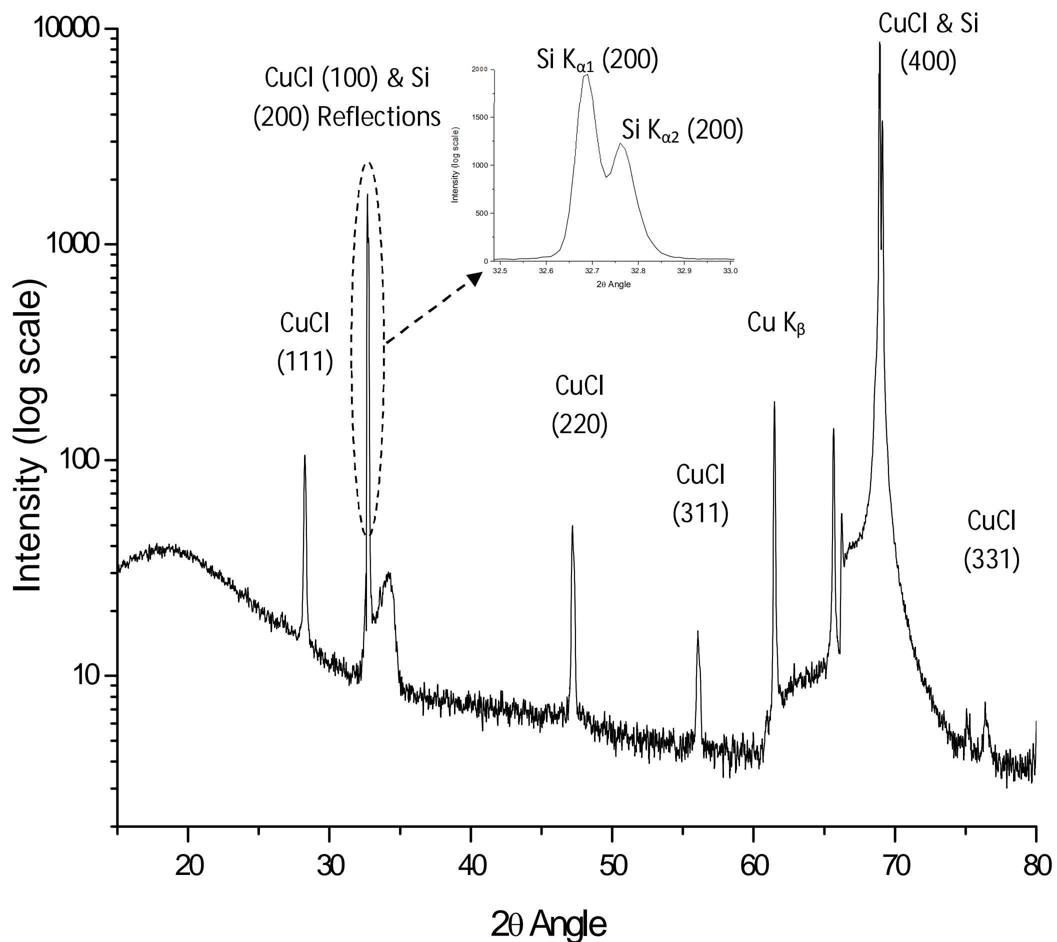

Figure 3.9 *2θ-θ scan for a varnished 500nm CuCl sample*

When the resolution of the peaks is increased two distinctive peaks can be seen. These are present for each of the diffraction peaks and can be attributed to the $K\alpha_1$ and $K\alpha_2$ reflections. Looking specifically at the enlarged (200) Si reflection in figure 3.9, we can see $K\alpha_1$ and $K\alpha_2$ peaks present at 32.687º and 32.766º. The (200) Si peak is normally forbidden due to the structure factors of the crystal, but as shown by this scan, multiple diffraction has occurred in the thick substrate from various planes of the single crystal resulting in the diffracted Si (200) beam shown [98]. It should be noted that the CuCl (200) peak cannot be distinguished from the Si (200) peaks. This peak would be quite small relative to the other diffraction peaks and since the position of this peak is extremely close to the $K\alpha_2$ (200) Si peak, the Si peak overshadows it entirely.

Diffraction Peak	$K\alpha_1$			$K\alpha_2$		
	XRD Experime-ntal Value	ICDD Value	$\Delta K\alpha_1$	XRD Experimen-tal Value	ICDD Value	$\Delta K\alpha_2$
CuCl (111)	28.268	28.545	0.277	28.309	28.594	0.285
Si (200)	32.687	Forbidden		32.766	Forbidden	
CuCl (220)	47.200	47.476	0.276	47.298	47.561	0.263
CuCl (311)	56.065	56.338	0.273	56.182	56.441	0.259
Si (400)	68.912	69.132	0.220	69.112	69.327	0.215
CuCl (331)	76.393	76.590	0.197	76.674	N/A	N/A

Table 3.4 *Comparison between the experimental and accepted diffraction peak values for both the $K\alpha_1$ and $K\alpha_2$ x-ray values taken from figure 3.9. All values are 2θ degrees. The CuCl (331) $K\alpha_2$ value was absent from the system's ICDD database*

The same effect occurs at the Si (400) peak which is of much higher intensity. It has been shown previously on Si (111) that CuCl growth matching the orientation of the substrate results in a broadening of the rocking curve at this diffraction angle rather than having any noticeable effect on the peaks themselves in the 2θ-ω scans [99]. This is due to the polycrystalline growth of the CuCl in this orientation indicating a slight misalignment with the Si. This is not the case with Si (100) although it could be due to the lower intensities of these diffraction peaks (as indicated by the ICDD values and our scans of the powder material) not being significant enough to be detected rather than a lack of growth in the substrate's orientation.

Upon performing φ-scans on the Si (100) peak, it was found to be heavily dependent on the φ angle used. A series of sharp diffraction peaks in four-fold rotational symmetry are found as shown in figure 3.10 (a). Each of these peaks are numbered, with 1A, 1B, 1C and 1D being symmetrical peaks and the same rule applies for 2, 3 and 4. Figure 3.10 (b) shows an enlarged 90˚ section showing the identification of each of the multiple diffraction peaks confirmed to stem from the Si substrate. There is no evidence of any extra diffraction peaks, or unexplained variations in intensity that could signify the presence of CuCl. This pattern repeats every 90˚ and very closely matches the previous results for the φ pattern of (100) Si at 33˚ from which the peaks are identified [98].

At 28.268° we see the CuCl (111) peak. This is the largest intensity of the solely CuCl peaks and agrees with previous studies which have shown (111) CuCl to be the preferred orientation of CuCl growth on amorphous glass substrates and Si substrates of various orientation [47, 100-102]. At 47.177° the CuCl (220) is shown as

the (220) Si peak is forbidden and the (311) CuCl peak is visible at 57.065 for the $K\alpha_1$ and at 57.182 for the $K\alpha_2$. Each peak was shown to stem from CuCl in our

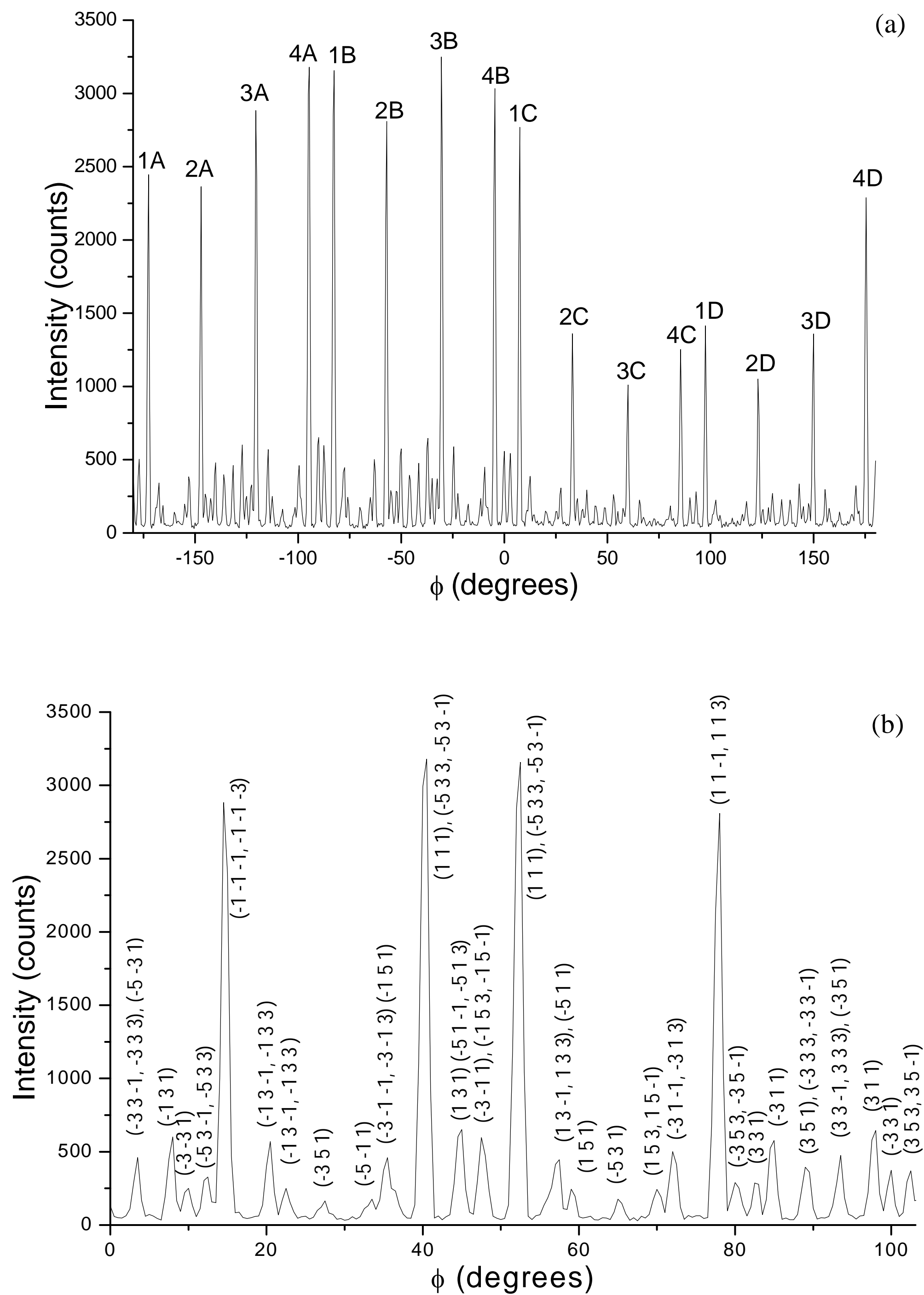

Figure 3.10 *(a) φ-scan of a 500nm CuCl sample on Si (100) with the 2θ angle set to 33˚. The numbers are constant for each position of symmetry, i.e. 1A, 1B, 1C and 1D are symmetrical. (b) φ-scan of the same sample truncated to show the section of symmetry*

composition scans as there were no peaks visible at these orientations for the Si wafer scans. The $K\alpha_1$ and $K\alpha_2$ values at each of these orientations are almost indistinguishable from each other except for the slight shoulder on the right-side of the peak corresponding to the slightly weaker $K\alpha_2$ peak. This is enough for the peak positions to be obtained through data processing.

The variation from the expected intensity of these peaks according to the ICDD values is quite dependent on the quality of the deposition and the level of decay of the samples. With this in mind the closest matching ratios obtained were for a different sample to that shown in figure 3.9. The percentage intensities relative to the (111) peak of the (220) and (311) orientations are 60% and 27% which is an acceptable variation from the ICDD values of 55% and 30% respectively. Multiple samples showed that whilst there was some variation in the ratios obtained, they were all much closer to the ICDD values than those obtained from the CuCl pellet scans. This could be due to the material relaxing to its natural orientation as the distance from the Si surface is increased and with no inherent restriction on the material due to the manufacturing process.

The presence of a number of clear CuCl XRD peaks discussed indicates that the CuCl film is not epitaxially grown on the substrate, however the samples do show a degree of preferential alignment or texture [72]. It would appear from the scans that preferential growth of CuCl occurs in the (111) direction on the (100) Si substrate due to the level of intensity of this peak and that it stems solely from the CuCl deposited. Whilst clearly the (200) peak is of greater intensity, the contribution of CuCl to this peak is relatively minor as discussed previously. The degree of alignment or texture is best illustrated by the texture factor and for the CuCl thin film sample illustrated in Fig 3.9 the texture factor of the (111) peak is ~1.6. Across multiple CuCl samples this was

typically in the region of ~1.35 – 1.65 which is notably far less than the CuCl pellets, but still shows a bias towards the (111) peak.

The crystallite size of the (111) peak obtained from the FWHM value is found to be 55.3 nm. Across multiple samples the size was found to vary between 50 – 55 nm with the samples with larger texture factors having a smaller crystallite size in the (111) plane.

The (111) peak is shown more clearly in the following section on glancing angles as the x-ray does not penetrate deeply into the thin film and the Si (200) peak intensity is removed by the nature of the technique. When characterising the CuCl samples it is important to distinguish between the peaks reflected from the substrate and those reflected from CuCl. As the lattices are very closely matched, there is only a small difference in the angle of the diffracted peaks. There is a more significant difference in their intensity, with the peaks stemming from the silicon substrate being much larger and masking the CuCl signal.

3.7 Glancing Angle X-Ray Diffraction

The X-ray diffraction pattern of thin films deposited onto a substrate can be dominated by the substrate itself. To minimise the contribution from the Si substrate and focus on the surface layer of the CuCl thin film samples glancing angle x-ray diffraction was used. This method was described previously in section 2.3.

Several different glancing angles were tested and are shown in figure 3.11. At angles up to 10° shown in particular by scans (b) – (e) from figure 3.11, the signal to noise ratio is such that the CuCl peaks can be clearly discerned from the background signal. However at angles greater than 10°, the influence of the CuCl surface begins to

wane, the peak intensity dips and the influence of the underlying Si material masks the CuCl signal, as seen in (f) from figure 3.11. Similarly as the glancing angle approaches 4˚, through scans (a) – (c) from figure 3.11, the intensity of the CuCl peaks increases and attains maximum intensity. From the region of maximum intensity between 4˚ and 10˚ degrees, 5˚ was chosen as the glancing angle for all subsequent scans.

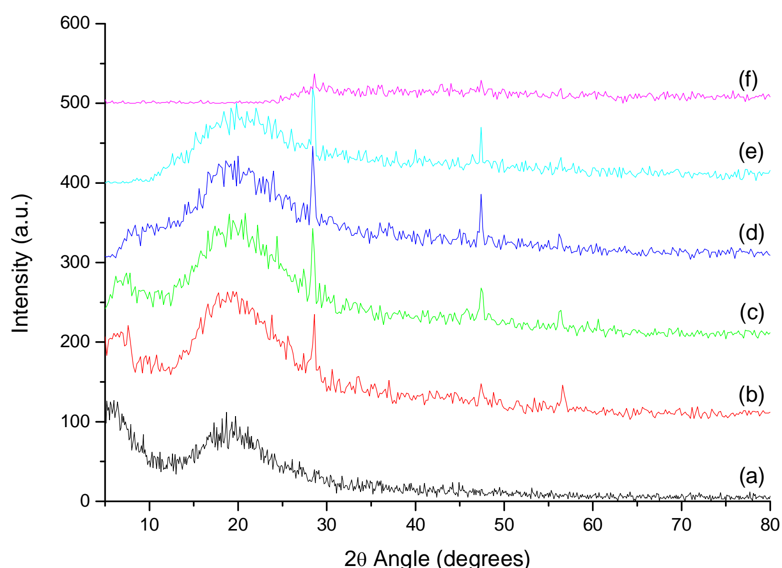

Figure 3.11 *Glancing Angle scans of CuCl recorded at (a) 0.5˚, (b) 2.7˚, (c) 4˚, (d) 6˚, (e) 10˚ and (f) 24˚. Each of these is offset by 100 counts for clarity and all scans were recorded from the same sample and setup*

To further understand the penetration depth within our samples of this glancing angle, figure 3.12 shows the attenuation length of the x-rays within CuCl and Si as the glancing angle is increased. Using this graph we can see our 5˚ glancing angle has an attenuation length of ~ 3 μm through CuCl. Since our CuCl layer is 500nm thick, the remainder of the x-ray intensity will pass through the Si layer.

Using an exponential scale the x-rays will have lost 60% of their intensity in the CuCl layer when they reach the Si and all diffraction peaks will have to emerge once again through the surface further decreasing the Si signal. Due to these factors the

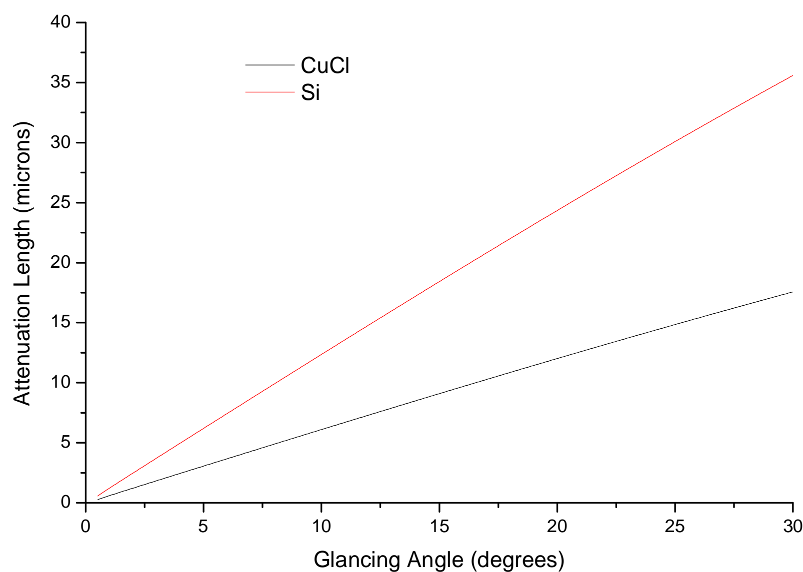

Figure 3.12 *Glancing Angle of the X-ray diffraction plotted against the Attenuation length of the X-ray within both CuCl and Si*

diffraction at a glancing angle should stem mainly from the CuCl thin film layer, with little to no contribution from the Si layer underneath.

In practice this proves to be the case. The scan shown in figure 3.13 was recorded at a glancing angle of 5° and shows that the technique has eliminated any reflection from the silicon substrate itself as there are no Si peaks visible, just CuCl. There is still however some influence of the base plate and tape as shown by the region between 10˚ and 20˚. The shallow angle used and the spread of the beam itself makes it difficult to remove the influence of these signals from the glancing angle scans so it is important to note their source. The three CuCl peaks prominent in the θ/2θ scans can also be clearly seen in the glancing angle scan, the (111), (220) and (311) peaks. The (331) and (100) peaks were also seen in some scans but not consistently and always at a low intensity. For the (331) peak this intensity is similar to the θ/2θ scans but for the (100) peak it shows how small the contribution of CuCl growth is at this orientation.

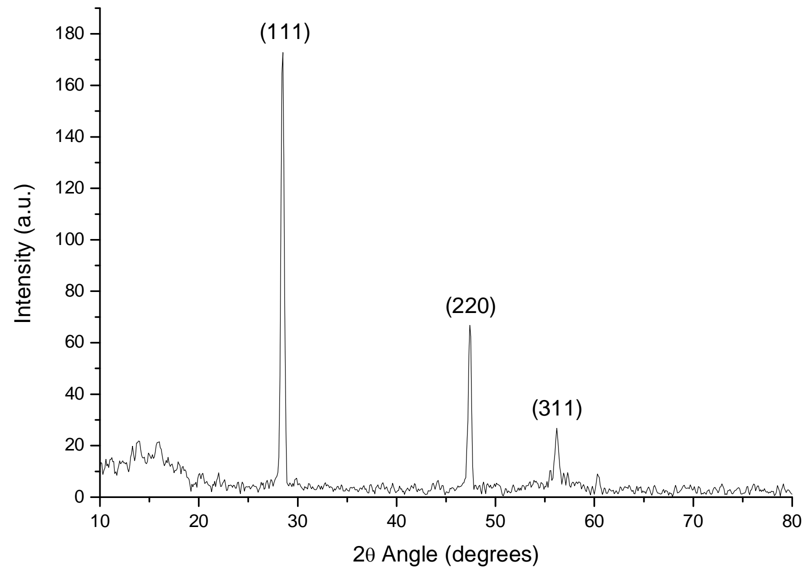

Figure 3.13 *Glancing Angle scan of a CuCl thin film sample performed at a glancing angle of 5˚*

The glancing angle setup will only allow diffraction peaks from polycrystalline grains within the material to be detected. Due to the range of different peaks present at orientations different to that of the Si substrate beneath, it is clear that CuCl exhibits polycrystalline growth as the distance from the Si substrate is increased. The texture factor of the (111) peak shows a significant increase at the glancing angle orientation when compared to the $\theta/2\theta$ setup, changing from ~1.6 to ~2.1 for most CuCl samples tested. Whilst this value varied across different batches of samples, the increase was always ~0.4. Since the pellet scans of CuCl showed a texture factor of 5.7 for the (111) peak it's clear that the polycrystalline growth of CuCl is more relaxed towards the orientations present in the pellet form prior to deposition. The FWHM of the glancing angle scans is broadened by the nature of the technique, leading to a much smaller value of the crystallite size to be estimated. However, changes in this value can be measured and will be used in the section on oxygen doping to show how the doping

effects the polycrystalline formations within the CuCl and KCl-CuCl thin film samples.

3.8 CuCl - KCl Samples

During the CuCl/KCl deposition, it is thought that a K-Cu-Cl liquid mix is being formed during the melting of the CuCl/KCl growth mixture due to the concentrations of CuCl and KCl. In turn the deposited film, if it follows the source material stoichoimetry, should form a phase-separated mixture of CuCl and K_2CuCl_3 as it cools according to the phase diagram shown in figure 3.4. Thus we expect the deposited film to be a 500 nm film of CuCl containing K_2CuCl_3 crystallites and CuCl crystallites in the molar ratio 1:7 K_2CuCl_3:CuCl to match the stoichiometry of the original mixture (2:8 ; KCl:CuCl). The K_2CuCl_3 crystallites are expected to be (a) very small ~62.5nm and (b) to constitute a small fraction of the overall material. The ICDD pattern for K_2CuCl_3 shows 197 reflections beginning at $2\theta = 10.191°$ and occurring at irregular intervals after this up to $2\theta = 80.809°$. Given the fact that the K_2CuCl_3 crystallites are expected to be very small one would expect a Debye-Scherrer broadening and the overlap of these broadened, closely spaced, low intensity peaks should have a negligible effect, with maybe a slight influence on the overall background signal.

We can see when examined using the $\theta/2\theta$ scan as seen in figure 3.14, the KCl-CuCl sample discussed in section 2.2.3 doesn't appear to be much different from the CuCl, maintaining a slightly higher background signal but possessing similar peaks throughout. Both scans show the CuCl (111), (200), (220) and (311) peaks become more pronounced as the resolution of the scan is increased. The cause of the cluster of

peaks around 56˚ is not confirmed, but can be seen sporadically in both the CuCl and KCl-CuCl samples. One theory is that it stems from the wurtzite phase of CuCl formed between 681 and 703 K [67]. As production and testing continued these peaks became more pronounced with time. The only change to the deposition process was a slower rate of temperature increase to counter a bubbling effect as the CuCl liquidised with the KCl. To keep results for both types of sample consistent, this slower rate was also used for unaltered CuCl samples. These peaks are not present at glancing angles indicating they stem from beneath the surface possibly coming from a formation of the wurtzite CuCl at the Si substrate interface.

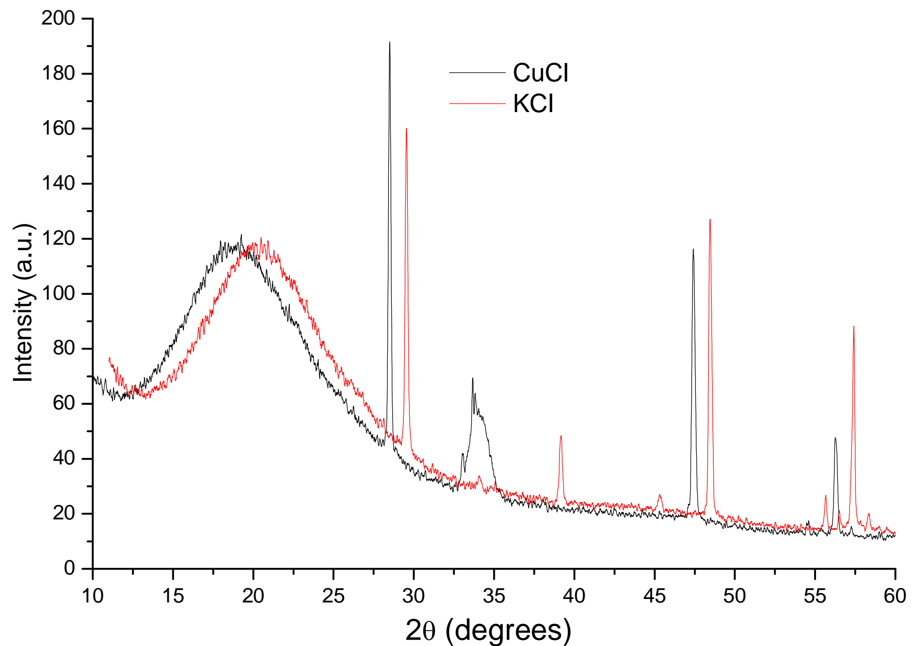

Figure 3.14 *2θ-ω scans comparing a 500 nm CuCl to a 500 nm KCl-CuCl sample*

The two other peaks unaccounted for in the KCl sample at 38.3˚ and 44.6˚ have been previously shown to stem from the base plate in section 3.2. However, previous studies on CuCl have shown that the orthorhombic η-Cu_3Si compound observed as the result of the reaction between CuCl and Si at temperatures greater than

250˚C is also present at 44.6˚ [49]. Peaks of Cu are enhanced by the formation of this compound and can also be found at 38.3˚ [103]. As was the case with the peaks around 6˚, they are not present at glancing angles indicating they stem from the Si substrate interface or the base plate beneath.

Scans performed using the glancing angle on the KCl-CuCl samples setup show little variation from the scans of CuCl as shown in figure 3.15. The main peaks present are the CuCl (111), (220) and (311) peaks with little change to the background level or relative peak intensity. At higher resolutions the CuCl (331) peak at 76˚ can also be seen but at very low intensity as was the case with the CuCl samples.

The texture factor of the KCl-CuCl peaks is also similar to the pure CuCl samples ranging from ~1.6 to ~1.8 with a similar increase at glancing angles up to ~2.1 due to the low intensity of the (331) peak at 76˚ in the glancing angle scans. Crystallite size of the (111) CuCl peak is also comparable to the regular CuCl samples, measuring an average of 50 nm.

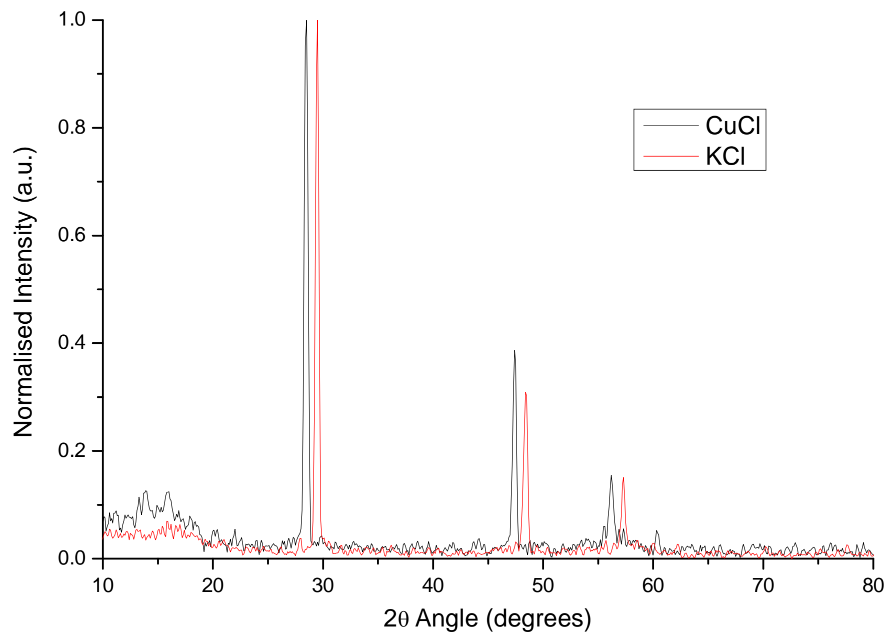

Figure 3.15 *Glancing Angle Scans of 500 nm samples of CuCl and KCl-CuCl normalised to the highest peak at 28˚*

3.9 Decayed samples of CuCl and KCl

Deterioration of the structural properties of the CuCl and KCl-CuCl thin film samples occurs due to interactions with moisture and oxygen naturally present in air. This causes hydrated oxyhalides of Cu^{++} to be formed mainly consisting of numerous different isomers in the atacamite group of minerals which have the common chemical formula of $Cu_2(OH)_3Cl$. These isomers have several diffraction peaks in common leading to amplification of these peaks, in particular the peak at 16˚ visible in both the KCl and CuCl samples in figure 3.16. This peak is an indication of the level of oxidation of the samples. Several more peaks are present at 33˚, but as with the fresh CuCl samples this is masked by the Si substrate underneath. There is also a visible difference in the decayed samples tested, with a greenish hue on the surface and a more visible powder-like structure on the surface rather that the smooth rainbow-like

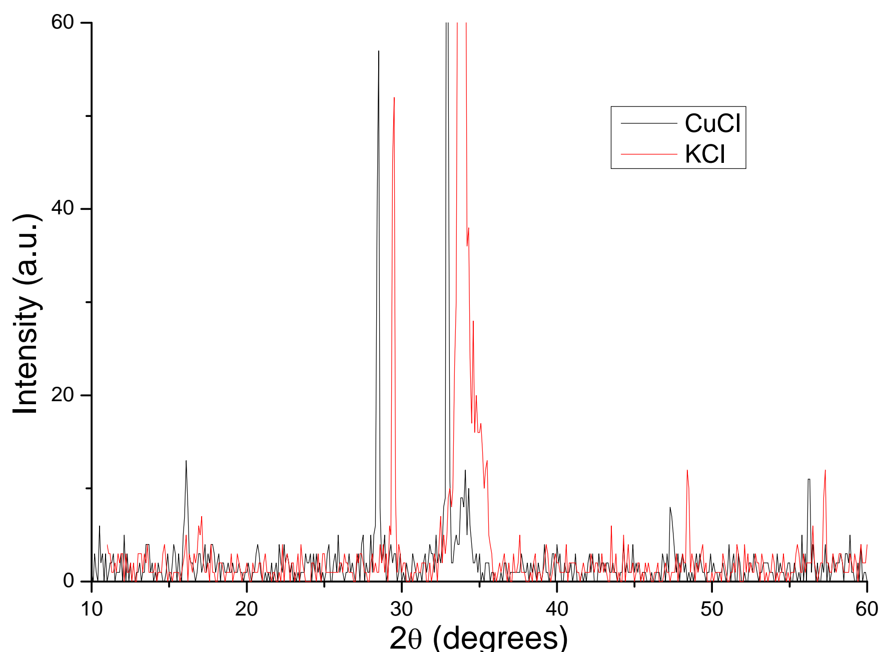

Figure 3.16 *2θ/θ scans of 500nm samples of CuCl and KCl-CuCl focussing on the area of the main CuCl peaks. Scans are offset by 1˚ for clarity.*

effect seen in freshly deposited thin films.

More detailed scans of the oxidation peak and CuCl peaks at 28˚, 47˚ and 56˚ confirm that there is a large decrease in the intensities of the CuCl peaks compared to the fresh samples, a decrease of between 65-85% for each peak. If we look at the relative intensities of the peaks there is a decrease for the 47˚ of ~14% with the other peaks reducing in tandem with the 28˚ peak. The crystallite sizes are slightly increased by around 10-15% probably due to the incorporation of the new elements and their bonding within the thin film. Texture factor values are slightly at the lower end of the scale, but well within values recorded for numerous fresh CuCl and KCl-CuCl samples, being between 1.1 and 1.6 with an increase to between 1.9 and 2.1 at glancing angles. The oxidation peak at 16˚ has a crystallite size of between ~36 and 39 nm across both CuCl and KCl-CuCl samples. The importance of these tests is to distinguish the change in features due to interaction with both oxygen and moisture and from the introduction of pure oxygen in the doping tests detailed in the following section.

3.10 Oxygen Doping of CuCl

To understand the effect of oxygen plasma treatments on the range of CuCl thin film samples, XRD measurements were taken before and after plasma treatments for all samples. The samples were treated for up to 900 seconds to chart the effect on the structural properties. The difference in the XRD proved to be extremely slight, having little to no effect on the intensities for up to 300 seconds of doping and a

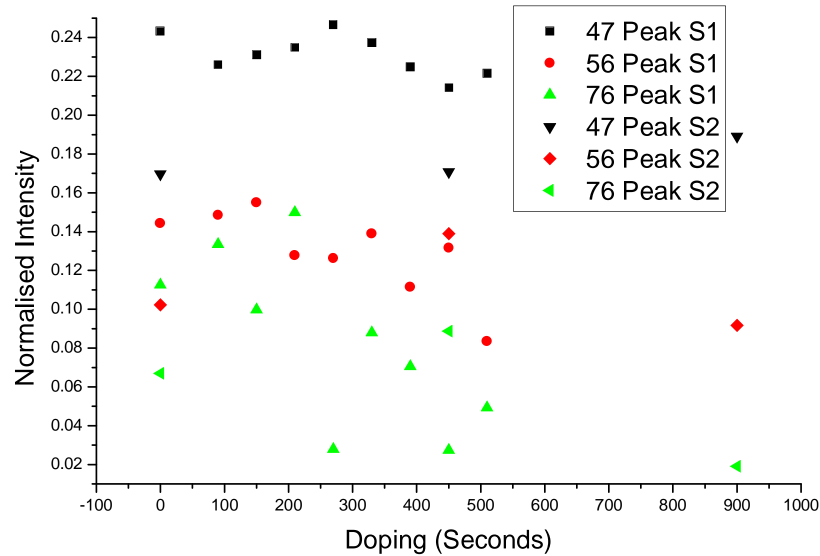

Figure 3.17 *2θ-θ intensities of the peaks present at 47˚, 56˚ and 76˚ normalised to the 28˚ peak intensity. These were recorded on two different CuCl samples, one at 60 second doping intervals after an initial 90 second dope, the other after 0, 450 and 900 seconds of doping.*

gradual decline in the intensity of the majority of the peaks after this point.

Figure 3.17 shows this slight decline in the relative peak intensities of the various CuCl orientations. The (111) peak at 28˚ was used to normalise the other peaks as it remained the peak of maximum intensity throughout with signal deterioration notable only after 900 seconds of doping. The (220) peak at 47˚ peak remains at a relatively constant level throughout the entire process but the (311) peak at 56˚ and the (331) peak at 76˚ show a significant decline. This is distinct from the decayed samples measured in the previous section which showed a significant deterioration in the (220) 47˚ peak indicating that this decay was caused by the presence of both oxygen and moisture. The peak intensities remain constant at glancing angles indicating that the detrimental structural effect of the plasma treatment is most prevalent on the CuCl forming ordered growth in alignment with the Si substrate. The KCl samples however,

showed a relative decline for all of the peaks compared to the (111) peak at 28° which increased in intensity at doping levels of up to 300 seconds and decreased after this point. The relative glancing angle intensities remained constant for the KCl doped samples as well.

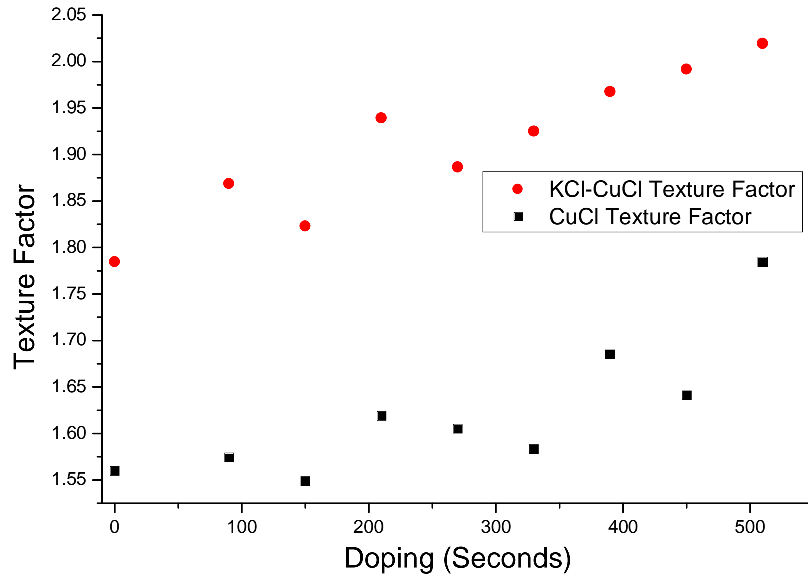

Figure 3.18 *Texture factors of the (111) peaks for CuCl and KCl samples doped for 90 seconds and then 60 second intervals up to 510 seconds.*

The deterioration of the peaks of orientations other than the (111) peak is best illustrated by the changes in the calculated texture factor. As we can see from figure 3.18, there is a linear relationship between the texture factor and the length of the doping process. This was found to be common across multiple samples with the initial texture factor value being the only variance. This shows that the other peaks are deteriorating at a faster rate than the (111) peak. The stability of the (220) peak at 47° is further shown by the crystallite size calculations shown in figure 3.19. We can see that for both the CuCl and KCl samples the (311) peak at 56° shows a significant decrease in crystallite size as doping is increased. This peak possessed the lowest

intensity of all the diffraction peaks recorded and the highest initial crystallite size. So rather than indicating an isolated crystallite size reduction, the universal effect of the doping process is more pronounced at this diffraction peak.

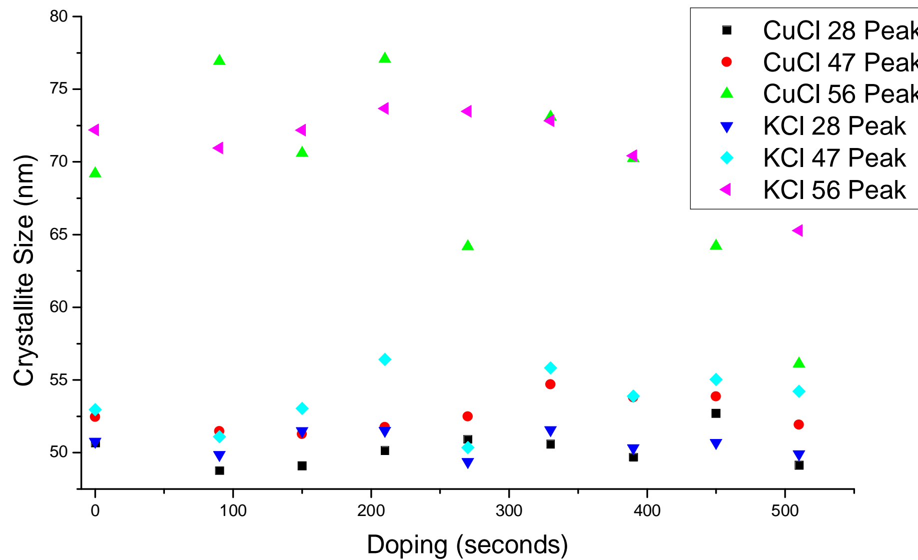

Figure 3.19 *Calculated crystallite sizes of the diffraction peaks at 28˚, 47˚ and 56˚ for CuCl and KCl samples doped for 90 seconds and then 60 second intervals up to 510 seconds.*

3.11 Summary

The X-ray diffraction studies performed in this chapter show that preferential growth for the undoped CuCl samples occurs in the (111) direction, with diffraction peaks at (220) and (311) orientations clearly distinguishable as well demonstrating the zincblende lattice structure of CuCl. The presence of the (100) CuCl peak was investigated with the φ scan at the (100) position of pure Si and our thin film samples compared. No trace of separate (100) CuCl diffraction was found. The glancing angle scans differentiate between the polycrystalline CuCl diffraction peaks and those

aligned with the (100) Si substrate. These showed the polycrystalline nature of the CuCl thin films on the Si substrates and once again a distinct lack of the (100) CuCl peak. There is still the possibility of perfect lattice-matching with the Si substrate material, but it seems extremely unlikely seeing as the CuCl (100) peaks are unable to be distinguished in either of the XRD scan methods used.

The influence of the KCl salt on the structural properties proved to be indistinguishable from the CuCl samples themselves. Oxygen doping of the samples produced a decrease in the measured crystallite size determined from each of the diffraction peaks and an increase in the texture factor of the CuCl (100) peak for both CuCl and KCl-CuCl samples. There was an overall decrease in the peak intensity of each of the measured diffraction peaks as doping was increased indicating a deterioration of the structural properties of the material. This seems to indicate a reduction in the quantity of CuCl material present after oxygen doping has taken place.

Due to the dominance of the (100) CuCl peak throughout the XRD analysis, any prominent features discussed in the following chapters are likely to stem from CuCl material at this orientation. This will be especially true for highly doped material due to the increasing texture factor seen.

Chapter 4

CL and EDX Imaging in the SEM

4.1 Introduction

This section reports on the analysis of photons and x-rays from our thin film material when an electron beam is focused on the surface of the samples in the SEM system. We begin by detailing the CL results for the undoped CuCl thin films and discussing the distinctive features of these spectra. These consist of the FWHM and relative intensity ratios of the peaks detected, and their variance as the probe current is increased. Low-resolution digital CL images combined with images from the SEM in secondary electron mode are used to illustrate changes in CL beneath the surface of the sample topographically.

With the CuCl undoped sample properties and expected values established, the KCl-CuCl sample properties were investigated in a similar manner before moving on to our oxygen-doped samples of both CuCl and KCl-CuCl. The alterations in the characteristic properties of the CuCl and KCl-CuCl thin films as the doping is increased are described in this section, showing their fluctuations and establishing an ideal doping level to maximise both the luminescence properties and the conductivity of the samples.

EDX scans were used to complement the results obtained from the CL scans. These ascertained the atomic percentages of both our undoped samples before plotting

their variation as the levels of doping are increased. This allows us to attribute notable changes in the CL spectra to any corresponding factors at the atomic level within the material.

Finally SEM images recorded in secondary electron mode are used to show the effect of the doping process on the surface of the samples themselves. This allows us to see structurally how the effects responsible for the changes detected in the CL and EDX scans may also manifest themselves in the surface topography of the samples. A short discussion on the how the properties of atmospherically decayed samples of CuCl and KCl-CuCl compare to our oxygen doped samples concludes the chapter.

4.2 Cathodoluminescence Results

Studies on nominally undoped CuCl thin films using the CL technique (at room temperatures) provided useful information, with a clearly defined peak around 385 nm or 3.224 eV (which closely matches the Z_3 exciton of 3.204 eV [104] once the shift to room temperature is taken into account) and a large broad band of blue-green emission centred at 520 nm due to defects within the material [105] as shown in figure 4.1. For this scan a probe current of 500 pA was used combined with a magnification of 1000× and a beam energy of 15 keV. These settings ensure results will stem from a relatively large area on the surface but sample damage due to high current density should also be minimal. This spectrum also shows the 2nd order of the 385 nm peak around ~772 nm due to the diffraction grating. The range of the scans was set to between 350 and 700 nm to remove this peak from all future spectra.

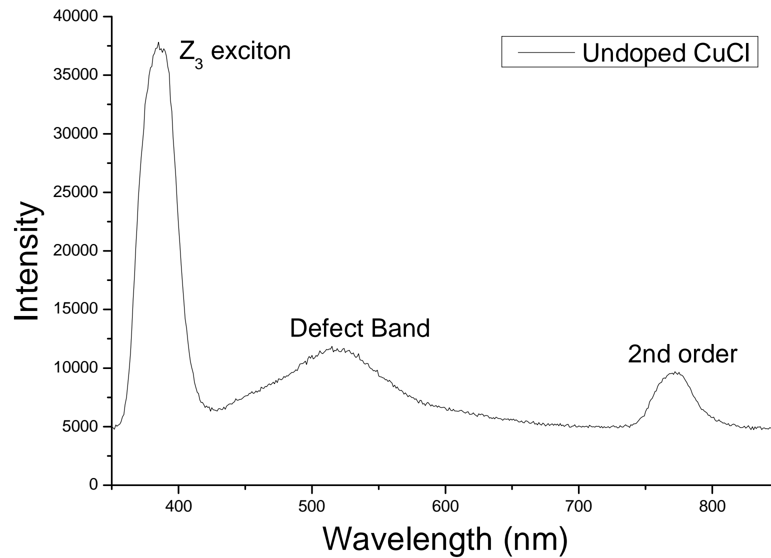

Figure 4.1 *CL spectrum for an undoped CuCl 500nm sample*

A consistency test was performed using this technique to verify the reliability of the results and the deposition itself. Several batches of samples were made using the same powder and under the same conditions. CL scans were then performed on the samples using 15keV for the electron beam and a probe current of 500 pA. Each sample was tested in turn with the remaining samples from each batch held in an evacuated desiccation jar which was continuously pumped down to maintain the vacuum within. This ensured minimal decomposition of the samples due to natural air. A fresh batch of samples was produced upon the completion of testing of the previous batch. Since the thickness of the deposition layer varies depending on its position from the centre-point of evaporation, readings were taken from different positions on each sample tested, at opposite ends of the samples themselves.

From figure 4.2 we can see that a small discrepancy between the peak intensities of the 385 nm and 520 nm peaks is present. When the scans are normalised to the position of maximum intensity of the 385 nm peak (figure 4.3) the difference

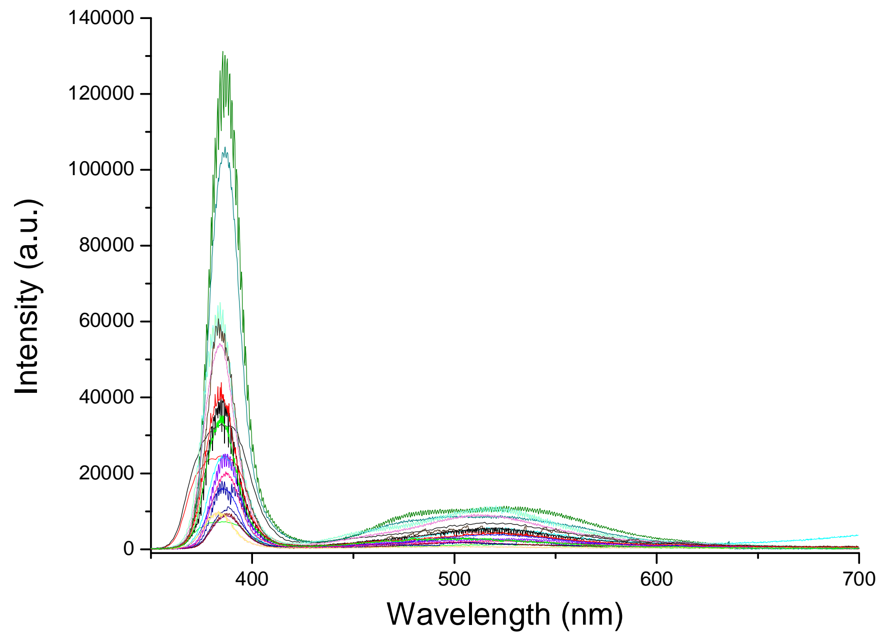

Figure 4.2 *Full spectra recorded for a selection of undoped 500 nm thickness CuCl samples. Background signal has been subtracted.*

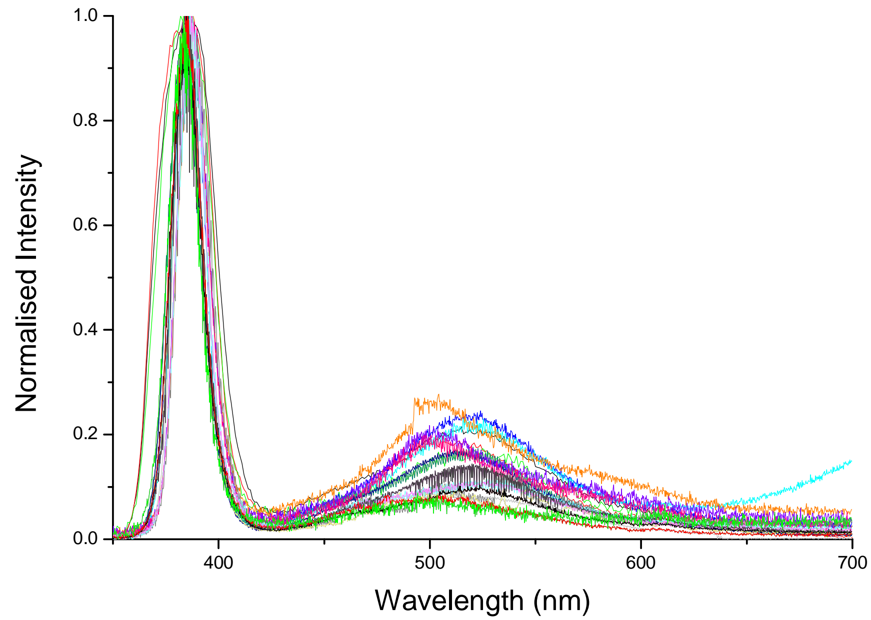

Figure 4.3 *Normalised (with respect to peak at ~ 385 nm) spectra recorded for a selection of undoped 500 nm thickness CuCl samples. Background signal has been subtracted.*

between the peak positions in various samples is still evident but also quite small. The shape of the 520 nm band is similar for all of the samples with some variation of up to 10 nm in the central peak location due to the slight variance in defect content within the different sample. This could be due to thin film interference effects and slight differences in the sample thickness, as previously observed in samples of ZnO with the effect becoming more pronounced as thin film thickness is increased [106]. The same variance is not present in the Z_3 peak at 385 nm, varying by as little as 2 nm throughout. This is mainly because unlike the defect region, the Z_3 exciton location is a physical property of the CuCl material itself and thus should display minimal variance.

If we examine the area under the curve for the 385 nm and 520 nm peaks the relationship can consistently be approximated to 2:1. This relationship remains somewhat constant throughout multiple samples. However if we determine there to be a number of different peaks superposed as appears to be the case, the area under the curve becomes less reliable without separating out each of these peaks. This indicates that the peaks present in this region are not gaussian in nature and for this reason the peak intensity value was used instead of the area beneath the curve. The increasing intensity recorded at 700 nm for the turquoise scan is due to the system overheating, an inherent problem with the SEM CL attachment itself and present in numerous other samples not shown here. The values recorded prior to this position were the expected readings for the regions under inspection and once the system is allowed to cool, values become within expected bounds once more.

Another way to examine the repeatability of the scans is by measuring the full width at half maximum (FWHM) of the 385 nm peak. For each of the samples a Gaussian fitting profile was used, which fit the data well and the FWHM was extracted from the output of the fit. The resultant graph is shown in figure 4.4 alongside one of

the Gaussian fits to show the accuracy. As we can see from this, the FWHM fluctuates only slightly, varying in width between 15.4 nm and 17.9 nm. The resolution of the Gatan MonoCL monochromator is approximately 1 nm and is shown by the error bars on the graph. This suggests that the 385 nm peak width does not depend on the deposition run. In fact it was found to depend heavily upon the micrometer setting of the equipment itself. This setting controls the slit width for light incident on the internal CL mirroring equipment and detector. For the doped samples and some undoped samples upon increasing this setting from 5 mm up to 10 mm a corresponding increase of approximately 10 nm in the FWHM was recorded.

Deep level defect emission at photon energies below the band edge region is a useful tool for judging material quality. An example of such emission is the 520 nm band in CuCl as seen in figure 4.1. A comparison of the ratio of the 520 nm band to the

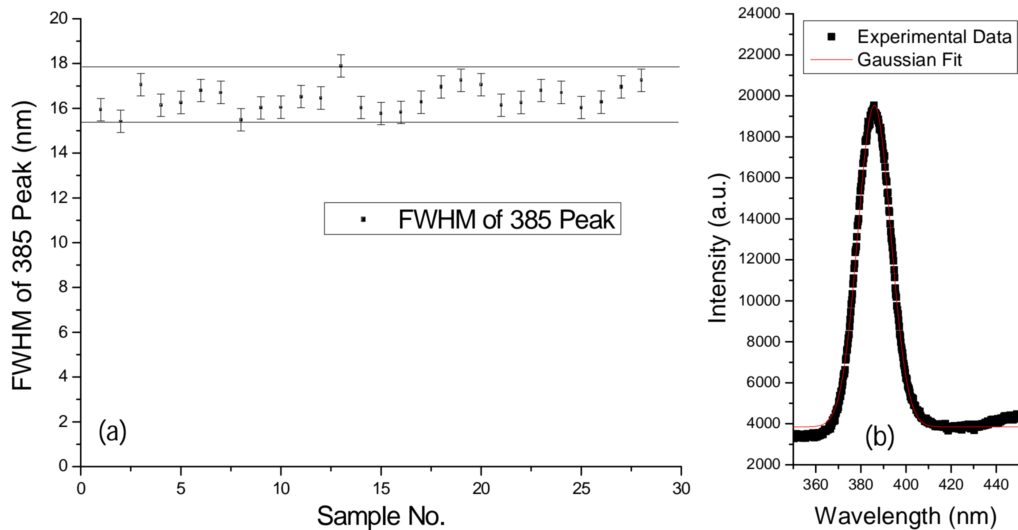

Figure 4.4 *(a) Variance in the full width at half maximum values derived from a Gaussian fit recorded for each of the undoped CuCl 500 nm thickness samples (b) said Gaussian fit of one of the CuCl peaks*

385 nm band is shown in figure 4.5. Although there is a variance of 0.2, the ratio is consistently between 0.075 and 0.275 for each of the undoped samples. In combination with the data in figures 4.2, 4.3 and 4.4, this indicates that the deposition process for undoped material is reproducible in terms of the room temperature optical properties measured by CL. This allows us to accept these values as typical of the undoped properties of the material and any alterations to these values when measured on doped samples will be due to the effect of the added material. These values were also the lowest measured across all the different sample types suggesting that the both the oxygen doping and KCl mixture increases the presence of defects within the CuCl thin films.

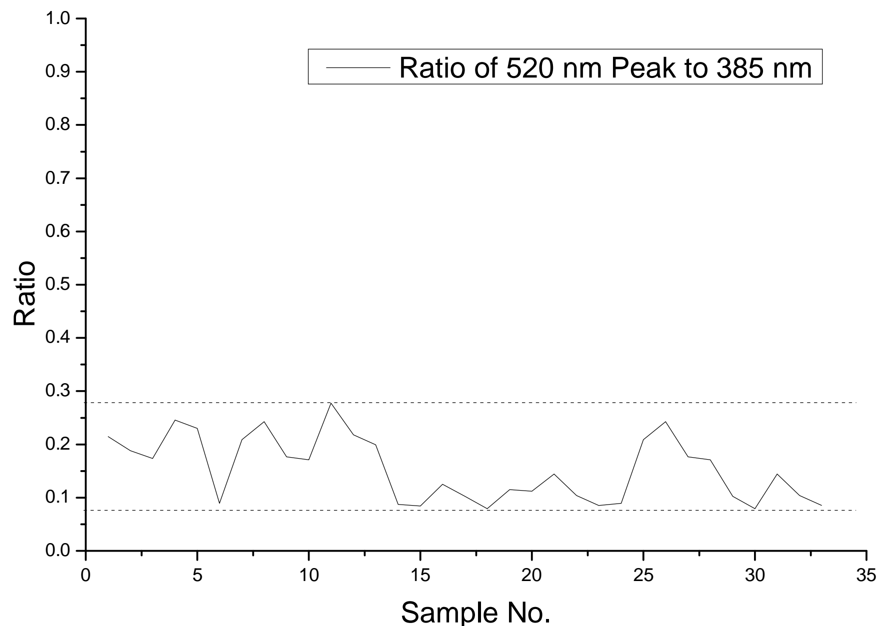

Figure 4.5 *Ratio of the 520 nm peak intensity to the 385 nm peak intensity for a selection of undoped CuCl 500 nm thickness samples. Minimum background intensity has been subtracted from these samples prior to calculations.*

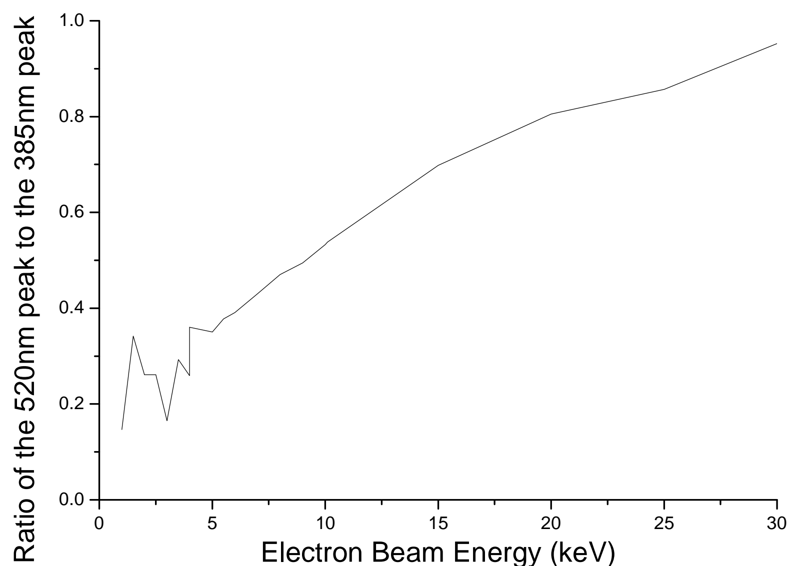

Figure 4.6 *Ratio of the 520 nm peak to the 385 nm peak as the electron beam energy is increased. Test was performed on undoped CuCl samples of 500 nm thickness at a constant current of 1100 pA.*

Figure 4.6 shows the effect of the beam energy on the CL output of this 520 nm band, which allows us to judge the depth at which defect contributions become prominent in the samples. The sample used for this test was an undoped CuCl 500 nm thickness sample after atmospheric exposure of an hour to develop a 520 nm signal significant enough to be measured accurately across the range of keV values.

The small maximum in the relative intensity between 1-2 keV is due to the overall CL at these energies being of extremely low intensity and may be ignored. As the beam energy was increased to 4 keV, there was a clear increase in the intensity emitted from the surface. Using a Monte Carlo simulation of the sample at this energy [92] previously shown in Chapter 2, the penetration depth was found to be over 140 nm. This appears to be a crossover point within the material for a high level defect emission CL signal to be observed. Similarly between 20-30 keV (and presumably beyond, although the limit of this SEM is 30 keV) we can see a levelling off of the relative 520 nm intensity. This can be attributed to both finite thickness of our sample

and the recombination and re-absorption effects within the material that will inhibit deep level emission as the depth is increased.

Previous studies [107] and our own observations have shown that the Si substrate does not contribute to the 520 nm or other emission bands. Therefore, the luminescence observed above this beam energy comprises luminescence from within the entire CuCl layer and no further changes in the band edge to deep level emission are seen, as expected.

In figure 4.7 (a) and (b) we can see the increase in the beam energy has allowed us to image defects from beneath the surface of the material. The white shapes in (b) were not present in the 4 keV CL image or in the SEM image (a). Their position within the material can be ascertained by varying the beam energy and recording the

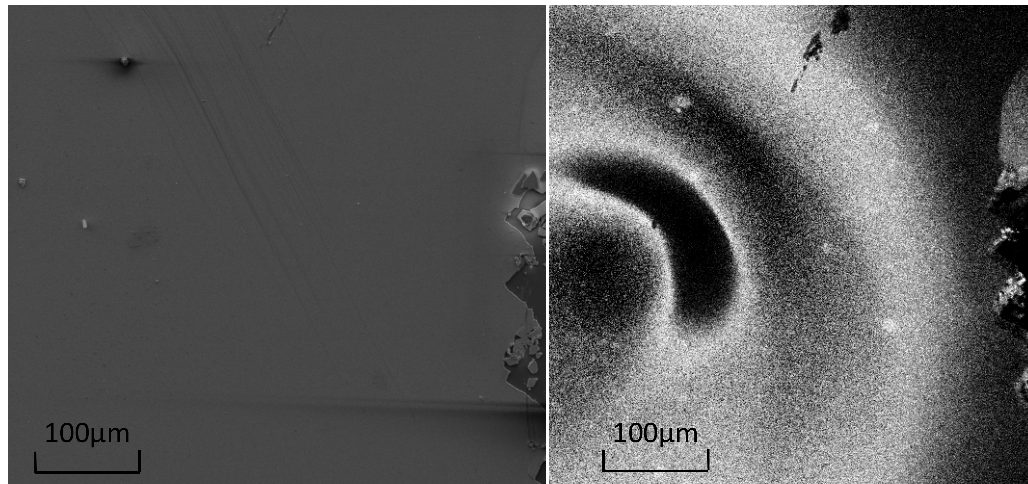

(a) (b)

Figure 4.7 *Comparison images of the same area using (a) Secondary Electron imaging and (b) the subtraction from each other of two CL images recorded in polychromatic mode at 4 keV and 30 keV. Differences between the beam energy images are clearly seen with the brighter material stemming from the deeper scan of 30 keV.*

CL spectra at various beam energies. Combined with the penetration depth of the beam energy this would allow their depth within the material to be ascertained. Several different samples have been tested with similar outcomes. The sample of highest quality (in terms of integrated PL intensity detailed in previous work [99]) was chosen for the scans displayed here. Due to the inherent spatial resolution limitations of the digital CL equipment, this technique was unable to directly image the sources of luminescence at the grain level within the material as originally intended. Deep level defect detection represents an alternative use for the technique, mapping the luminescence beneath the surface of the material which is distinct from each of the other luminescent techniques discussed in this work.

4.3 KCl Samples

The CL spectra of the undoped KCl-CuCl sample shown in figure 4.8, matches the general shape of the CuCl spectra with one notable addition, an accentuation of the 520 nm defect band at smaller wavelengths than previously seen. If we treat the defect band as containing two separate broad peaks, the existing 520 nm peak is supplemented by another broadband peak centred at 490 nm. The cause of the 490 nm peak is not known at present as it can appear in CuCl samples but is consistently present in all KCl-CuCl samples. Aside from this peak the spectra of the undoped KCl-CuCl samples appears to match the undoped CuCl samples with a similar slight variance of the central peak at 385 nm between samples.

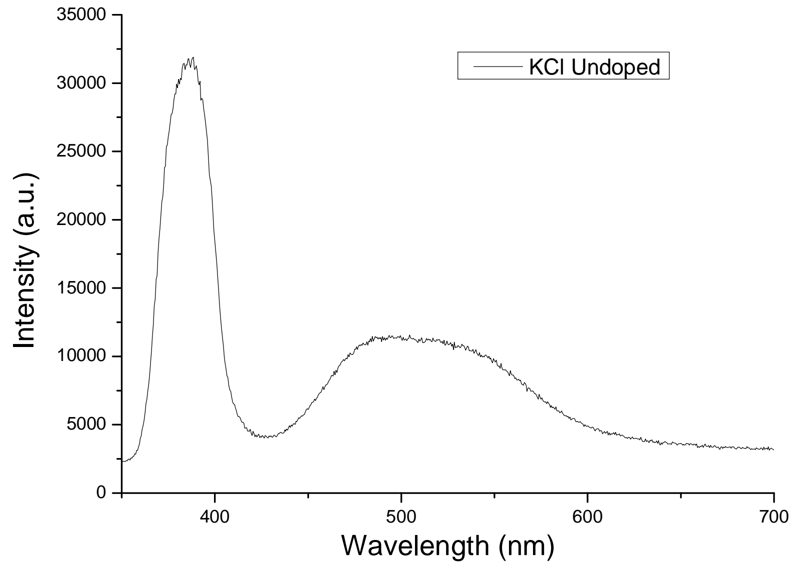

Figure 4.8 *CL spectrum for an undoped sample of KCl-CuCl in the mixture ratio 20:80. Beam energy was set to 15 keV with a probe current of 500 pA.*

This 490 nm peak is further demonstrated in figure 4.9 which shows a range of CL spectra for different undoped KCl-CuCl samples each containing this peak at different levels of intensity. These spectra also illustrate the repeatability of the KCl-CuCl samples, with the FWHM of the Z_3 exciton peak remaining consistent and the variance of the intensity ratio of the 520 nm peak to the Z_3 exciton peak shown in figure 4.10. The gridlines show the variance in the values with the ratios remaining between 0.24 and 0.36 which is an increase of 0.1 over the CuCl undoped samples. This shows that the addition of the KCl mix to the CuCl samples leads to an increase in the concentration of deep defects compared to the standard CuCl thin film samples [65]. This should lead to a decrease in the conductivity of the material but instead leads to an increase due to interstitial ionic hopping of K^+ in the CuCl crystal matrix which more than compensates for the deep defect concentration increase [95].

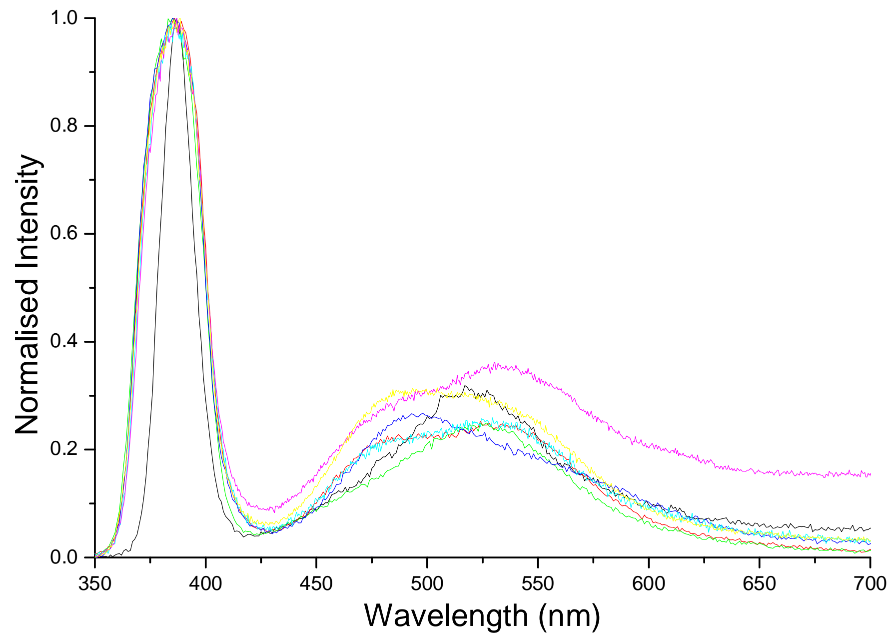

Figure 4.9 *Cathodoluminescence spectra for undoped samples of KCl-CuCl in the mixture ratio 20:80 normalised to the peak of maximum intensity at 385 nm. Beam energy was set to 15 keV with a probe current of 500 pA.*

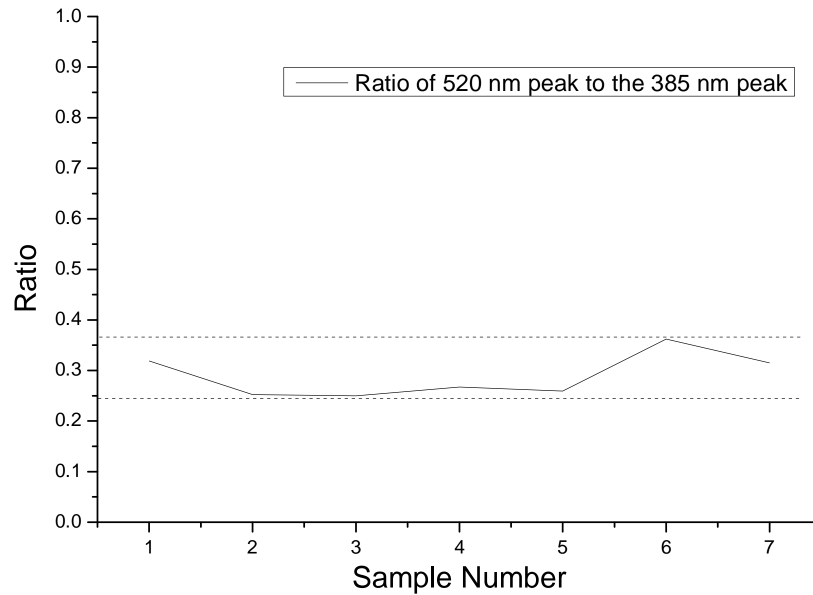

Figure 4.10 *Ratio of the maximum intensity of the 520 nm peak to the 385 nm peak across a range of undoped KCl-CuCl samples. Dotted lines show the range of the values recorded*

4.4 Oxygen Doping

Previous studies of the conductivity of CuCl thin films have shown that when doped with oxygen there is a decrease in the optical quality of the films, a negative thermal quenching effect [108] and an increase in the conductivity [109]. Oxygen is incorporated into anion vacancies and thus enhances the density of the holes and creates p-type conductivity in the CuCl thin films [110, 111]. It should be noted that reliable conductivity measurements of CuCl thin films on Si substrates have not been performed due to the difficulty in applying metal contacts to the surface of the material, the referenced increase in conductivity was measured on a bulk sample of CuCl.

To investigate these effects, doping was performed using an Oxford Instruments Plasma Lab Plus 800 Reactive Ion Etcher (RIE). This places the specimen in a low pressure environment of 50 mTorr and introduces oxygen and argon into the chamber at flow rates of 80 sccm and 20 sccm, respectively. The effect of the doping on the properties discussed for the KCl and CuCl thin film samples were most apparent after the first doping treatment.

An immediate increase in the 520 nm signal was recorded relative to the 385 nm peak (figure 4.11). Each of the spectra have been normalised to the position of minimum intensity, the undoped value given at 0 seconds. This is to illustrate the increase present in each of the samples and also to show that the CuCl samples exhibited the largest increase in this region due in part to the KCl samples' higher starting defect band intensity discussed in the previous section. Both the CuCl and KCl samples reached a maximum ratio of 0.66 relative to the 385 nm peak at 450 and 900 seconds. This increase was achieved by the samples doped for longer increments

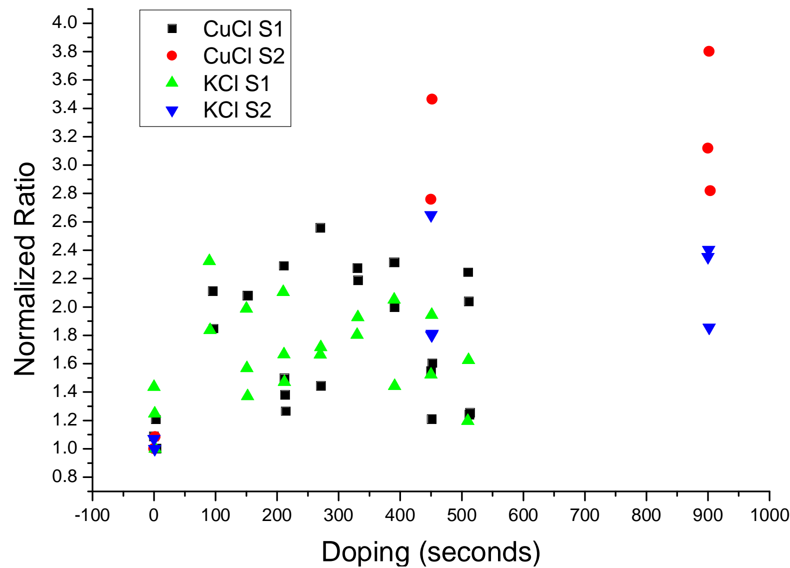

Figure 4.11 *Normalised values for the ratio of the 520 nm peak to the 385 nm peak as the level of oxygen doping is increased. S1 and S2 denote difference samples. Multiple data points at the same doping level represent tests at different points in the sample to show variance*

indicating the requirement for the oxygen to penetrate deep within the sample to increase the 520 nm band relative intensity.

Distinct differences were measured for the samples, with changes notable in the FWHM values, the ratio of the intensity of the 385 nm to 520 nm peaks and the maximum intensity of the 385 nm peak itself.

The FWHM values displayed in figure 4.12 showed an immediate decrease once doping began, dropping almost 10% when compared to the undoped values present at 0 seconds on the graph. However they slowly increase until around 400 seconds before dropping off again. Further doping was shown to decrease the FWHM more indicating there is no further resurgence in the FWHM signal. As previously mentioned the FWHM signal is highly dependent on the micrometer setting for the CL

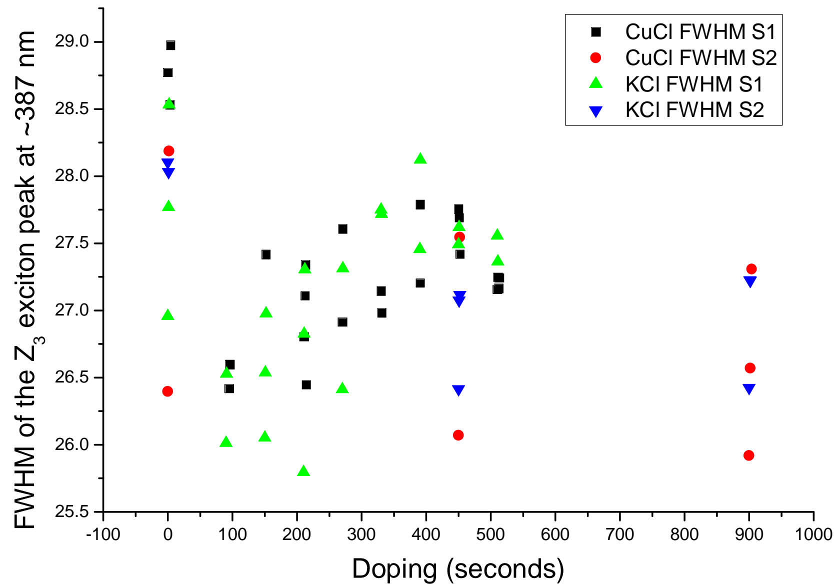

Figure 4.12 *Normalised values of the FWHM for the 385 nm peak as the level of oxygen doping is increased. Multiple data points at the same doping level represent tests at different points in the sample to show variance*

equipment which was kept at a constant 10 mm throughout testing. The spectrometer resolution is 1 nm and this coupled with the sensitivity of the FWHM to the micrometer setting naturally calls the reliability of these results into question. However, these results indicate there is an ideal level of plasma exposure to maintain a high Z_3 exciton intensity coupled with the conductivity increase offered by the doping technique itself which is supported further as we continue our analysis by examining the maximum peak intensity of the Z_3 exciton peak as doping is increased.

The spectra used to calculate the maximum peak intensity have been normalised to the peak of maximum intensity in figure 4.13 but it is notable that this maximum is not present at the undoped peak position across all samples. In fact only the CuCl S1 sample has the maximum peak intensity at the undoped position, each of the other samples achieve maximum intensity in the region around 400 seconds similar

to the FWHM graph. These luminescent properties and ideal doping region will be examined further in our discussion of the optical properties in Chapter 5.

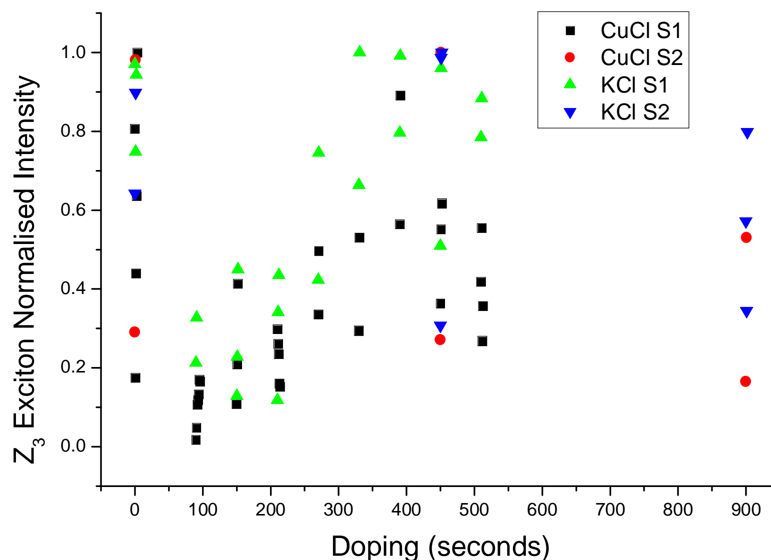

Figure 4.13 *Normalised values for the maximum peak intensity of the 385 nm peak as the level of oxygen doping is increased. Multiple data points at the same doping level represent tests at different points in the sample to show variance*

4.5 EDX Imaging

Energy dispersive x-ray microanalysis was used to chart the change in the relative concentrations of atoms present as the samples were doped with oxygen. This technique results in the output of EDX spectra with software analysis used to calculate the atomic quantity of each material in the area under investigation. Figure 4.14 shows the undoped EDX spectra for both CuCl and the KCl-CuCl samples. Although dominated by the Si peak, when the percentage values for Cu and Cl are combined the CuCl:Si ratio is approximately 60:40 as illustrated in figure 4.15. When comparing the CuCl and KCl-CuCl samples, notable differences are the presence of trace elements of

K but also significant levels of bromine (Br) within the sample. Br was present at significant amounts in every sample of KCl-CuCl measured but only at trace amounts in the CuCl samples shown by the peak's presence left of Si. The addition of KCl to the mix didn't influence the level of Cl which remains unchanged within experimental error.

O was detected at low levels in both samples showing how quickly the decay process begins as both samples were tested an hour after deposition. To see if the O levels increase at a constant rate, a selection of samples were exposed to the natural levels of O present in atmosphere for a further hour and retested. No significant change was measured indicating the O presence increases rapidly upon initial atmospheric exposure across the surface of the sample, taking longer to penetrate the depths of the sample and cause the characteristic decomposition of CuCl in atmospheric conditions.

The traces of K found were at significantly lower levels than the amount used in the deposition process, a ratio of approximately 0.5:99.5 for K and CuCl compared

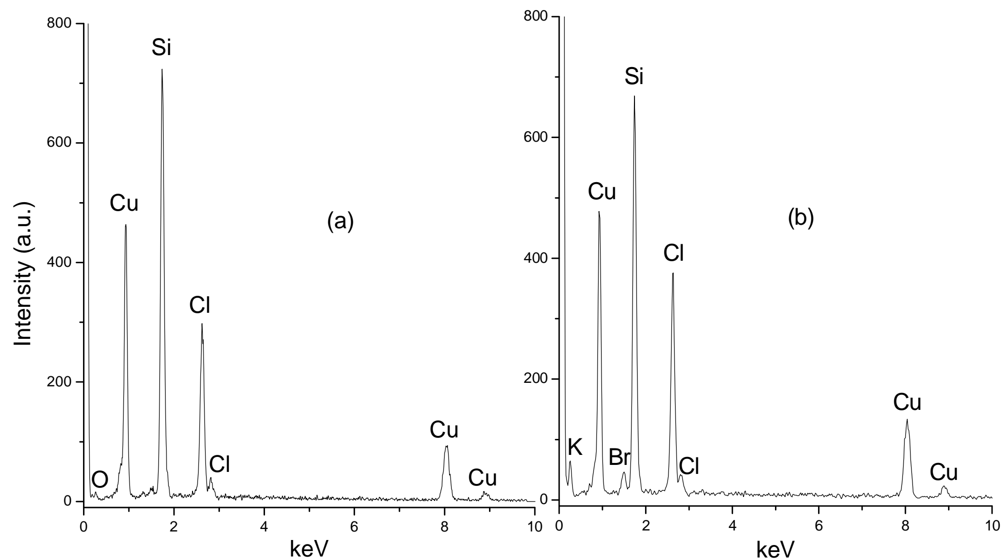

Figure 4.14 *EDX spectra for (a) 500nm CuCl thin film sample and (b) 500nm KCl-CuCl thin film sample*

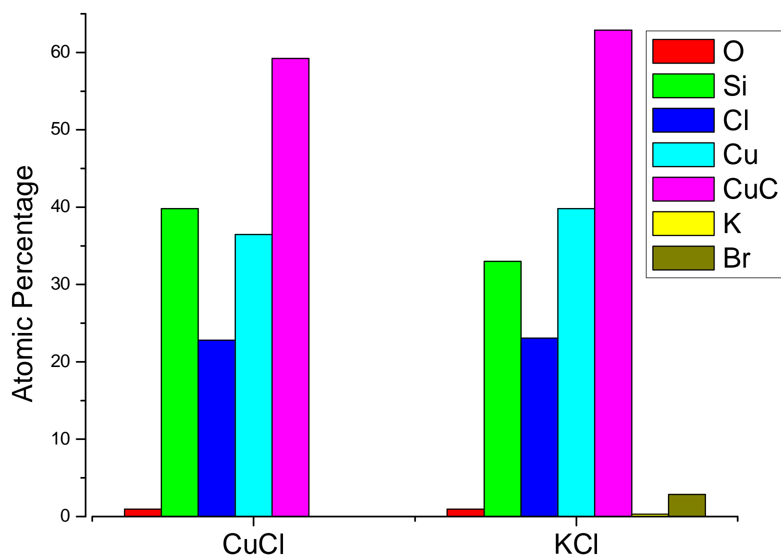

Figure 4.15 *Bar Graph showing the atomic percentages for both the CuCl and KCl-CuCl samples. The values included for CuCl represent the result of the sum of both the Cu and Cl contributions.*

to the deposition ratio of 20:80 for KCl and CuCl. This indicates that rather than forming large amounts of the K_2CuCl_3 compound on the surface of the material, the KCl is only present in limited amounts possibly wherever there are anion Cl^- vacancies on the surface of the material [49].

Oxygen doping of the samples leads to an expected increase in the levels of O present. Figure 4.16 shows that this increases nearly linearly, with the disparity between the S1 and S2 samples possibly due to an accumulation of additional factors; oxygen exposure time as a higher number of tests were performed on the S1 series, slightly longer plasma exposure due to the beam startup in the machine itself, etc. It's clear that each of the samples displays a linear dependence on the plasma beam exposure and remains broadly consistent across multiple tests indicating that O is entering the thin film material as intended at a constant rate.

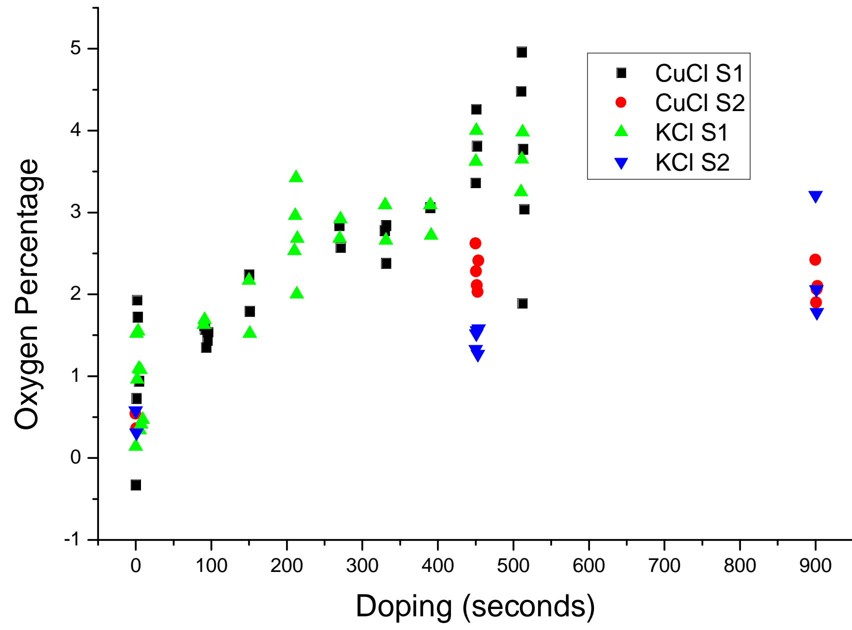

Figure 4.16 *EDX Atomic percentage for Oxygen as doping is increased*

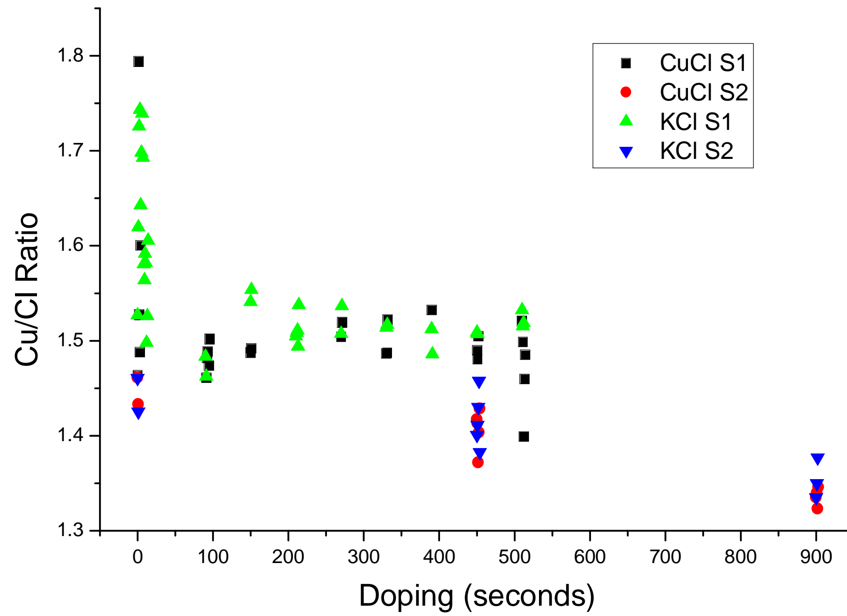

Figure 4.17 *EDX Atomic ratio for Cu to Cl as doping is increased*

Since the ratios of CuCl to Si show a high level of variance depending on the area of the sample under examination and testing the same area multiple times diminishes the signal, the ratio of Cu to Cl was used to illustrate the material change as the doping is increased. It was found that as doping increased, the level of Cu constantly decreased. This effect was linear for the samples with long plasma exposure times, and deviated from linearity for the samples tested routinely every 60 seconds as we can see in figure 4.17. The multiple data points at each doping position indicate different areas tested across the samples to ensure the surface variance was taken into account. Complementing this is a slight increase in the levels of Si recorded, indicating that the CuCl film thickness has reduced as the system is able to detect the underlying Si substrate more effectively.

For the KCl-CuCl samples, K values are found to remain unchanged throughout the plasma process as seen in figure 4.18. There may be a slight increase in their percentage as doping is increased, but the values measured are far too low to

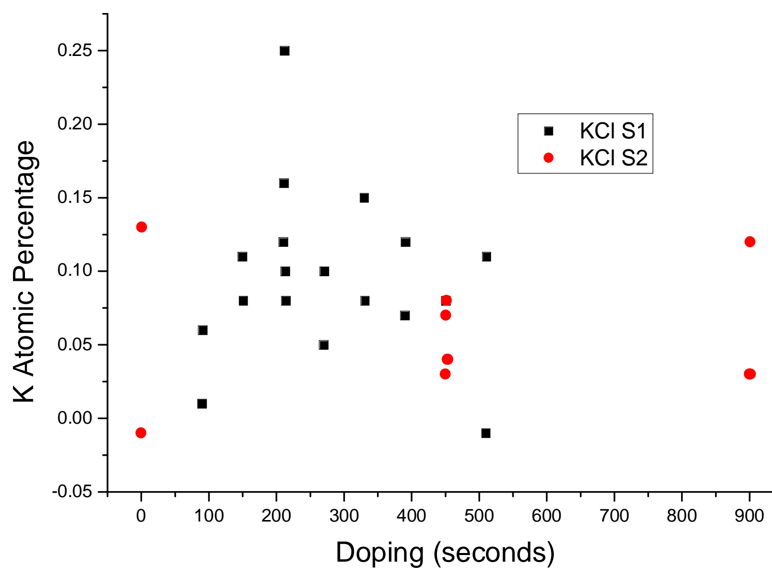

Figure 4.18 *EDX Atomic percentages for K in the KCl-CuCl samples as doping is increased*

make any clear conclusions. It is clear that there is no decrease in their values, which indicates that they are not reduced in the same manner as Cu.

Secondary electron (SE) images from the SEM can be used to show the direct effect of the plasma process on the surface of the material. It is important to clarify that the scarring effect produced by the plasma process in atomic properties and surface structure is entirely different from that produced by the oxygen doping process.

For this reason figure 4.19 shows images of the CuCl and KCl-CuCl samples before and after doping and also after decay due to atmospheric conditions. The images shown are the same area used for the EDX scans. The undoped KCl-CuCl sample was imaged at a higher degree of magnification because the material was suited to such analyses, probably due to an increase in the conductivity provided by the KCl inclusion. At greater magnification the surface topography is practically identical to the CuCl undoped sample pictured in (a). As we can see in (c) and (d), the doping process has caused a series of scarring effects across the surface of the samples. Further EDX tests at each of these darker sections on the images confirmed a raised percentage of Si compared to surrounding areas indicating that this effect is scoring away the thin film surface, as commented upon earlier. The raised sections in these doped images show similar atomic percentages to the surrounding area. It is possible that the plasma treatment is destabilizing the material’s attachment to the substrate leading to the presence of these raised regions. The proportion of lighter sections in the doped images is the same as our undoped samples. However the decayed samples show a significant increase in these lighter areas which further EDX scans revealed to be concentrations of CuCl material. This allows us to conclude that the topographical effects caused by the oxygen doping and atmospheric decay are entirely distinct, probably due to the absence of the moisture reaction in the plasma doping samples.

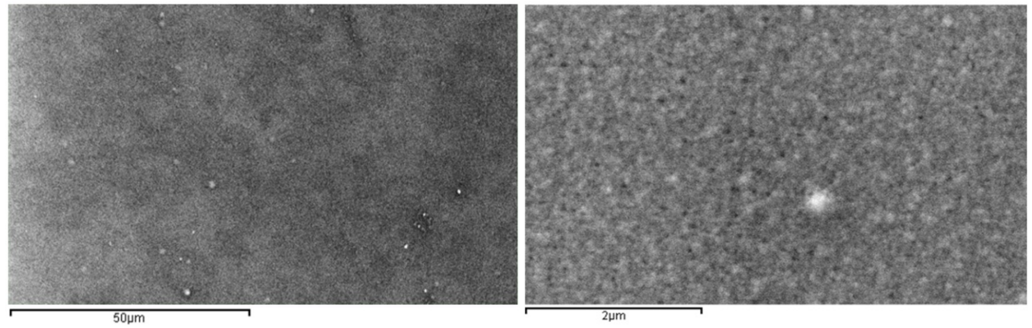

(a) (b)

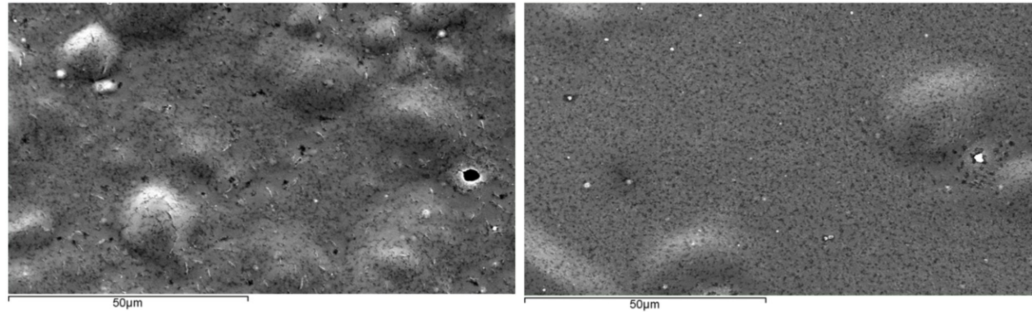

(c) (d)

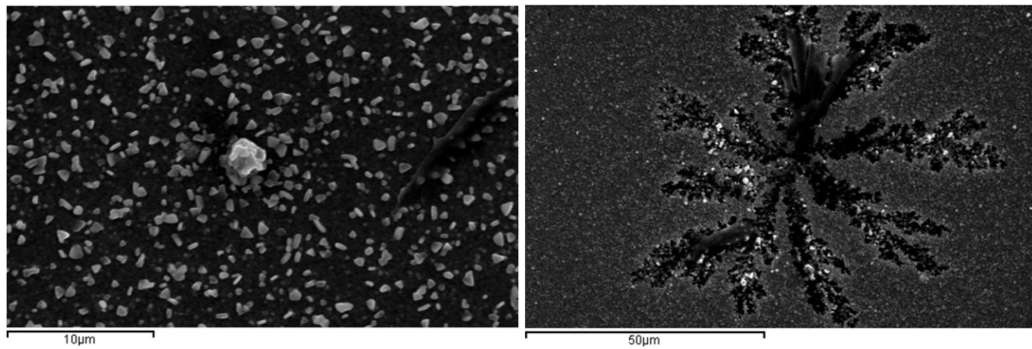

(e) (f)

Figure 4.19 *SE images for CuCl (left column) and KCl-CuCl (right column) samples showing the change in the surface area as due to doping and atmospheric decay. (a) and (b) show the undoped surface for a CuCl and KCl-CuCl sample, (c) and (d) show the surface for the same CuCl and KCl-CuCl samples after 900 seconds of plasma doping and (e) and (f) show the surface of a CuCl and KCl-CuCl sample after decay due to atmospheric exposure.*

The pattern seen in the decayed KCl-CuCl sample is a feature also visible in decayed CuCl samples. Further decay of (e) would result in the production of these features. EDX analysis of the darkened region of these features shows a decreased ratio of Cu to Cl over the surrounding areas and also when compared to most of our doped and undoped samples. The ratio is 1.3 which is comparable to the values of our doped samples after 900 seconds as previously shown in figure 4.17. Further scans of the wire-like formations at these points recorded at greater magnifications show that the Cl percentage actually surpasses that of the Cu, leading to a Cl:Cu ratio of ~0.7.

The shape of the CL spectra from these decayed sections is indistinguishable from those of the oxygen doped samples in all aspects except for a decrease in the intensity of the Z_3 385 nm peak. The regions of material outside of this darker area show high concentrations of CuCl, varying around 1.75. The decayed samples of CuCl are similar to this, varying between 1.75 and 1.95, which reaches values significantly higher than any of any of the other samples measured. This points to the accumulation of Cu material near the surface of the samples as atmospheric decay occurs, with further decay leading to a removal of Cu material from the sample itself as visible the darkened regions shown in (e).

4.6 Summary

Within this chapter we saw the use of a digital CL camera to image the deep level defects within the material, but proper usage of this technique remained restricted due to the poor spatial resolution of the equipment itself. However this technique is extremely promising in future studies of CuCl material. By slowly increasing the penetration depth of the electron beam and recording digital CL images throughout, a

3D map of the defect band locations within the CuCl material can be plotted. This would greatly assist with answering some of the outstanding questions regarding the source of the defect band, especially if capable of being recorded at high resolutions.

The line spectra produced from CL studies of the undoped CuCl samples showed the Z_3 exciton position and the 520 nm defect band as the main features. The ratio of the defect band intensity to the Z_3 exciton intensity was shown to be consistent across multiple samples allowing a clear increase in this ratio to be discerned for the KCl-CuCl samples. This was also the case for the doped samples, with the ratio increasing in a similar but more erratic, style. Examination of the FWHM and maximum intensity of the Z_3 exciton peak fluctuation as doping is increased indicates that there is an ideal region for doping. After an initial decrease in both properties, the FWHM and maximum intensity increases up to around 400 seconds before decreasing once more. This effect was present in both CuCl and KCl-CuCl samples. The lack of the emergeance of this region in the XRD section indicates that these are optical properties which may also be present in the PL and reflectance analysis.

EDX imaging allowed us to calculate the atomic percentages for the both the CuCl and KCl-CuCl thin film samples. Expected ratios of Cu, Cl, Si and O were found in the CuCl samples with the addition of trace elements of K and Br found in the KCl-CuCl samples. This shows us that despite the inability of the other methods of characterization to detect the presence of the KCl salt, the deposition of KCl and CuCl on the same Si substrate has been successful, albeit at lower stoichometry levels than expected based on the ratio of the mixture used (80:20).

The SEM images at the close of this chapter show the physical scarring effects of the doping process on the surface of the CuCl material in a more tangible manner. It is clear this process is etching layers of CuCl material from the surface of

the thin films. However the bubbling pattern seen in these images as doping is increased remains unexplained. In future works a test could be performed by isolating a section of the CuCl thin film for exposure to the plasma and examining the interaction of these bubbles with undoped CuCl material. Alternatively multiple high resolution SEM images could be recorded of the doped material at various zoom levels. The sample could then be cleaved in two and the location of the cut matched with the high resolution SEM images. The sample could be rotated and the underneath of one of these structures probed with analysis using both the SEM and EDX equipment.

Chapter 5

Optical Properties

5.1 Introduction

This section reports on the analysis of photons emitted from the near surface region of our thin film material when struck by light whilst the samples are contained within a low-temperature cryostat system. We begin by detailing the PL results for the undoped CuCl thin films and discussing the distinctive features of these spectra. These consist of the exciton and bi-exciton spectral positions and the relative intensities of each of the peaks detected. The calculation of the exciton binding energy from the exciton peak positions is discussed. A brief summary of the temperature dependence of the PL spectra and the effects of atmospheric exposure on the PL spectra is also discussed before moving on to the KCl-CuCl and doped samples. Alterations to the established CuCl exciton positions are described in this section with notable increases of PL peaks not previously present in CuCl for the doped samples.

Reflectance scans were used to record both the Z_3 and $Z_{1,2}$ exciton positions in the next section, before a similar summary of the observed properties detailed for the PL section. As before, once the CuCl undoped sample properties have been discussed, the differences caused by the addition of KCl and oxygen doping to the spectra is examined with a notable change in the optical properties recorded once doping commences.

Finally reflectance modelling of the undoped CuCl samples is used to calculate the various parameters affecting the shape of the reflectance spectra observed. These include the exciton polariton dispersion curve, exciton energy positions, damping, transverse and longitudinal splitting, effective exciton mass, thickness of the thin film samples and the dead layers present at the interfaces within the samples. These properties are compared to previously recorded values obtained for a bulk sample of CuCl. A short discussion on the advantages of this method of characterization compared to the others utilized throughout this work concludes the chapter.

5.2 Photoluminescence

5.2.1 Undoped CuCl Photoluminescence

We have optically characterised CuCl and KCl-CuCl samples on thin films at various oxygen-doping durations and etch solutions using temperature dependent photoluminescence. The properties of the spectra are best observed at lower temperatures, with room temperature scans of the samples failing to produce detectable signals due to the low excitation intensity levels used in the excitation process. This is best demonstrated by the results obtained by our group from a system of higher energy excitation using a low wavelength 244 nm laser setup [99]. This allowed peaks to remain visible as room temperature approached and a relatively high level of intensity at lower energy values. However in order to ensure testing occurred on the same samples for the doping and KCl-CuCl testing as soon as possible, an alternative PL setup was required. These measurements (being those used throughout this thesis) were recorded using a 325 nm HeCd laser which typically allowed 3 distinctive peaks

to be distinguished with the readings recorded at the low temperature limit of the cryostat of ~20 K shown in figure 5.1 being one of the few where 4 peaks are visible.

Each of the peaks present in this spectra and the corresponding photon energy values are the exciton and biexciton energies of the CuCl material. Starting from the higher photon energy side, we can see the Z_3 free exciton peak, typically recorded at 3.202 eV which closely matches previous results for both thin film (3.203 eV at 10 K [26]) and bulk samples (3.208 eV at 6 K [15]) and the values recorded at room temperature in the CL results section when temperature shift is taken into account (3.202 eV = 387 nm, with the CL peak recorded at 386 nm). The next peak is the peak of maximum intensity, the I_1 impurity bound exciton doublet peak at 3.180 eV with Cu vacancies in the material thought to be responsible for this defect-related emission [112].

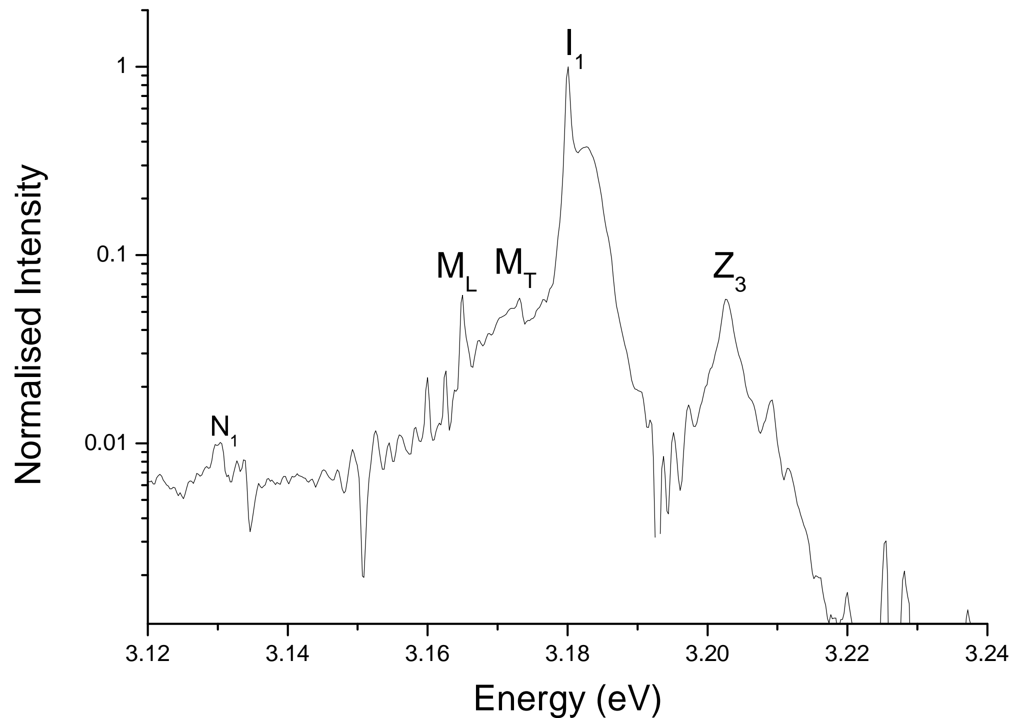

Figure 5.1 *PL Spectrum for nominal 500 nm thin film CuCl sample on (100) Si*

At lower energies are the peaks at 3.165 eV and 3.172 eV ascribed to the free longitudinal and transverse contributions of the biexciton M and being the result of excitonic molecule recombination [20]. The relative intensity of the longitudinal and transverse peaks matches those previously recorded for bulk CuCl [113], with the M_L values being used for further analysis as they match the accepted M value used in binding energy calculations. Finally at the lowest energy of 3.130 eV is the N_1 impurity bound biexciton. The impurities responsible for the N_1 and I_1 peaks are both believed to be from neutral acceptors but these identifications are tentative due to a lack of previous observations of PL peaks associated with impurities under ideal conditions [26].

The information obtained from the PL scans can be used to estimate the binding energy of the bound exciton I_1, the free biexciton M and the bound biexciton

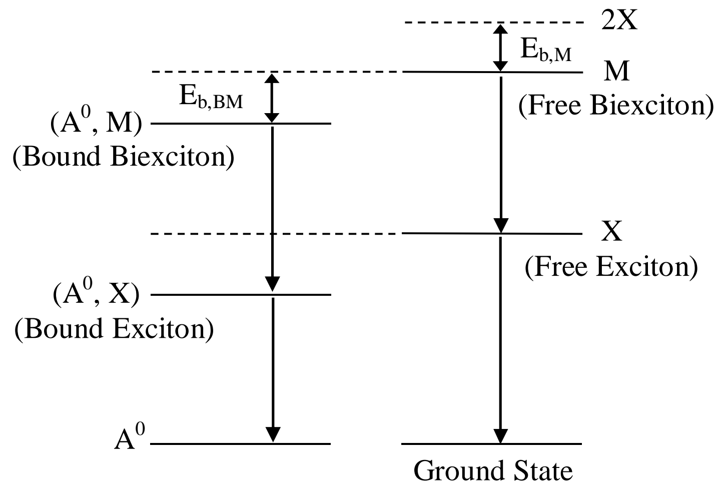

Figure 5.2 *The Nakayama energy scheme for calculation of the exciton binding energies [26]. The left side shows the free states and the right side the bound states. M, X and A^0 denote the free biexciton, Z_3 free exciton and the neutral acceptor. $E_{b,M}$ and $E_{b,BM}$ denote the binding energy of the free and bound biexcitons.*

N_1. This estimation is based on the corrected bound energy scheme calculation (shown in figure 5.2) developed by Nakayama *et al.* [26] and uses the following equations [26, 114, 115]:

$$E_M^B = E_Z - E_M$$

$$E_I^B = E_Z - E_I$$

$$E_N^B = 2E_Z - E_N - E_I - E_M^B \qquad \textit{Eqn 5.1}$$

where E_Z, E_M, E_I and E_N are the energies of the free exciton Z_3 (3.203 eV), the free biexciton M (3.165 eV), the bound exciton I_1 (3.180 eV) and the bound biexciton N_1 (3.130 eV) respectively. E^B represents the binding energy.

The estimated binding energies are 23 ± 2 meV for the bound exciton I_1, 38 ± 2 meV for the free biexciton M and 58 ± 2 meV for the bound biexciton N_1. The binding energies for I_1 and M are quite close to those recorded previously for CuCl thin film on Al_2O_3, 22 and 34 meV respectively. However the binding energy of the bound biexciton N_1 is approximately 12 meV higher than the estimated value recorded on Al_2O_3. However this matches previous results obtained in our group for CuCl thin film samples on Si [116] so these values can be considered our baseline for undoped CuCl samples.

The temperature dependence of the PL spectrum of CuCl is shown in figure 5.3. This shows the large decrease of the I_1 peak, dominant at low temperatures and visible to the left of the image, but quickly superseded by the Z_3 peak to the right. This peak also gradually reduces in intensity as temperature is increased, moving to higher energy and broadening until it can no longer be distinguished. Shown in this graph at low intensity is the biexciton peak M, visible up to 60 K before being lost to background noise. The I_1 peak remains visible until this temperature is reached as well,

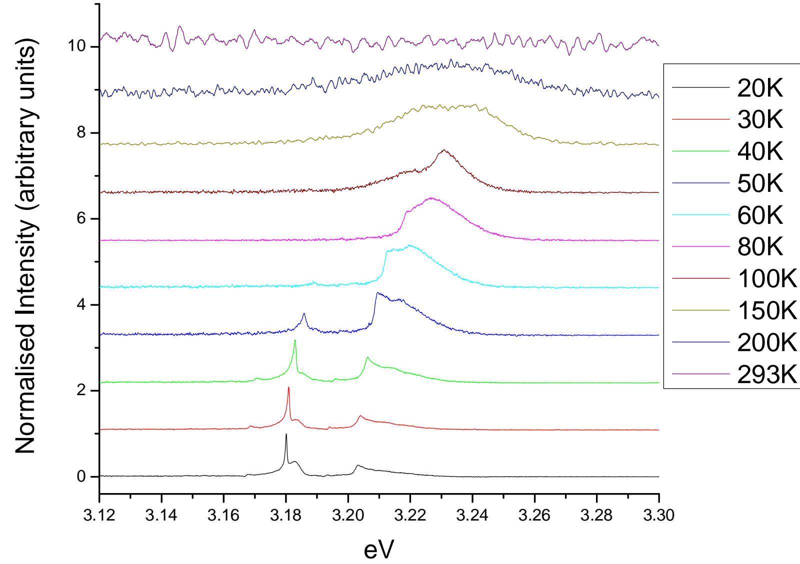

Figure 5.3 *PL scans showing the variation of the CuCl peaks as temperature is increased*

but declines at a higher rate due to its relatively high intensity at 20 K compared to the M biexciton peak. This is probably due to the thermal dissociation of the bound states as the thermal activation energy is ~20 meV [26] which is extremely close to the previously obtained binding energy of the bound exciton of ~23 meV, obtained by the energy difference between the Z_3 free exciton peak and the I_1 bound exciton peak.

The variations in peak energy as the temperature is increased are shown more quantitatively by the graph in figure 5.4. Although the I_1 and M values can only be measured up to 60 K, over this small range they closely match the shape of the Z_3 graph. After 40 K the Z_3 exciton energy is shown to have a linear relationship with temperature in the region examined. This matches the observations made previously by our group, measuring up to the point before the effect of the ion vibrations causes the rate of peak intensity increase to level out [116].

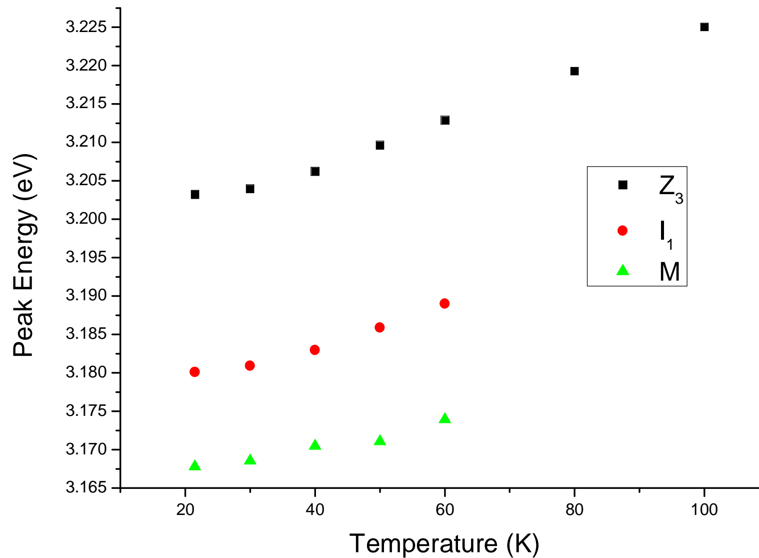

Figure 5.4 *Variation of the peak energies for the CuCl thin film samples with temperature*

To conclude the analysis of the properties of the undoped CuCl thin film samples, it is worth comparing the effects of atmospheric exposure on the PL signal. Figure 5.5 shows the PL spectra for a fresh CuCl sample and one after 24 hours of atmospheric exposure. There is a significant increase in the Z_3 exciton peak intensity and also a reduction in the peak energies of both the Z_3 and I_1 peaks, whilst only trace elements of the N_1 and M peaks are visible. These peaks are masked by a rise in the background intensity and this indicates a decrease in crystal quality of the material seen previously in our XRD scans in chapter 3. The decrease in energy is not uniform for both Z_3 and I_1 peaks, resulting in a decrease of the I_1 bound exciton binding energy from ~22 meV to ~18 meV showing the decay in the exciton's bond with the CuCl material. A broad PL band due to impurities, which can usually be observed on the low energy side of the I_1 band, is not visible in the decayed sample nor any of the samples

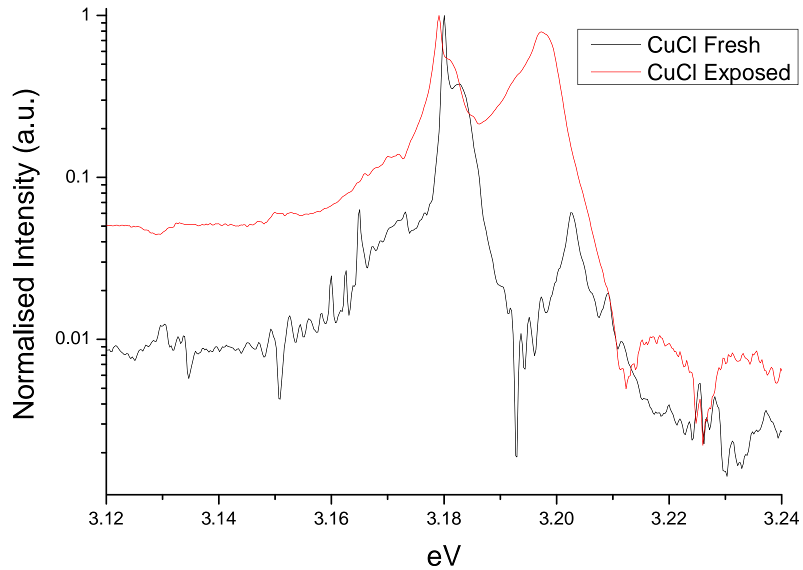

Figure 5.5 *PL spectra of a fresh CuCl sample compared and one after 24 hours of atmospheric exposure*

measured [117]. This band becomes visible at higher excitation levels using the lower wavelength laser excitation setup previously mentioned due to the increased level of input energy this setup provides.

5.2.2 KCl-CuCl PL Analysis

The comparison of the PL spectra for the CuCl and KCl-CuCl samples is shown in figure 5.6. Each of the peaks discussed in our analysis of the undoped CuCl samples is present with only slight alterations to their positions. This reduction of ~0.2 meV to the value of both the I_1 and Z_3 peak positions is probably due to small levels of atmospheric exposure (similar to that observed in figure 5.5) rather than the influence of the KCl dopant. A notable decrease in the peak luminescence intensity values was recorded when comparing the KCl-CuCl sample to the CuCl sample using the same setup for both. This is due to the percentage of the KCl dopant being between 15 –

20% which is above the 5% threshold to increase luminescence intensity but within the key area of increased conductance the optical properties of which are the subject of discussion [95]. The close resemblance of this spectrum to the CuCl spectra shows that the KCl-CuCl thin films are dominated by the CuCl component, with the KCl component distributed throughout the film at far lower percentages than those included in the deposition ratio (80:20). No evidence of the K_2CuCl_3 compound formation on the surface has been found.

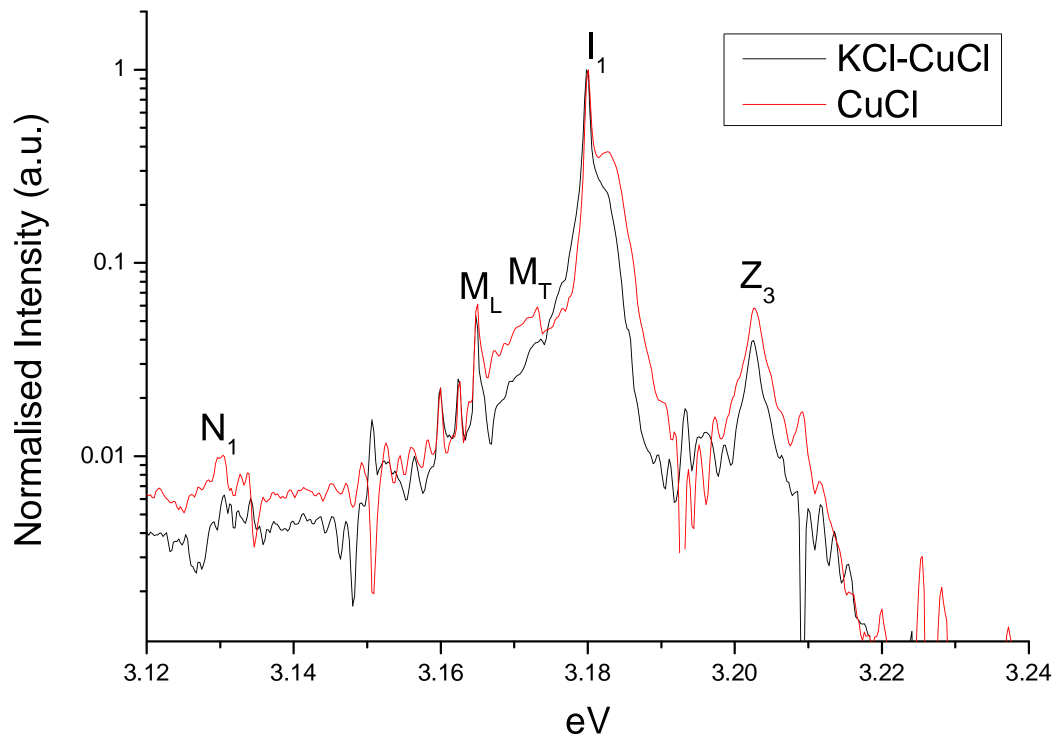

Figure 5.6 *PL spectra showing the KCl-CuCl thin film compared with the undoped CuCl sample. The spectra have been normalised and are shown on a log-scale to ensure the visiblility of all peaks.*

5.2.3 Oxygen Doping PL Analysis

The oxygen doping was performed using the same setup and levels of exposure as detailed in previous chapters. Most notable was the lack of effect on the exciton energy positions the process had, with previous work showing a relatively large shift of ~20 meV in the Z_3 exciton position and ~10 meV in the I_1 position [64]. The samples of both CuCl and KCl when doped up to 900 seconds were found to vary only by ± 0.5 meV in the Z_3 position and ± 0.05 meV in the I_1 position, with no conclusive trend between the different samples. This could in part be caused by the lower level of excitation energy used in the PL system, but this should result in the biexciton processes being rendered at reduced intensities and not effect the exciton energy position itself.

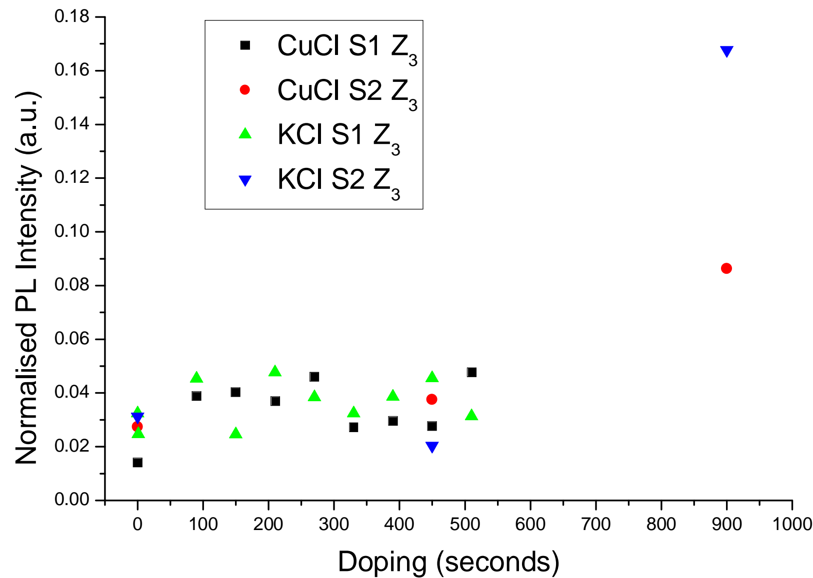

Figure 5.7 *Normalised PL intensity for the Z_3 exciton peak as oxygen doping levels are increased. As per the previous graphs, the intensity values have been normalised to the I_1 intensity. The S1 and S2 values indicate sets of samples doped at 90 second intervals and 450 seconds respectively.*

Instead of analysing the energy values, we must scrutinise the alterations in the recorded relative intensity of the exciton peaks to notice the effects of the doping process. Figure 5.7 clearly shows the increase in the intensity of the Z_3 peak relative to the I_1 intensity only becomes prominent at high levels of doping, with the 900 second doped samples showing relatively high intensity levels which match results previously observed for doped CuCl samples [108]. Rather than point to an increase in the visibility of the Z_3 exciton peak, these results instead illustrate the deterioration of the I_1 intensity and the general optical quality of the material as the Z_3 peak becomes relatively significant without showing any large increase in overall absolute intensity when compared with surrounding background values.

More notable is the significant emergence of the peak at 3.187 eV as doping was increased. Shown in figure 5.8, the increase in intensity recorded was only present in the CuCl samples and grew to such an extent that it dominated the spectrum at

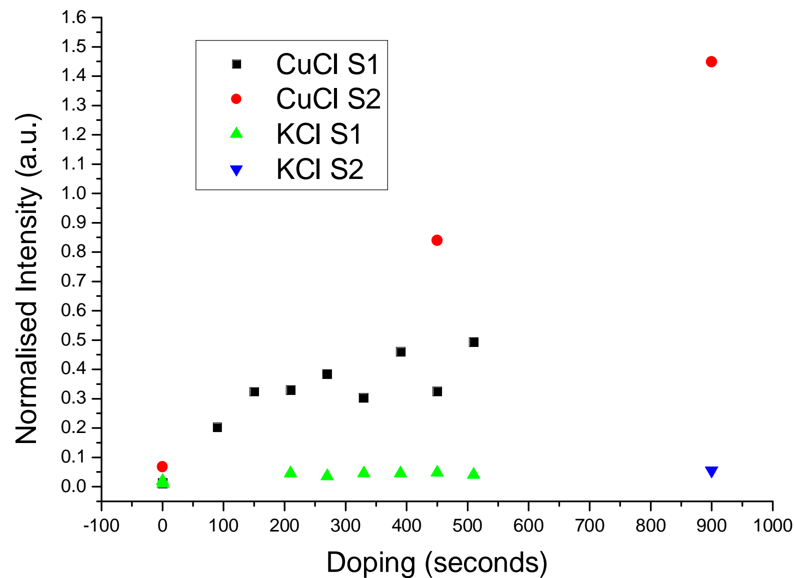

Figure 5.8 *Normalised PL intensity for the peak detected at 3.187 eV. Graph has been normalised to the I_1 intensity.*

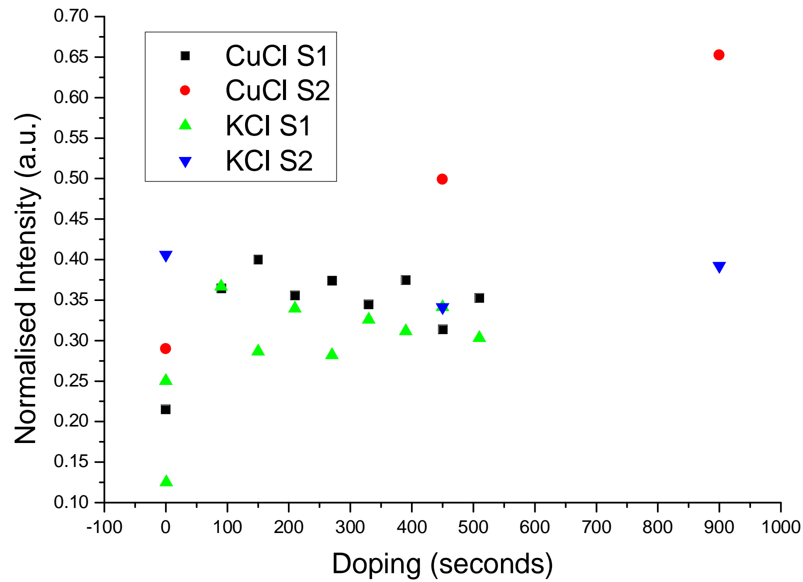

Figure 5.9 *Normalised PL intensity for the broad peak detected at 3.182 eV. Graph has been normalised to the I_1 intensity and illustrates how the I_1 peak intensity is decreasing relative to the 3.182 eV emissions*

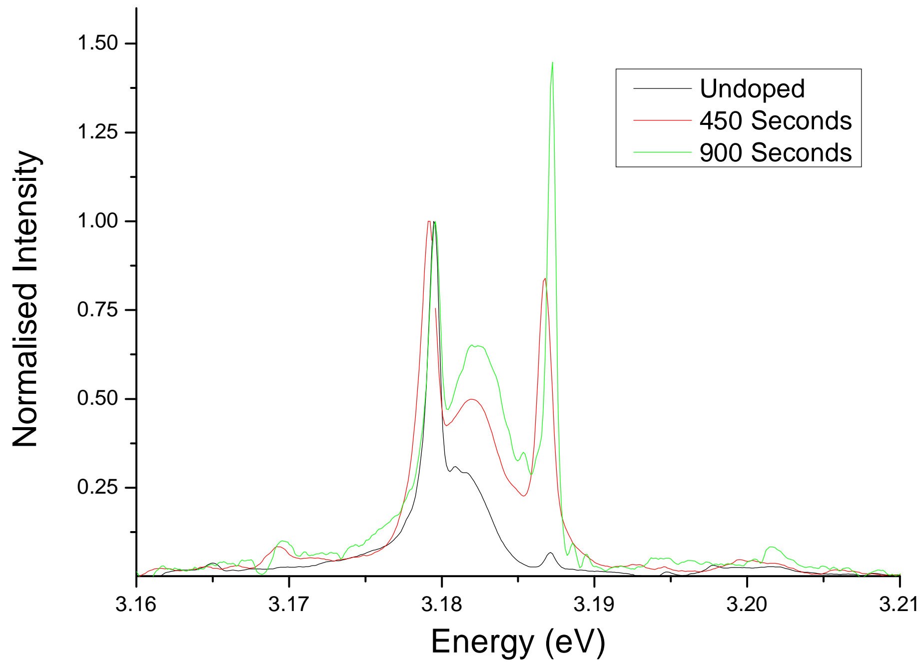

Figure 5.10 *Normalised PL intensity of the 450 second doped samples showing the increase in intensity of the peaks at 3.182 eV and 3.187 eV*

higher doping levels reaching a relative intensity of 1.4 when compared to the I_1 intensity. The emergence of this peak structure can be clearly seen in figure 5.10 which shows the normalised peak intensity of the 450 second doping series. These have been normalised to the I_1 peak intensity. Since it fails to increase during the KCl doping process it appears to be inhibited by the K^+ atoms in these samples, but not entirely blocked. This phenomenon may be related to the relative increase of another broad peak centred at 3.182 eV shown in figure 5.9. Once again the increase is only present in the CuCl samples. This broad region shoulders the I_1 exciton peak and may in some way be a secondary peak related to it but at present the cause of the increase remains unknown.

5.3 Reflectance Analysis

5.3.1 CuCl and KCl-CuCl undoped samples

Reflectance measurements were performed on each of our samples at low temperatures using the setup detailed previously in chapter 2. Near-normal incidence (~6°) was used for each of the reflectance scans recorded to minimise the mixing of longitudinal and transverse modes and result in the presence of only transverse modes in the resultant spectra. Use of these conditions will enable the reduction of the boundary conditions to a one-dimensional scalar system of simultaneous equations for the purpose of modelling.

The single crystal samples reported in the literature [118] and used as our reference in this section did not include the Fabry-Perot fringes visible in our graph, which occur due to multiple reflections from within the CuCl thin films and are dependent on the thickness of the material. These fringes are clearly visible at the

lower energy levels with the fringes at higher photon energies less visible due to the strong excitonic reflection from Si. The parameters for reflectance that cause these fringes are best ascertained by using a modelling program based on the exciton-polariton dispersion relation and boundary conditions and this will be discussed in the next section. In this section we will limit our analysis of the reflectance spectra to the exciton peak positions and relative intensities for the CuCl, KCl-CuCl and doped samples.

Figure 5.10 shows us these for undoped CuCl. These scans were recorded at 20 K with a deposited layer of aluminium on Si used as a reflectance reference to ensure the reflectance calculated is for CuCl thin film rather than any other factors. We can clearly distinguish the Z_3 and $Z_{1,2}$ transverse exciton peak energies at the reflectance maxima, with the corresponding longitudinal exciton energies present at the intensity minima and at slightly higher energy levels. The values of the Z_3 and $Z_{1,2}$ transverse energies are determined to be 3.2036 eV and 3.2724 eV respectively which

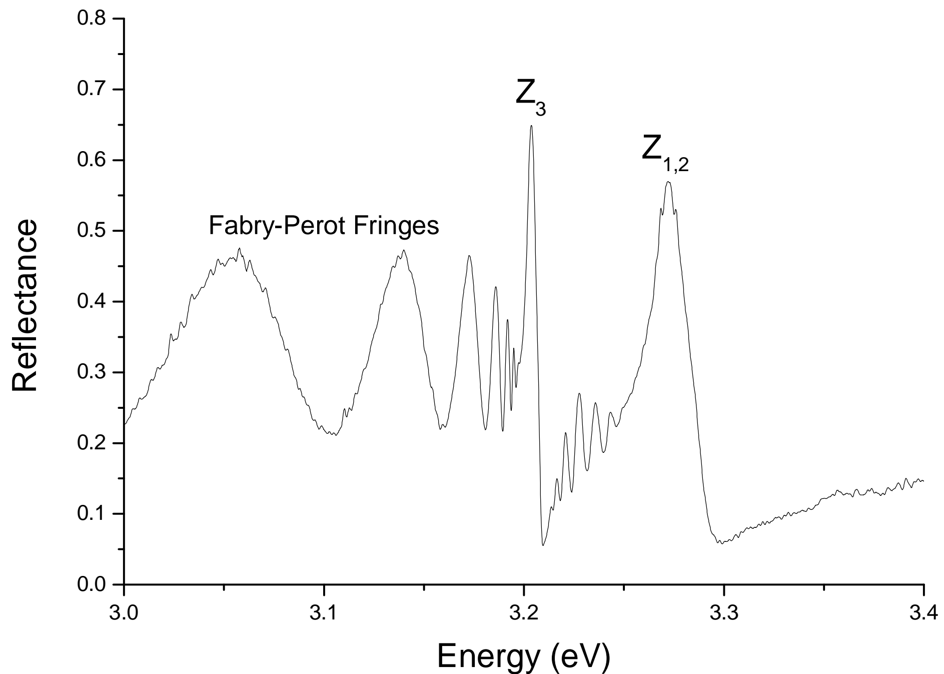

Figure 5.10 *Reflectance spectrum for an undoped CuCl 500nm sample*

closely matches previous results of 3.205 eV and 3.272 eV which were obtained on bulk samples of single crystal CuCl [119].

Reflectance scans were performed on the KCl-CuCl samples and compared to our CuCl samples to see if the addition of KCl had any effect on the exciton energies. The KCl-CuCl samples were prepared in a similar method to the CuCl samples and detailed in chapter 2. Although data was taken from across a broad range of the spectrum, data is only shown between 3.15 eV and 3.32 eV, the area of interest for the excitons of CuCl and also to avoid the influence of the strong Si reflection beginning at 3.35 eV and centred at 3.5 eV.

As we can see from figure 5.11, there is no shift in the exciton position between the 2 samples. There is an increase in calculated reflectance intensity in the KCl-CuCl samples of around 0.1 with multiple samples of both CuCl and KCl-CuCl

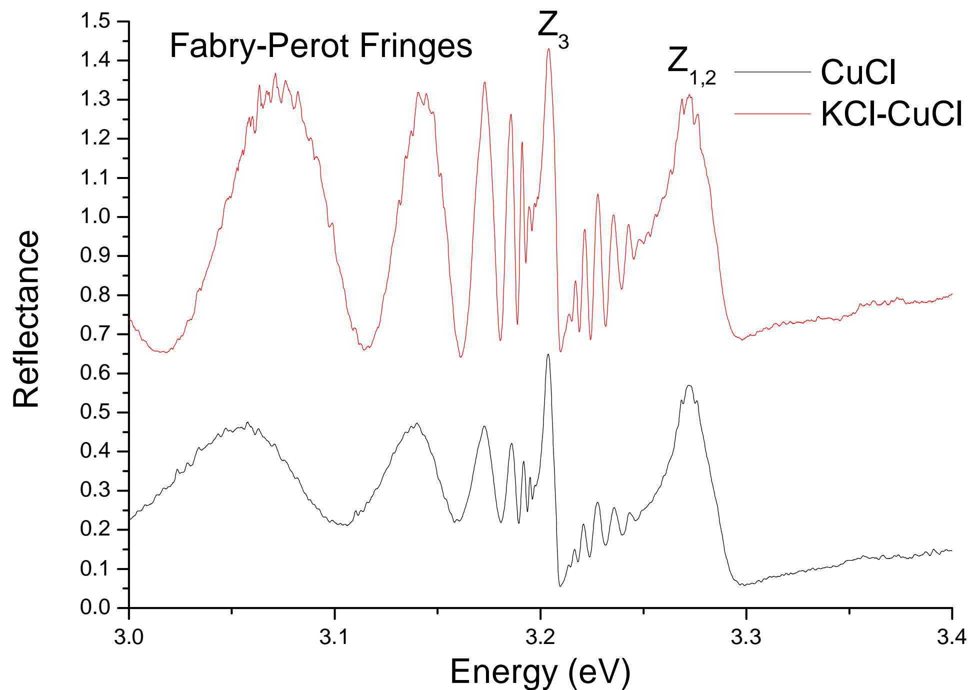

Figure 5.11 *Reflectance spectrum for the KCl-CuCl 500nm sample compared to the CuCl 500nm sample. Scans have been offset by 0.6 for clarity.*

confirming the increased response of these optical properties. Also notable is the increase in the amplitude of the Fabry-Perot fringes observed. The exciton energies compare favourably with previous values recorded for CuCl [119]: Z_3 transverse energy measured ~3.204 eV, compared to the literature value of 3.205 eV and $Z_{1,2}$ transverse energy ~ 3.272 eV, matching the literature value.

Figure 5.12 shows the temperature variance of the $Z_{1,2}$ and Z_3 exciton positions as temperature is increased. The Z_3 temperature dependence appears linear to 180 K before levelling off. The $Z_{1,2}$ exciton position behaves similarly with a more gradual curve effect present throughout. Unlike the PL samples, both peaks remain distinguishable up to room temperature but once temperature levels increase above 120 K features such as the Fabry-Perot fringes are lost to background noise. We can see from the region measurable in both techniques that the variance in the Z_3 exciton value is minimal.

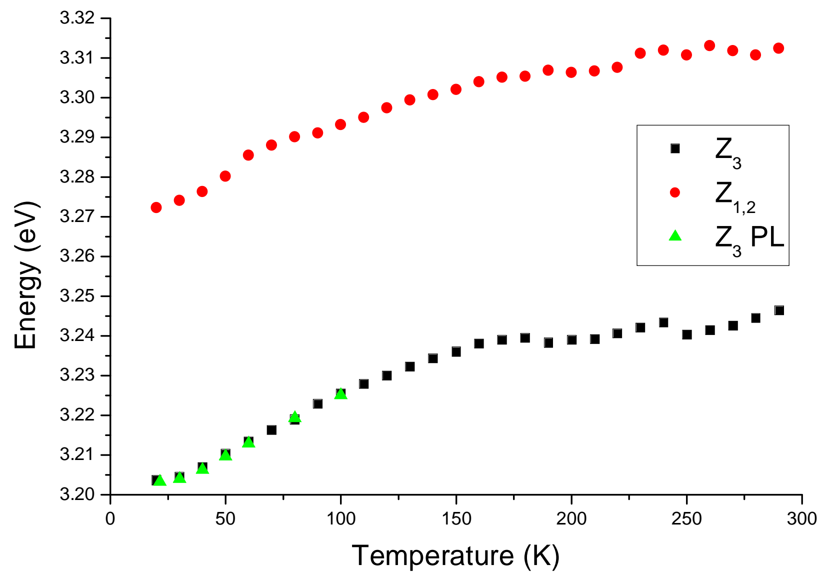

Figure 5.12 *Temperature variance of the $Z_{1,2}$ and Z_3 exciton positions for 500 nm thin film CuCl samples. Also included are the previously measured values for the Z_3 position obtained from PL discussed earlier in this chapter*

5.3.2 Oxygen Doping of CuCl and KCl-CuCl

The main effect produced by the oxygen doping, is a deterioration of the optical properties of the material. The shape of the exciton peaks themselves are increasingly deteriorated as each run of doping takes place. This also causes a slight shift in the position of the exciton peaks themselves, and they occur at lower energies. This can be seen from figure 5.13 for the $Z_{1,2}$ exciton peak and figure 5.14 for the Z_3 exciton peak positions. Whilst the shift of only 5 meV for the $Z_{1,2}$ and 3 meV for the Z_3 might call this assertion into question, the resolution of the equipment is ~0.4 meV and multiple scans have shown the accurate repeatability of the peak locations for unmodified samples. The gradual shift of these peaks and erosion of the distinctive shape of the reflectance spectra is shown in figure 5.15. A gradual reduction in each of

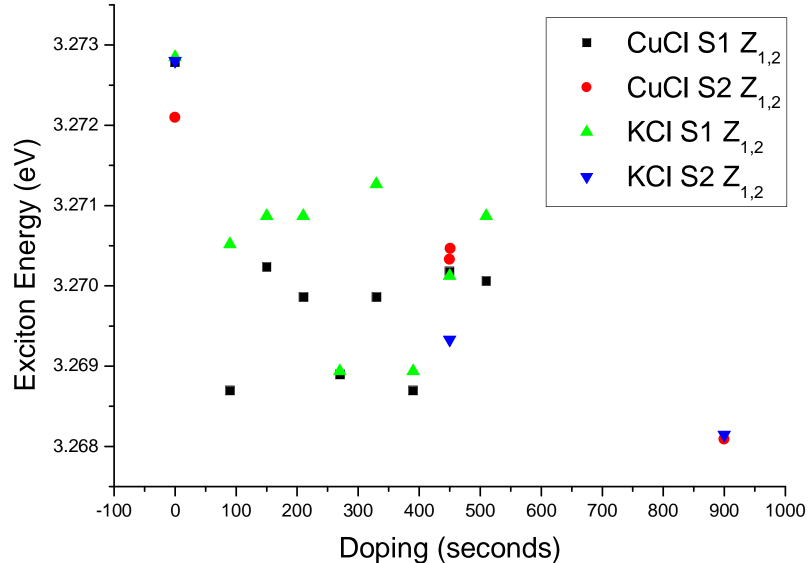

Figure 5.13 *Variance of the $Z_{1,2}$ exciton position in both CuCl and KCl-CuCl samples as oxygen doping levels are increased. As in previous graphs, S1 and S2 refer to separate series of doping tests, S1 consisted of 90 second doping runs and S2 450 second*

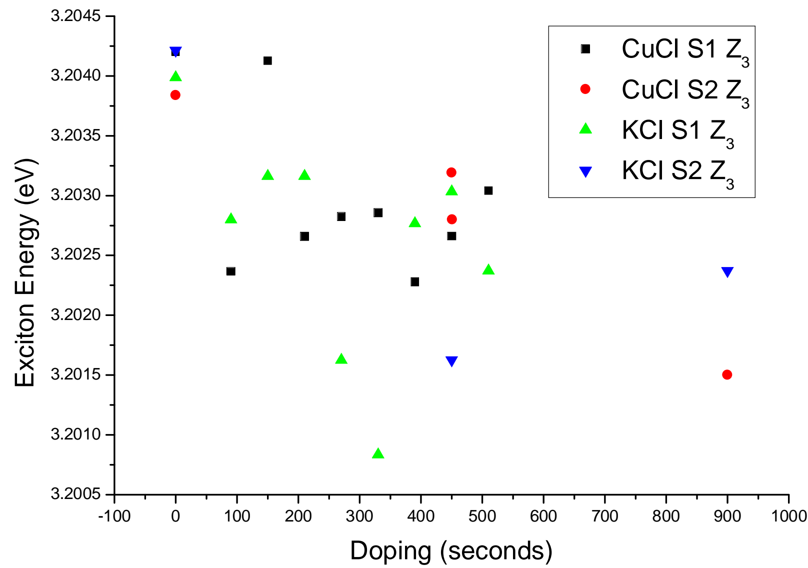

Figure 5.14 *Variance of the Z_3 exciton position as oxygen doping levels are increased for both CuCl and KCl-CuCl thin film samples As in previous graphs, S1 and S2 refer to separate series of doping tests, S1 consisted of 90 second doping runs and S2 450 second*

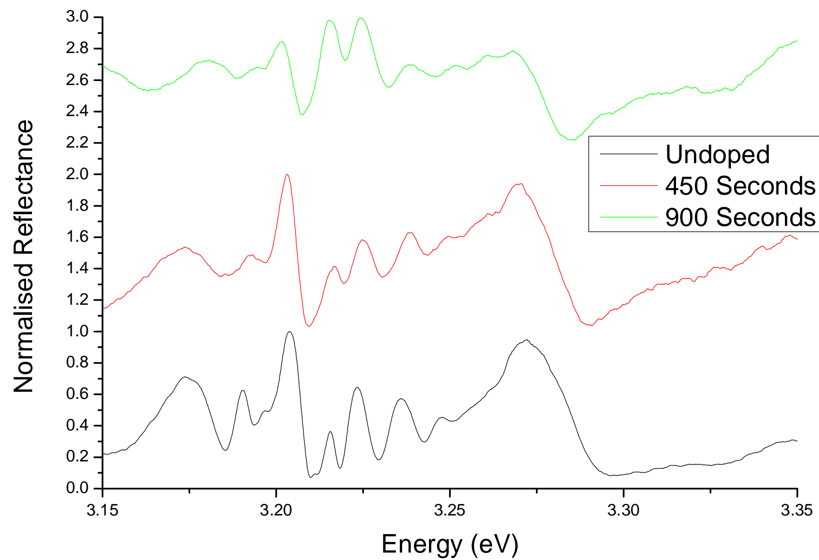

Figure 5.15 *Reflectance spectra of the 450 second doping series. Samples have been normalised to the peak of maximum intensity to show highlight the change in spectra shape and exciton position as doping is increased*

the features can be seen, with the Fabry-Perot peak structure retaining a higher level of intensity after 900 seconds of oxygen doping.

This assertion is also demonstrated by figure 5.16 where we can see the gradual decrease of the reflected intensity at the exciton positions as doping is increased. Previously an ideal doping level was discussed, being somewhere between 2-4 minutes. These graphs further enforce this idea as whilst there is an immediate reduction in the optical quality once doping commences, the exciton peak positions stay relatively unchanged within this region and the exciton reflectance intensity remains above the lowest levels. In fact an increase is recorded within this region for the CuCl samples but not the KCl samples. This matches the increase observed in our PL scans where a similar increase was recorded for CuCl at higher doping levels but not for the KCl-CuCl samples. As in this previous case, it appears to point to the K^+ atoms blocking the influence of the oxygen doping on the optical properties of the material.

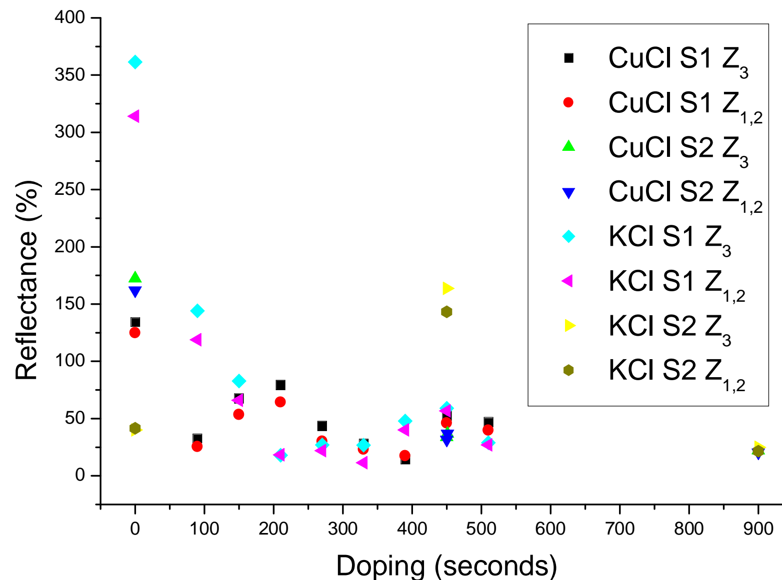

Figure 5.16 *The reflectance percentage as the oxygen doping levels are increased for the Z_3 and $Z_{1,2}$ exciton peaks in both CuCl and KCl-CuCl thin film samples*

5.4 Reflectance Modelling

5.4.1 Introduction

The classical theory of exciton-polariton coupling given by Hopfield and Thomas [120] was used to model the reflectance data in MATLAB [121]. Each of the experimental scans was performed at near normal incidence to minimize the influence of longitudinal exciton bands and allow our spectra to be modelled using a coupled two-exciton band model for the CuCl Z_1 and Z_3 exciton bands. These models combine Maxwell's boundary conditions with a form of additional boundary conditions (ABCs). There are various possible ABCs reported but the 'Pekar ABC' has proved adequate for modelling our spectra. This specifies that the total polarization due to each exciton branch disappears at the crystal interface or at a finite distance from the interface which gives rise to an exciton dead layer, as detailed elsewhere [122]. Exciton-polariton mixed excitation modes are present within the crystal due to photon and free exciton coupling. This affects the refractive index close to the exciton energies and can thus be probed by reflection.

Two modes propagating within the material means three boundary conditions are needed, due to the reflected field and fields due to each of each these modes as seen in figure 5.17 (a). Maxwell's equations give two boundary conditions so another is needed. Pekar ABCs are used for this, which require that the polarization due to a particular exciton band vanish at a certain location in the crystal, usually at the surface or close to the surface, with the physical meaning that the exciton cannot leave the material. For two exciton band material, such as CuCl with the Z_3 and $Z_{1,2}$ exciton bands, the situation is more complex. Three propagating modes are present, with four boundary conditions required as shown in figure 5.17 (b). Another ABC is required.

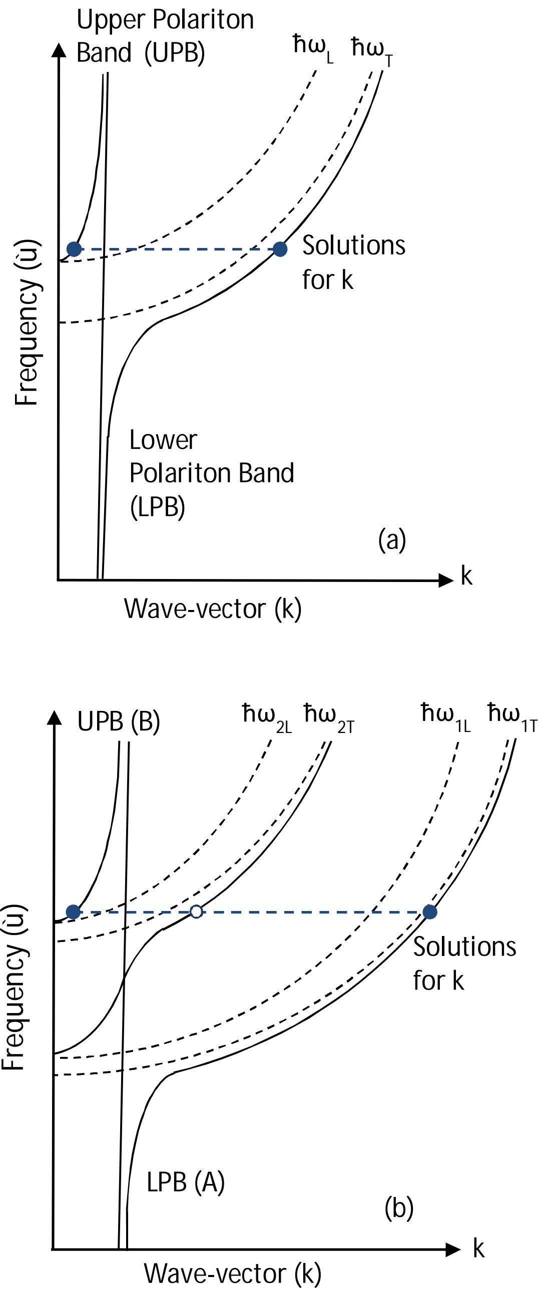

***Figure 5.17** (a) Illustration of the frequency versus the positive real part of the wave-vector for longitudinal and transverse waves. This shows the 2 modes propagating through the film as solutions are valid only along each of the polariton bands shown (b) The same illustration but with an additional propagating mode showing the additional boundary conditions required*

Pekar ABCs are used for both exciton polarizations. Each of these modes will be labelled by the subscripts in the modelling description following this section.

The polarizabilities of the following form characterize insulating crystals for a given wave vector k and frequency ω:

$$\alpha(\omega, k) = \sum \frac{\alpha_{0j}\omega_{jT}^2}{\omega_{jT}^2 - \omega^2 + \beta_j k^2 - i\omega\,\Gamma_j}$$

Eqn 5.2

where α_{0j} are the polarizabilities of each exciton resonance j at $\omega = 0$ and $k = 0$, ω_{jT} the transverse resonance frequencies at $k = 0$, and Γ_j the empirical damping constants. The influence of spatial dispersion is described by:

$$\beta_j k^2 = \left(\frac{\hbar\omega_{jT}}{M_j}\right) k^2$$

Eqn 5.3

where M_j is the effective exciton mass of j and $\hbar$ is Planck's constant divided by 2π.

The frequencies under examination in this thesis occur near two exciton resonances, Z_3 and $Z_{1,2}$. The sum of all these oscillators gives the wave-vector independent background polarizability α_∞:

$$\alpha(\omega, k) = \alpha_\infty + \frac{\alpha_{0A}\omega_{AT}^2}{\omega_{AT}^2 - \omega^2 + \beta_A k^2 - i\omega\,\Gamma_A} + \frac{\alpha_{0A}\omega_{BT}^2}{\omega_{BT}^2 - \omega^2 + \beta_B k^2 - i\omega\Gamma_B}$$

Eqn 5.4

The relation $\varepsilon\varepsilon_0 E = \varepsilon_0 E + \alpha E$ between the electric field E existing in the crystal, the permittivity of the vacuum ε_0, the polarizability α, and the dielectric function ε leads to

$$\varepsilon(\omega, k) = \varepsilon_\infty + \frac{\alpha_{0A}}{\varepsilon_0}\frac{\omega_{AT}^2}{\omega_{AT}^2 - \omega^2 + \beta_A k^2 - i\omega\Gamma_A} + \frac{\alpha_{0B}}{\varepsilon_0}\frac{\omega_{BT}^2}{\omega_{BT}^2 - \omega^2 + \beta_B k^2 - i\omega\Gamma_B}$$

Eqn 5.5

where ε_{∞} is a frequency and wave-vector independent background dielectric constant ($\varepsilon = \varepsilon_0$ for $\omega \to \infty$).

The transverse solution of Maxwell's equation is:

$$\varepsilon(\omega, k) = \frac{k^2c^2}{\omega^2}$$

$$\frac{k^2c^2}{\omega^2} = \varepsilon_r \mu_r$$

Eqn 5.6

This shows the change from the vector to the tensor notation used in the above discussion. Substituting equation 5.5 for the dielectric constant into equation 5.6 and assuming the magnetic permeability of the crystal is that of free space (i.e. the relative permeability $\mu_r = 1$) the transverse solution becomes:

$$\frac{k^2c^2}{\omega^2} = \varepsilon_{\infty} + \frac{1}{\varepsilon_0}\left(\frac{(\alpha_0 + \beta k^2)\omega_0^2}{\omega_0^2 + \beta k^2 - \omega^2 - i\omega\Gamma}\right)$$

Eqn 5.7

When we include both the A and B excitonic resonators, one can simply sum their polarizabilities:

$$\frac{k^2c^2}{\omega^2} = \varepsilon_{\infty} + \frac{\alpha_{A0}}{\varepsilon_0}\left(\frac{\omega_{AT}^2}{\omega_{AT}^2 + \beta_A k^2 - \omega^2 - i\omega\Gamma_{\mathrm{A}}}\right) + \frac{\alpha_{B0}}{\varepsilon_0}\left(\frac{\omega_{BT}^2}{\omega_{BT}^2 + \beta_B k^2 - \omega^2 - i\omega\Gamma_{\mathrm{B}}}\right)$$

Eqn 5.8

where α_{A0} is the static polarizability for the *A* exciton, α_{B0} is the static polarizability for the *B* exciton, ω_{AT} and ω_{BT} are the transverse frequencies of the *A* and *B* excitons respectively, and Γ_{A} and Γ_{B} are the damping coefficients. In each case the parameters refer only to the transverse modes since these propagate at normal angles of incidence. The β parameter will be different for both the A and B excitons because it is related to the transverse frequency and the effective mass of the exciton. To simplify this, equation 5.8 can be expressed as:

$$Ak^2 = \varepsilon_\infty + \frac{B}{C + \beta_A k^2} + \frac{D}{E + \beta_B k^2}$$

Eqn 5.9

where we define A-E as:

$$A = \frac{c^2}{\omega^2}$$

$$B = \frac{\alpha_{A0}}{\varepsilon_0}\omega_{AT}^2$$

$$C = \frac{\varepsilon_0 B}{\alpha_{A0}} - \omega^2 - i\omega\Gamma_{\mathrm{A}}$$

$$D = \frac{\alpha_{B0}}{\varepsilon_0}\omega_{BT}^2$$

$$E = \frac{\varepsilon_0 D}{\alpha_{B0}} - \omega^2 - i\omega\Gamma_{\mathrm{B}}$$

Eqns 5.10

Multiplying by the denominators on the RHS, equation 5.9 becomes

$$Ak^2(C + \beta_A k^2)(E + \beta_B k^2) =$$

$$\varepsilon_\infty(C + \beta_A k^2)(E + \beta_B k^2) + B(E + \beta_B k^2) + D(C + \beta_A k^2)$$

Eqn 5.11

and after multiplying the out the bracketed parameters and collecting terms one obtains the expression:

$$(A\beta_A\beta_B)k^6 + (AC\beta_B + AE\beta_B - \varepsilon_\infty\beta_A\beta_B)k^4 + (ACE - \varepsilon_\infty C\beta_B - \varepsilon_\infty C\beta_A - B\beta -$$

$$D\beta)k^2 - (\varepsilon_\infty CE + BE + DC) = 0$$

Eqn 5.12

This, when re-arranged, leads to an equation cubic in k^2 for each value of ω, and thus for each optical frequency there are 3 different modes, with three different k values, which we denote by subscripts (k_i). These k values may be complex and the sign of the k value used (i.e. the positive or negative solution of $\sqrt{k^2}$) is chosen to

confirm with physically meaningful boundary conditions (e.g. a solution vanishing far from a boundary or the correct direction of energy transfer). Each of these propagating modes has an associated refractive index, n_i, given by $n_i = \omega / k_i$. To solve for reflectance and transmission at various different optical frequencies we need to use a matrix approach.

In doing so, we have modelled four of the different scenarios possible using different combinations of dead layers treating the thin layer sample as a bulk sample before including the thickness of the material and dead layers at the interfaces (figure

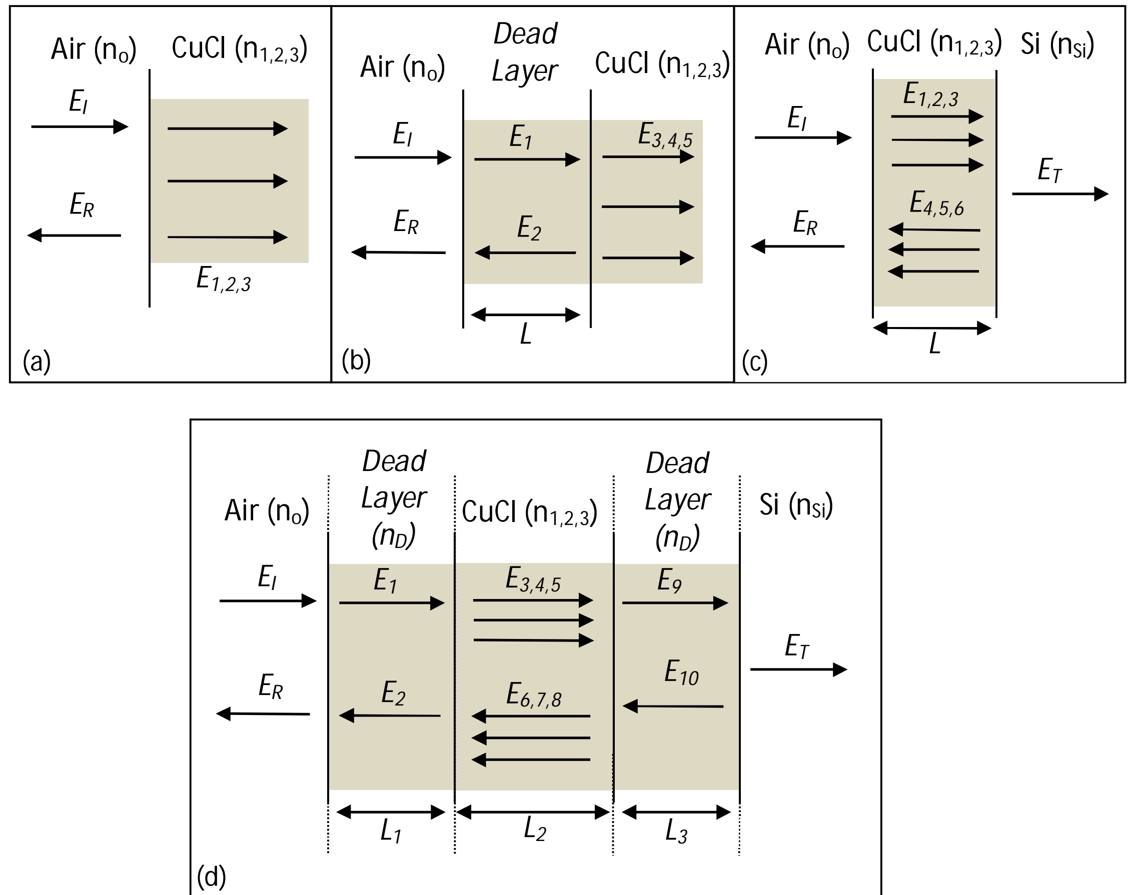

Figure 5.18 *Photon and polariton modes for (a) Model 1 (b) Model 2 (c) Model 3 and (d) Model 4. Electric field amplitudes are labelled Ei. Layer thicknesses are labelled* L_i *and refractive indices as* n_i

5.18). Model 1 applies Pekar's ABC at the air-CuCl interface and presumes a sample of bulk CuCl. Model 2 applies the same ABC properties at the air-CuCl interface and includes the dead layer thickness at the air-CuCl interface as a fitting parameter, applying Pekar's ABC at the dead layer boundary. Model 3 applies the same ABC properties at the air-CuCl interface and includes additional parameters for the thickness of the thin film layer and the reflection at the Si substrate beneath but with dead layers remaining absent. Model 4 is similar to model 3 considering the thin film to have a defined thickness with the addition of dead layers at the air-CuCl and CuCl-Si boundaries.

The equations and theory behind each of these models will now be discussed. Since each of the models has a similar underlying structure, they will be described in order with each model building upon the previous.

5.4.2 Model 1 (Air – Bulk CuCl)

When Maxwell's equations are combined with the ABC Pekar boundary conditions we are left with the following series of simultaneous equations for the boundary conditions

$$E_1 + E_R = E_1 + E_2 + E_3 \qquad \textit{Eqn 5.13}$$

$$n_0 E_1 - n_0 E_R = n_1 E_1 + n_2 E_2 + n_3 E_3 \qquad \textit{Eqn 5.14}$$

$$\alpha_A(k_1,\omega)E_1 + \alpha_A(k_2,\omega)E_2 + \alpha_A(k_3,\omega)E_3 = 0 \qquad \textit{Eqn 5.15}$$

$$\alpha_B(k_1,\omega)E_1 + \alpha_B(k_2,\omega)E_2 + \alpha_B(k_3,\omega)E_3 = 0 \qquad \textit{Eqn 5.16}$$

where n_i represents the refractive index n_1, n_2 and n_3 and $\alpha(k,\omega)$ is the polarizability of the *A* or *B* free excitons as a function of frequency for each of the three solutions for the wavevector $k_{1,2,3}$. Equations 5.13 and 5.14 above correspond to the boundary

conditions from Maxwell's equations and equations 5.15 and 5.16 to the Pekar ABCs for the A and B exciton bands, respectively, showing that the polarization due to each exciton vanishes, in this case at the surface. Equation 5.13 is represented visually in figure 5.18 (a). The polarizability $\alpha(k,\omega)$ is defined as:

$$\alpha_A(k_{1-3},\omega) = \varepsilon_0(\varepsilon_\infty - 1) + \frac{\alpha_{A0}\omega_{AT}^2}{\omega_{AT}^2 + \beta_A k_{1-3}^2 - \omega^2 - i\omega\Gamma_A}$$

Eqn 5.17

for *A* excitons with a similar expression for *B* excitons. ε_∞ is the static background dielectric constant, α_{A0} is the static exciton polarizability, ω is the angular frequency of the incident radiation, ω_{AT} is the transverse exciton frequency, Γ_A is the wavevector-independent damping parameter of the *A* exciton and k is the wavevector. The β parameter can be expressed in terms of the exciton effective mass as follows [123]:

$$\beta_A = \frac{\eta\omega_{AT}}{m_A^*}$$

Eqn 5.18

where m^* is the effective mass (in the case above for the A exciton band). This also has a similar expression for *B* excitons, with separate values for the effective mass being used to distinguish the $Z_{1,2}$ and Z_3 excitons. The above boundary conditions can be expressed in the matrix form:

$$\begin{pmatrix} -1 & 1 & 1 & 1 \\ 1 & n_1 & n_2 & n_3 \\ 0 & \alpha_{A1} & \alpha_{A2} & \alpha_{A3} \\ 0 & \alpha_{B1} & \alpha_{B2} & \alpha_{B3} \end{pmatrix} \begin{pmatrix} r \\ A \\ B \\ C \end{pmatrix} = \begin{pmatrix} 1 \\ 1 \\ 0 \\ 0 \end{pmatrix}$$

Eqn 5.19

where each of the relative field intensities are defined as $r = E_R/E_I$, $A = E_1/E_I$, $B = E_2/E_I$ and $C = E_3/E_I$. α_{A1-3} are the frequency dependant polarizabilities defined in equation (5) for the *A* free excitons with wavevectors k_{1-3} and α_{B1-3} are the corresponding frequency dependant polarizabilities for the *B* free excitons with wavevectors k_{1-3}. The refractive index of air has been set to unity for this model and

throughout the rest of the analysis. $n_{1\text{-}3}$ represents the refractive index for each of the $E_{1\text{-}3}$ modes. The matrix above takes the form $Xy=z$. This means by taking the inverse of the square matrix Z we can solve for the reflection coefficient r, i.e. $y=X^{-1}z$ so $y(1)$ gives us r. Squaring this gives us the reflectance R. The A, B and C values provide the relative interface field amplitudes and phases for the propagating polariton modes within the structure. These and later matrix operations were performed using MATLAB.

5.4.3 Model 2 (Air – DL – CuCl)

For this model we apply an additional dead layer to the theory of model 1. The thickness of this layer is denoted by the fitting parameter L resulting in the following solvable matrix set:

$$\begin{pmatrix} r \\ A \\ B \\ C \\ D \\ E \end{pmatrix} = \begin{pmatrix} -1 & 1 & 1 & 0 & 0 & 0 \\ 1 & n_D & -n_D & 0 & 0 & 0 \\ 0 & e & e_* & -1 & -1 & -1 \\ 0 & n_D e & -n_D e_* & -n_1 & -n_2 & -n_3 \\ 0 & 0 & 0 & \alpha_{A1} & \alpha_{A2} & \alpha_{A3} \\ 0 & 0 & 0 & \alpha_{B1} & \alpha_{B2} & \alpha_{B3} \end{pmatrix}^{-1} \begin{pmatrix} 1 \\ 1 \\ 0 \\ 0 \\ 0 \\ 0 \end{pmatrix} \qquad \textit{Eqn 5.20}$$

where e represents $exp\left(i\frac{n_D\omega L}{c}\right)$ and e_* represents $exp\left(-i\frac{n_D\omega L}{c}\right)$. n_D represents the dead layer refractive index defined as $n_D = \sqrt{\varepsilon_\infty}$. The equation is solved for r and then squared to obtain the reflectance.

5.4.4 Model 3 (Air – CuCl – Si)

For the third model, each of the parameters of the first model are included with the addition of the thin film nature of the sample and reflection from the CuCl/Si interface. The thickness is denoted by L and used as an additional fitting parameter.

These additional parameters require the use of further boundary conditions. These are applied at each of the interfaces and state that the polarization due to the excitons must be zero at the air-CuCl and CuCl-Si interfaces as we are not taking the dead layers into account in this model. The two resonances obtained for the *A* and *B* excitons at the air-CuCl interface are:

$$\alpha_{0A}(k_1,\omega)[E_1 + E_4] + \alpha_{0A}(k_2,\omega)[E_2 + E_5] + \alpha_{0A}(k_3,\omega)[E_3 + E_6] = 0 \qquad \textit{Eqn 5.21}$$

with α_{0A} representing the polarizability factor for the *A* exciton and changing to α_{0B} for the *B* exciton resonance equation below:

$$\alpha_{0B}(k_1,\omega)[E_1 + E_4] + \alpha_{0B}(k_2,\omega)[E_2 + E_5] + \alpha_0(k_3,\omega)[E_3 + E_6] = 0 \qquad \textit{Eqn 5.22}$$

Similarly at the CuCl-Si interface the additional boundary conditions obtained are:

$$\alpha_{0A}(k_1,\omega)\left[E_1 e^{i(n_1\omega L/c)} + E_4 e^{-i(n_1\omega L/c)}\right] +$$

$$\alpha_{0A}(k_1,\omega)\left[E_2 e^{i(n_2\omega L/c)} + E_5 e^{-i(n_2\omega L/c)}\right] +$$

$$\alpha_{0A}(k_1,\omega)\left[E_3 e^{i(n_3\omega L/c)} + E_6 e^{-i(n_3\omega L/c)}\right] = 0$$

Eqns 5.23

for the A exciton. The additional B exciton boundary conditions are similar and given by:

$$\alpha_{0B}(k_1,\omega)\left[E_1 e^{i(n_1\omega L/c)} + E_4 e^{-i(n_1\omega L/c)}\right] +$$

$$\alpha_{0B}(k_1,\omega)\left[E_2 e^{i(n_2\omega L/c)} + E_5 e^{-i(n_2\omega L/c)}\right] +$$

$$\alpha_{0B}(k_1,\omega)\left[E_3 e^{i(n_3\omega L/c)} + E_6 e^{-i(n_3\omega L/c)}\right] = 0$$

Eqns 5.24

The additional *E* values are added to our existing boundary conditions given in equation 5.13 – 5.16 and expressed in the matrix form. The solvable $b=A^{-1}c$ format is:

$$\begin{pmatrix} r \\ A \\ B \\ C \\ D \\ E \\ F \\ G \end{pmatrix} =$$

$$\begin{pmatrix} -1 & 1 & 1 & 1 & 1 & 1 & 1 & 0 \\ 1 & n_1 & n_2 & n_3 & -n_1 & -n_2 & -n_3 & 0 \\ 0 & e_1 & e_2 & e_3 & e_{*1} & e_{*2} & e_{*3} & -1 \\ 0 & n_1 e_1 & n_2 e_2 & n_3 e_3 & -n_1 e_{*1} & -n_2 e_{*2} & -n_3 e_{*3} & -n_{Si} \\ 0 & \alpha_{A1} & \alpha_{A2} & \alpha_{A3} & \alpha_{A1} & \alpha_{A2} & \alpha_{A3} & 0 \\ 0 & \alpha_{B1} & \alpha_{B2} & \alpha_{B3} & \alpha_{B1} & \alpha_{B2} & \alpha_{B3} & 0 \\ 0 & \alpha_{A1} e_1 & \alpha_{A2} e_2 & \alpha_{A3} e_3 & \alpha_{A1} e_{*1} & \alpha_{A2} e_{*2} & \alpha_{A3} e_{*3} & 0 \\ 0 & \alpha_{B1} e_1 & \alpha_{B2} e_2 & \alpha_{B3} e_3 & \alpha_{B1} e_{*1} & \alpha_{B2} e_{*2} & \alpha_{B3} e_{*3} & 0 \end{pmatrix}^{-1} \begin{pmatrix} 1 \\ 1 \\ 0 \\ 0 \\ 0 \\ 0 \\ 0 \\ 0 \end{pmatrix}$$

Eqn 5.25

where $e_i = exp\left(i\frac{n_i \omega L}{c}\right)$ and $e_{*i} = exp\left(-i\frac{n_i \omega L}{c}\right)$ and n_{Si} represents the refractive index of silicon which at 3.2 eV is ~5.5 [15]. As before this equation is solved for the amplitude reflection coefficient r which is then squared to obtain the reflectance.

5.4.5 Model 4 (Air – DL – CuCl – DL – Si)

For the fourth model we include the Si interface theory of the second model with the addition of exciton dead layers (DL) at the air/CuCl and CuCl/Si interfaces. Each of these dead layers are given fitting parameters of L_1 and L_3 respectively with the thickness of the CuCl layer represented by L_2 (figure 5.18 (d)). The boundary conditions of the dead layers are added onto the previous matrix resulting and rearranged to give:

$$
\begin{pmatrix} r \\ A \\ B \\ C \\ D \\ E \\ F \\ G \\ H \\ I \\ J \\ K \end{pmatrix}
=
\begin{pmatrix}
-1 & 1 & 1 & 0 & 0 & 0 & 0 & 0 & 0 & 0 & 0 & 0 \\
1 & n_D & -n_D & 0 & 0 & 0 & 0 & 0 & 0 & 0 & 0 & 0 \\
0 & -e_{D1} & -e_{*D1} & 1 & 1 & 1 & 1 & 1 & 1 & 0 & 0 & 0 \\
0 & -n_D e_{D1} & n_D e_{*D1} & n_1 & n_2 & n_3 & n_1 & n_2 & n_3 & 0 & 0 & 0 \\
0 & 0 & 0 & e_{12} & e_{22} & e_{32} & e_{*12} & e_{*22} & e_{*32} & -1 & -1 & 0 \\
0 & 0 & 0 & n_1 e_{12} & n_2 e_{22} & n_3 e_{32} & n_1 e_{*12} & n_2 e_{*22} & n_3 e_{*32} & -n_D & n_D & 0 \\
0 & 0 & 0 & 0 & 0 & 0 & 0 & 0 & 0 & e_{D3} & e_{*D3} & -1 \\
0 & 0 & 0 & 0 & 0 & 0 & 0 & 0 & 0 & n_D e_{D3} & -n_D e_{*D3} & -n_{Si} \\
0 & 0 & 0 & \alpha_{A1} & \alpha_{A2} & \alpha_{A3} & \alpha_{A1} & \alpha_{A2} & \alpha_{A3} & 0 & 0 & 0 \\
0 & 0 & 0 & \alpha_{B1} & \alpha_{B2} & \alpha_{B3} & \alpha_{B1} & \alpha_{B2} & \alpha_{B3} & 0 & 0 & 0 \\
0 & 0 & 0 & \alpha_{A1} e_{12} & \alpha_{A2} e_{22} & \alpha_{A3} e_{32} & \alpha_{A1} e_{12} & \alpha_{A2} e_{22} & \alpha_{A3} e_{32} & 0 & 0 & 0 \\
0 & 0 & 0 & \alpha_{B1} e_{12} & \alpha_{B2} e_{22} & \alpha_{B3} e_{32} & \alpha_{B1} e_{12} & \alpha_{B2} e_{22} & \alpha_{B3} e_{32} & 0 & 0 & 0
\end{pmatrix}^{-1}
\begin{pmatrix} 1 \\ 1 \\ 0 \\ 0 \\ 0 \\ 0 \\ 0 \\ 0 \\ 0 \\ 0 \\ 0 \\ 0 \end{pmatrix}
$$

Eqn 5.26

where e_{ij} represents $exp\left(i\frac{n_i \omega L_j}{c}\right)$ with n_i representing the refractive indices as in previous models, with the addition of $n_D = \sqrt{\varepsilon_\infty}$ for the dead layers. L_j represents the lengths L_1, L_3 and L_2 for the two dead layers at each of the interfaces and the CuCl thin layer thickness respectively. Similar to model 2, e_{*ij} represents $exp\left(-i\frac{n_i \omega L_j}{c}\right)$. As in each of the previous models, the equation is solved for the amplitude coefficient r and squared to give the reflectance.

5.4.6 Modelling Results

To aid the fitting procedure, initial values are taken from the experimental data for the transverse and longitudinal frequencies of the excitons *A* and *B* which can be estimated from the maximum and minimum reflectivity at the expected spectral regions. The static background dielectric constant can be estimated from the average reflection coefficient far from the areas of interest. By varying parameters such as the *A* and *B* longitudinal and transverse exciton energies, the damping coefficient, exciton mass, thin film CuCl thickness for models 3 and 4 and in the case of models 2 and 4 the dead layer thickness, the fitted reflectance spectra is optimized to the experimental data using a least squares procedure. For this we have used MATLAB [121].

Figure 5.19 shows the experimental reflectance data plotted alongside the best fits for each of the models used of that data. We can see that each of the models quite closely matches the experimental data for the Z_3 exciton with models 3 and 4 being slightly closer to the measured experimental values for the Z_3 exciton (3.202 eV) and the $Z_{1,2}$ exciton (3.272 eV). This figure also displays the Fabry-Perot oscillations present throughout the spectra as the distance from the exciton positions is increased. Figure 5.20 shows the calculated exciton-polariton dispersion curve for CuCl overlaid on top of the dispersion curve obtained by previous work [23]. This previous report also calculated the three-branch CuCl dispersion curve using a two-oscillator model, one for each of the excitons Z_3 and $Z_{1,2}$. The regions above and below the central exciton position have a high Fabry-Perot fringe presence, with the central line indicating probable Fabry-Perot oscillations between the two exciton peaks as well. We can see the shape of our curve matches that from the previous work excellently, with only slight differences due to a small difference in the calculated energy position of the $Z_{1,2}$ exciton for our model. In fact, the agreement is so close that it is hard to

distinguish between our data and that of reference [23] over large regions of the dispersion curves. The comparison of our modelled thin film values and those obtained for bulk CuCl are shown in table 5.1 and discussed therein.

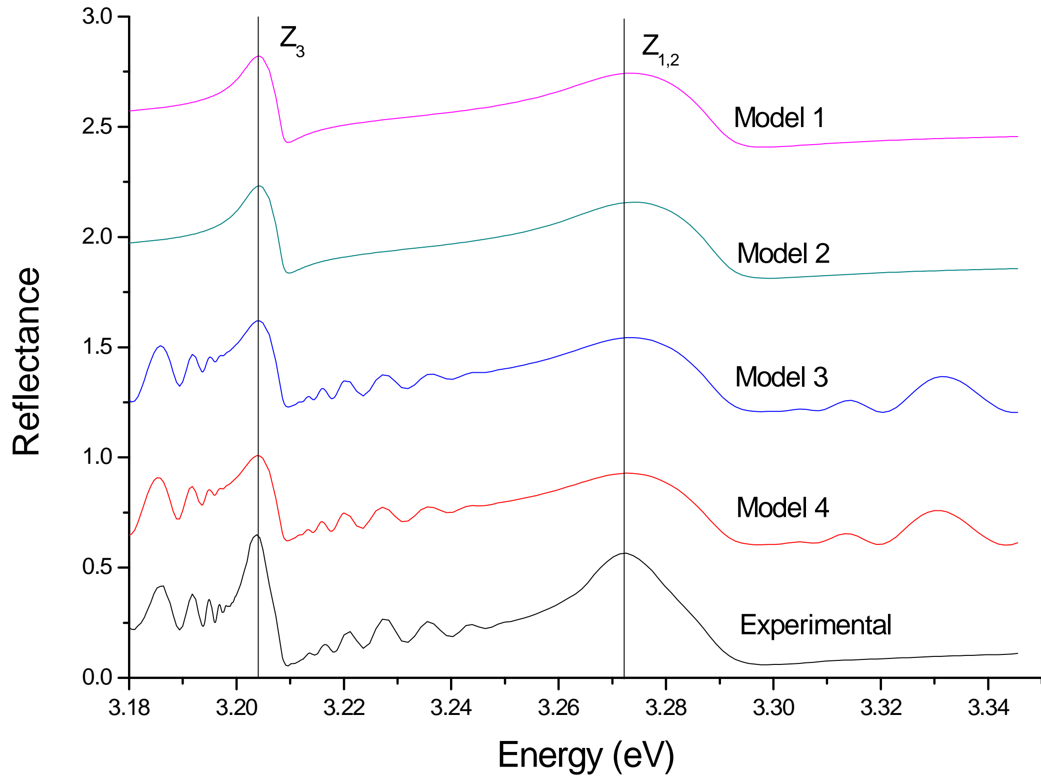

Figure 5.19 *Experimental reflectance plotted against each of the reflectance models. Spectra have been offset by 0.6 each for clarity and the position of the* Z_3 *and* $Z_{1,2}$ *excitons shown. The CuCl thin film is shown at its recorded intensity level. The included interface layers of each model are as follows: Model 1: Air - Bulk CuCl; Model 2: Air – Dead layer – Bulk CuCl; Model 3: Air – Thin film CuCl – Si substrate; Model 4: Air – Dead layer – Thin film CuCl – Dead layer – Si substrate*

The Fabry-Perot oscillations will be observed when the spatial damping of the propagating modes is sufficiently small that the modes can make at least two passes through the sample. This also requires the sample thickness to be significantly less than L, where $L = (n_i\ k_0)^{-1}$ where n_i is the imaginary part of the mode refractive

index, k_0 the free space wavevector and L the mean free path of an exciton polariton [124]. In the regions around the exciton positions the value of L will be increased to the order of 1 x 10^5 so no fringes should be visible at these positions. Correspondingly as we move away from the exciton positions, the L value will greatly decrease and these fringes will become prominent. This trending is clearly shown in figure 5.11, with the Fabry-Perot fringes increasing in amplitude as the distance from the exciton position is increased. The fringes are blocked from prominence at the higher energy values due to reflection from the Si substrate which produces a broadband reflectance centred on 3.5 eV.

Table 5.1 shows the best-fit values to our data, determined using model 3, alongside previously measured values recorded for bulk CuCl [118]. Sample 1 is the

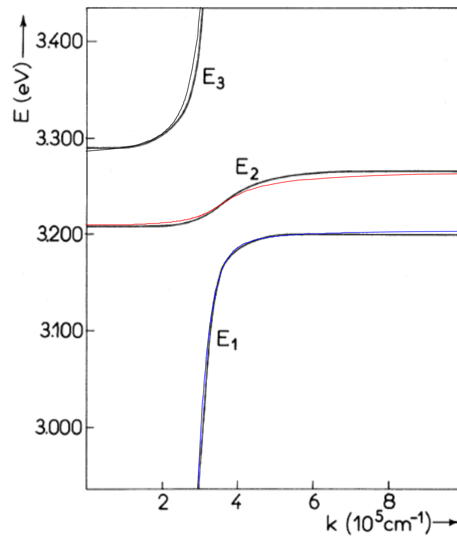

Figure 5.20 *The Computed Polariton Dispersion curves for CuCl. The overlaid blue, red and black lines are the curves produced from our calculations, with the underlying curve previously calculated in literature* [23]. *The agreement is so close that it is hard to distinguish between our data and that of reference* [23] *over large regions of the dispersion curves*

Parameter	Bulk sample [118]	Sample 1	Sample 2	Sample 3
$\hbar\varpi_{AT}$ (transverse Z_3 exciton energy, eV)	3.202	3.203	3.203	3.202
$\hbar\varpi_{BT}$ ($Z_{1,2}$ transverse exciton energy, eV)	3.266	3.267	3.267	3.266
$\hbar\varpi_{AT} - \hbar\varpi_{BT}$ (Z_3-$Z_{1,2}$ splitting, meV)	64	64	64	64
Δ_{LT}^{A} (Z_3 exciton LT splitting, meV)	5.7	5.76	4.54	5.41
Δ_{LT}^{B} ($Z_{1,2}$ exciton LT splitting, meV)	23	23.5	19.1	23.2
$\hbar\Gamma_A$ (Z_3 exciton damping, meV)	0.9	1.6	1.1	1.1
$\hbar\Gamma_B$ ($Z_{1,2}$ exciton damping, meV)	11.5	8.6	9.9	5.8
M_A (multiples of electron mass, Z_3)	2.4	0.36	0.80	0.29
M_B (multiples of electron mass, $Z_{1,2}$)	0.65	0.083	0.15	0.06
DL thickness Z_3 exciton (nm)	1.4	0	0	0
DL thickness $Z_{1,2}$ exciton (nm)	2.8	0	0	0
Film thickness (nm)	N/A	1002.2	746.8	691.1

Table 5.1 *Fitting parameters used for modeling the CuCl thin film samples and the bulk sample from the literature for comparison*

sample used in figure 5.19, with samples 2 and 3 other samples made in the same manner to test the reliability of the modelling process. Each of the constants closely matches the bulk samples except for the effective mass of each of the excitons. The effect of this variable on the shape of the graph is mainly seen in the relative intensity of the exciton peaks, the higher this value, the more asymmetric the peaks will become. From observation of our modeled spectra, there is a slight difference in the peak shape, with our modeled samples being slightly more rounded than the experimental peaks, suggesting that a larger exciton mass is required. However the limits of MATLAB are ± 1.7977e+308 so as the value of the thickness of the thin film is increased, the e_1 and e_2 parameters present in each of the matrices used in models 3 and 4 tends to increase above this limit at lower eV levels and produce an error. Artificially decreasing the exciton masses keeps these variables within the programming limitations but results in inaccuracies in the electron mass value. This allows us to model the Fabry-Perot fringes at lower energies and ensure the thickness value results in accurate fringe production between the two exciton peaks visible in figure 5.19.

The film thickness modeled to be 1000.2 nm would appear to be significantly higher than the deposited nominal 500 nm thin film thickness of the CuCl samples. However a number of factors can serve to inflate the thickness above the 500 nm intended thickness, position of the Si substrates in relation to the evaporation crucible, orientation of the shielding plate to restrict deposition until an ideal rate has been reached and the general non-uniformity of the surface of these samples all contribute to inflation of the CuCl thickness. Another cause could be an error in the calculated tooling factor used in the deposition of the CuCl material itself. Measurements performed in a scanning electron microscope (SEM) in cross-sectional geometry on a

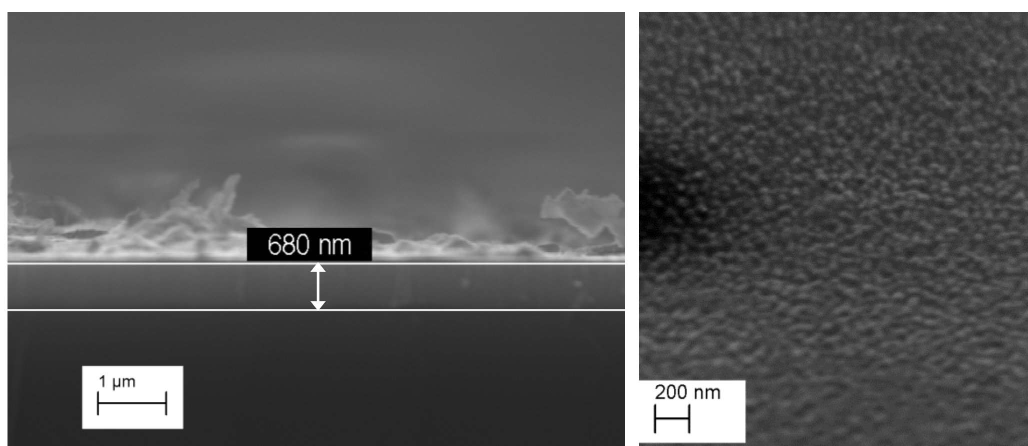

(a) (b)

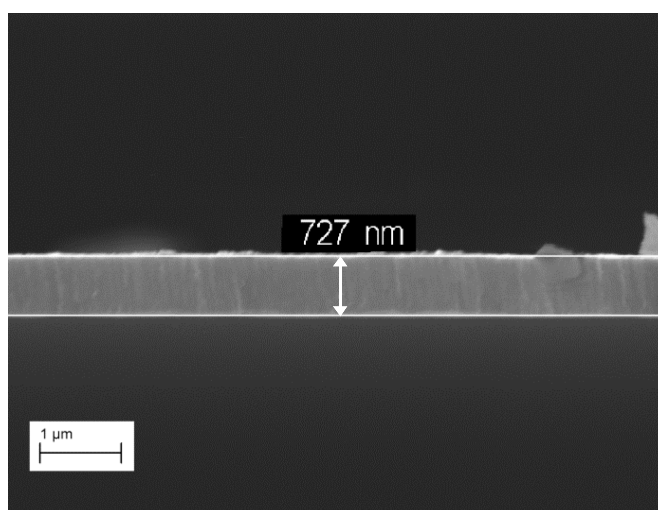

(c)

Figure 5.21 *(a) Cross-sectional of CuCl thin film sample 2 showing the physical thickness. Lines have been slightly shifted for clarity. The debris present on the CuCl surface is due to the cleaving process used to prepare samples for the cross-sectional SEM measurements and not representative of the CuCl sample surface (b) Tilted SEM image of the surface taken at close to 30° of the CuCl thin film sample showing the surface roughness (c) Cross-sectional of CuCl thin film sample 3 showing the physical thickness.*

CuCl thin film on Si revealed the actual layer thickness to be ~ 1080 nm, even though the nominal deposition thickness was 500 nm, thus validating the accuracy of the fitted thickness value for other samples. Further reflectance measurements on samples of actual thicknesses ~ 680 nm (as determined by cross-sectional SEM measurements shown in figure 5.21 (a)) yielded a best fit thickness of 691.1 nm. The cross-sectional image shows the presence of debris on the sample surface. This is mainly due to the cleaving process necessary to produce these images as figure 5.21 (b) shows the surface of the sample to be somewhat uniform. There is a similar good agreement between our modelled thickness and the actual thickness for thin film sample 3, the modelled value being 746.8 and the measured ~ 727 nm, further validating the accuracy of the fitted film thickness parameter (figure 5.21 (c)).

The critical dead layer thickness in bulk CuCl has previously been calculated to be ~1.4 and 2.8 nm for Z_3 and $Z_{1,2}$ excitons respectively and the authors say that above this value the fit of the reflectance spectra is destroyed [118] however this wasn't the case in our model. Dead layer thicknesses below these values have no discernible effect on the modelled spectra, shown by models 2 and 4 in figure 5.19. The dead layer value was set to the calculated values to try and show the effect of the layers and in model 4 a slight flattening of the Z_3 exciton peak can be observed while model 2 has no discernible differences. Increasing the dead layer value causes a decrease in the peak height at each of the exciton positions and a slight change in the location of the Fabry-Perot fringes. The lower values used for the exciton effective masses already cause the peak heights to be decreased, so the model tends to reduce the dead layer thickness to 0 to maintain accuracy at these locations. Using either previously calculated or physically plausible values for the dead layer thickness results in modelled spectra practically identical to that which negates this factor, i.e. model 1

being identical to model 2 and model 3 identical to model 4. The lack of effect of this dead layer is probably due to the excitonic radius for CuCl being 0.7 nm [125, 126] which is very small when compared to other copper halides, thus requiring a large dead layer to produce a notable resonance feature.

Bulk CuCl would be expected to be under minimal strain. It is feasible that any differences in the fitted parameters could be due to strain and stress within the thin film. However, the agreement of the fit values with the bulk values, particularly the LT splitting parameter, shows the lack of strain in the CuCl thin film, probably due to the close lattice matching with the Si substrate underneath [40]. The minor discrepancies in the LT splitting and exciton damping parameters occur for the $Z_{1,2}$ exciton peak which is broader compared to the Z_3 and thus the features are less sharp and so fitting errors will naturally increase.

Due to the close resemblance of the KCl-CuCl reflectance spectra to the CuCl spectra, a significant difference in the fitting parameters would not be expected. Identical parameters can be used for both, with the relatively larger reflectance signal from the KCl-CuCl and a subtle difference in the Fabry-Perot oscillations due to a different film thickness being the only variations. The result is similar for the doped samples of CuCl and KCl-CuCl; deterioration of the exciton peak intensity and shape as doping is increased effects the samples in a uniform manner, reducing the presence of the exciton peak signals and the Fabry-Perot fringes throughout the entire energy range.

This shows us the limitations of the modeling procedure for different types of samples, but for CuCl thin films of varying thickness on different substrates it could prove a valuable tool due to the non-destructive nature of the process. Long-time exposure to the laser used by the PL system leaves a burned or scarred pattern on the

surface and results in reduced PL intensities outputted from the surface. SEM usage results in a similar type of surface scarring produced by the electron beam on the surface of the sample, with the detected signal decreasing and a reduction in the secondary electron output as scanning continues. Even the non-destructive process of XRD causes the deterioration of the CuCl crystal structure due to the scans taking place in an open atmosphere environment and thus failing to inhibit the hygroscopic nature of the material. The reflectance modeling process represents the only truly non-destructive method of characterization utilized in this work which proves invaluable for controlling the natural exposure-related decay of the samples and also allowing different setups to be tested on samples with known properties.

5.5 Summary

This chapter further examined the luminescence properties of CuCl material. The PL characterization of the CuCl thin film samples has been performed, including a variable temperature analysis and a calculation of the exciton binding energies. Comparing the KCl-CuCl PL spectra with the CuCl spectra noted no discernible differences between samples. Analysis of the doped samples of both KCl-CuCl and CuCl showed the formation of an unknown peak at 3.187 eV. This peak production is present only in the CuCl samples, suggesting the K^+ ions added by the KCl salt inhibit the formation of this defect. Similarly the I_1 shoulder measured at 3.182 eV is found to increase in intensity when doped, with the increase present only in the CuCl samples. This is one of the few notable differences between the CuCl and KCl-CuCl samples. Further exploration of this formation could be performed in future works, with samples exhibiting these features in the PL system tested using the previously discussed

methods of characterization for any noticable differences to the previously recorded values.

Analysis of the reflectance spectra for CuCl and KCl-CuCl showed produced another noticable difference between the two materials, an increase in the reflected intensity for KCl-CuCl when compared to the CuCl samples. This also caused an increase in the overall amplitude of the peaks measured at the exciton positions Z_3 and $Z_{1,2}$ and at each of the Fabry-Perot fringe positions. Oxygen doping caused a decrease in the energy values recorded for each of the exciton positions as well as the measured reflectance value for each of the excitons. This decrease was more gradual, reaching a minimum at 270 seconds which when combined with our previous values for the ideal region of doping from chapter 4, suggests doping of 2-3 minutes will retain most of the material's properties whilst having the desired effect on the material's conductivity.

Modelling of the reflectance measurements using the classical theory of exciton-polariton coupling given by Hopfield and Thomas rounded off the chapter. Four different models using dead layers and thin film properties were plotted and compared both the experimental spectra and the bulk values previously acquired for CuCl material. Model 3, which includes the thin-film nature of the sample, was found to give an accurate fit of the excitonic resonances and the shape of the Fabry-Perot oscillations in the reflectance spectra thus providing an accurate determination of the film thickness. The influence of the dead layers on the spectra was found to be extremely minimal having a negligible effect on the resultant plots and requiring an increase to unrealistic levels to become prominent. The polariton dispersion curve for CuCl was also calculated from this fitting model and closely matched previous calculated values with any differences likely stemming from the damping parameter

used in the models as this value showed the largest variance from the bulk sample measurements.

Chapter 6

Conclusions and Further Work

6.1 Conclusions

Recently in DCU the construction of an LPE growth system has been completed. This allows for a more controlled and evenly distributed growth (possibly of single-crystal CuCl) to be deposited onto the target substrate than the physical vapour deposition process. However above 250 ˚C a reaction occurs between the CuCl and Si resulting in the formation of $SiCl_4$ gas and metallic Cu. To avoid this occurrence in the LPE procedure the melting point of the CuCl material must be reduced to ensure the process remains under this critical temperature. One of the ways to achieve this involves the addition of a second salt to the CuCl melt. KCl was chosen as an 80:20 solution of KCl-CuCl has a melting point of less than 200 ˚C. The resulting KCl-CuCl thin films were shown to have an increased level of conductance due to the addition of the K^+ ion and an increase in intensity of the optical properties of the material compared to the CuCl thin films [95]. A similar increase in conductivity is obtained when the CuCl thin films are doped with oxygen to increase the conductivity via p-type doping.

A study of the effects of these processes on the CuCl thin film material formed the background motivation for much of the work in this thesis which was

performed using various methods of characterization to quantify the different parameters and how these processes affect the material.

To summarise the main aspects of the experiments performed during the course of this thesis, textured polycrystalline thin film samples of CuCl were grown on (100) Si substrates chosen for the close lattice matching of the two materials. Room-temperature physical vapour deposition was used to coat the Si substrates to the ideal thickness of 500 nm. For half of each batch of samples, KCl was added to the CuCl mix and the KCl-CuCl samples produced were characterized in tandem with the CuCl samples. Plasma treatment of both sets of samples was then performed at different levels of doping exposure with the characterization process repeated for each step of doping exposure. This ensures any changes in the properties of the material caused by either the KCl addition or the doping procedure will be mapped across different samples and be comparable at identical doping levels.

X-ray diffraction studies show that preferential growth for the undoped CuCl samples occurs in the (111) direction, with diffraction peaks at (220) and (311) orientations clearly distinguishable as well demonstrating the zincblende lattice structure of CuCl. The presence of the (100) CuCl peak was investigated with the φ scan at the (100) position of pure Si and our thin film samples compared. No trace of separate (100) CuCl diffraction was found. The possibility of a perfect lattice-matching with the Si substrate material remains, but it seems extremely unlikely seeing as the CuCl (100) peaks are unable to be distinguished. To differentiate between the polycrystalline CuCl diffraction peaks and those aligned with the (100) Si substrate a series of glancing angle scans were performed. These showed the polycrystalline nature of the CuCl thin films on the Si substrates and a distinct lack of the (100) CuCl peak.

Changes in the structural properties due to the addition of the KCl salt proved to be indistinguishable from the CuCl samples themselves. Doping of the samples produced a decrease in the measured crystallite size determined from each of the diffraction peaks and an increase in the texture factor of the CuCl (100) peak for both CuCl and KCl-CuCl samples. There was an overall decrease in the peak intensity of each of the measured diffraction peaks as doping was increased indicating a deterioration of the structural properties of the material.

A Digital CL camera was used to image the deep level defects within the material, but proper usage of this technique remained restricted due to the poor spatial resolution of the equipment itself. The spectra produced from CL studies of the undoped CuCl samples showed the Z_3 exciton position and the 520 nm defect band as the main features. The ratio of the defect band intensity to the Z_3 exciton intensity was shown to be consistent across multiple samples allowing a clear increase in this ratio to be discerned for the KCl-CuCl samples. This was also the case for the doped samples, with the ratio increasing in a similar but more erratic, style. Examination of the FWHM and maximum intensity of the Z_3 exciton peak fluctuation as doping is increased indicates that there is an ideal region for doping. After an initial decrease in both properties, the FWHM and maximum intensity increases up to around 400 seconds before decreasing once more. This effect was present in both CuCl and KCl-CuCl samples.

EDX imaging allowed us to calculate the atomic percentages for the both the CuCl and KCl-CuCl thin film samples. Expected ratios of Cu, Cl, Si and O were found in the CuCl samples with the addition of trace elements of K and Br found in the KCl-CuCl samples. This shows us that despite the inability of the other methods of characterization to detect the presence of the KCl salt, the deposition of KCl and CuCl

on the same Si substrate has been successful, albeit at lower stoichometry levels than expected based on the ratio of the mixture used (80:20).

PL characterization of the CuCl thin film samples has been performed, including a variable temperature analysis and a calculation of the exciton binding energies. Comparison of the KCl-CuCl PL spectra with the CuCl spectra noted no discernable differences between samples. Analysis of the doped samples of both KCl-CuCl and CuCl showed the formation of an unknown peak at 3.187 eV. This peak production is present only in the CuCl samples, suggesting the K^+ ions added by the KCl salt inhibit the formation of this defect. Similarly the I_1 shoulder measured at 3.182 eV is found to increase in intensity when doped, with the increase present only in the CuCl samples.

Analysis of the reflectance spectra for CuCl and KCl-CuCl showed an increase in the reflected intensity for KCl-CuCl when compared to the CuCl samples. This caused an increase in the overall amplitude of the peaks measured at the exciton positions Z_3 and $Z_{1,2}$ and at each of the Fabry-Perot fringe positions. Oxygen doping caused a decrease in the energy values recorded for each of the exciton positions as well as the measured reflectance value for each of the excitons. This decrease was more gradual, reaching a minimum at 270 seconds which when combined with our previous values for the ideal region of doping suggests doping of 2-3 minutes will retain most of the material's properties whilst having the desired effect on the material's conductivity.

The classical theory of exciton-polariton coupling given by Hopfield and Thomas in conjunction with the Pekar boundary conditions was been successfully used to model the reflectance of the thin film CuCl material. Model 3, which includes the thin-film nature of the sample, was found to give an accurate fit of the excitonic

resonances and the shape of the Fabry-Perot oscillations in the reflectance spectra thus providing an accurate determination of the film thickness. The polariton dispersion curve for CuCl was calculated from this fitting model and closely matched previous calculated values.

The hygroscopic nature of CuCl and the resulting degradation of the thin film features have been examined and compared to the degradation produced by the oxygen doping technique. Both were found to have distinctly unique properties for each of the methods of characterisation employed. To combat degradation caused by atmospheric exposure a capping layer was tested. A common nail varnish (Marie Lluy long-lasting nail varnish) was applied to the CuCl thin film samples and the structural properties monitored using XRD. An increase in the background intensity was recorded, but no distinct peaks were detected showing that the varnish is amorphous in nature and will not interfere with the XRD spectra. This prevented the CuCl samples from deteriorating during the XRD scans as this is the only method of characterization occurring in open atmosphere.

In summary this thesis has ascertained the material properties and reproducibility of these for CuCl thin film samples and investigated the effect on these values of doping with both KCl during the deposition and oxygen via plasma treatment on these. Minimal differences in the material properties were observed by the addition of the KCl salt with a notable increase in the clarity of the reflectance spectra. There appears to be no disadvantage to this doping process. The oxygen doping process however was shown to cause the deterioration each of the materials properties once an exposure level of over 2-3 minutes has been passed. As long as the doping exposure remains within this limit the effect on the material properties is sufficiently minimised to grant the conductivity benefits without the negative effects becoming too damaging.

6.2 Further Work

Finally there are several outstanding questions that this research has been unable to answer. A pair of unidentified PL peaks was detected during the doping process. The samples could be tested in an alternative PL setup using a lower wavelength laser to see if the emergence of these peaks as doping is increased is altered.

The LPE system discussed at the start of this section failed to produce deposition onto the Si substrate due to adhesion problems with the Si layer. However a small number of non-uniform samples were successfully produced and characterised with large quantities of the K_2CuCl_3 compound detected [49]. If these samples could be reproduced, the effect of doping on the higher levels of KCl within the CuCl thin films could be investigated with the behaviour compared to the KCl samples. Also, the nature of the vapour phase epitaxy deposition technique prevents films being deposited with the exact same stoichometry repeatedly, with slight differences in the material thickness present depending on the position of the Si substrates within the deposition equipment. Ideally the LPE issues could be resolved and single-crystal CuCl samples produced but there are other alternatives. Molecular beam epitaxy (MBE) and atomic layer deposition (ALD) also deposit compound semiconductor films with repeatable stoichometry. These methods also allow greater control over the spread of doping within the thin films resulting in a uniform distribution of the dopant within the volume deposited.

KCl isn't the only possible dopant for CuCl to lower the melting point; other chlorides such as both $SrCl_2$ and $BaCl_2$ could be explored in the same manner as the KCl salt throughout this work. Alternative copper halides could also be explored, with

positive initial results recorded for thin films of CuBr [127]. Choosing a different copper halide to explore in this manner would also increase the stability of the samples as CuCl is the least stable of all the copper halides. The characterisation methods detailed in this thesis would be equally effective when applied to CuBr, especially the reflectance modelling as CuBr is also a two-band exciton model containing the Z_3 and $Z_{1,2}$ excitons [15].

References

1. S. Nakamura, G.F., *The Blue Laser Diode: GaN based Light Emitters and Lasers.* Springer, Berlin, 1997.
2. Itaya, K., et al., *Room temperature pulsed operation of nitride based multi-quantum-well laser diodes with cleaved facets on conventional C-face sapphire substrates.* Japanese Journal of Applied Physics Part 2-Letters, 1996. **35**(10B): p. L1315-L1317.
3. Karu, T., *Primary and secondary mechanisms of action of visible to near-IR radiation on cells.* Journal of Photochemistry and Photobiology B-Biology, 1999. **49**(1): p. 1-17.
4. Deppe, H. and H.H. Horch, *Laser applications in oral surgery and implant dentistry.* Lasers in Medical Science, 2007. **22**(4): p. 217-221.
5. Yang, Q., et al., *Enhancing Light Emission of ZnO Microwire-Based Diodes by Piezo-Phototronic Effect.* Nano Letters, 2011. **11**(9): p. 4012-4017.
6. Zhao, L.B., et al., *Optical Defect in GaN-Based Laser Diodes Detected by Cathodoluminescence.* Chinese Physics Letters, 2008. **25**: p. 4342-4344.
7. Ambacher, O., *Growth and applications of Group III-nitrides.* Journal of Physics D: Applied Physics, 1998. **31**: p. 2653-2710.
8. Kapolnek, D., et al., *Structural evolution in epitaxial metalorganic chemical vapor deposition grown GaN films on sapphire.* Applied Physics Letters, 1995. **67**: p. 1541-1543.
9. Ning, X.J., et al., *Growth defects in GaN films on sapphire: The probable origin of threading dislocations.* Journal of Materials Research, 1996. **11**: p. 580-592.
10. Gibart, P., *Metal organic vapour phase epitaxy of GaN and lateral overgrowth.* Reports on Progress in Physics, 2004. **67**: p. 667-715.
11. Nakamura, S., et al., *InGaN/GaN/AlGaN-based laser diodes with modulation-doped strained-layer superlattices grown on an epitaxially laterally overgrown GaN substrate.* Applied Physics Letters, 1998. **72**: p. 211-213.
12. Davis, R.F., et al., *Pendeo-epitaxial growth of thin films of gallium nitride and related materials and their characterization.* Journal of Crystal Growth, 2001. **225**: p. 134-140.
13. Usui, A., et al., *Thick GaN epitaxial growth with low dislocation density by hydride vapor phase epitaxy.* Japanese Journal of Applied Physics Part 2-Letters, 1997. **36**: p. L899-L902.
14. Marchand, H., et al., *Microstructure of GaN laterally overgrown by metalorganic chemical vapor deposition.* Applied Physics Letters, 1998. **73**: p. 747-749.
15. Madelung, O., *Semiconductors: Data Handbook.* Springer, 2003: p. 911-914.
16. Pearton, S.J., et al., *Recent progress in processing and properties of ZnO.* Progress in Materials Science, 2005. **50**: p. 293-340.
17. Lee, J.-B., et al., *Effects of lattice mismatches in ZnO/substrate structures on the orientations of ZnO films and characteristics of SAW devices.* Thin Solid Films, 2004. **447-448**: p. 296-301.
18. Kumar, A., M. Kumar, and B.P. Singh, *Fabrication and characterization of magnetron sputtered arsenic doped p-type ZnO epitaxial thin films.* Applied Surface Science, 2010. **256**: p. 7200-7203.
19. Sterzer, F., S. Miniter, and D. Blattner, *Cuprous chloride light modulators.* Journal of the Optical Society of America, 1964. **54**: p. 62-68.
20. Shaklee, K.L., R.F. Leheny, and R.E. Nahory, *Stimulated Emission from the Excitonic Molecules in CuCl.* Physical Review Letters, 1971. **26**: p. 888-891.

21. Doran, N.J. and A.M. Woolley, *The band structure of CuCl.* Journal of Physics C-Solid State Physics, 1979. **12**: p. L321-L324.
22. Kleinman, L. and K. Mednick, *Energy bands and effective masses of CuCl.* Physical Review B, 1979. **20**: p. 2487-2490.
23. Ostertag, E., *Three-Branch Polariton Dispersion Curve in CuCl.* Physical Review Letters, 1980. **45**: p. 372-375.
24. Westphal, D. and A. Goldmann, *Valence band structure of CuCl: an angle-resolved photoemission study.* Journal of Physics C: Solid State Physics, 1982. **15**: p. 6661-6671.
25. http://apps.isiknowledge.com, t.f.I.W.o.K.
26. Nakayama, M., H. Ichida, and H. Nishimura, *Bound-biexciton photoluminescence in CuCl thin films grown by vacuum deposition.* Journal of Physics-Condensed Matter, 1999. **11**: p. 7653-7662.
27. Heireche, H., et al., *Electronic and optical properties of copper halides mixed crystal* $CuCl_{1-x}Br_x$. Journal of Physics and Chemistry of Solids, 1998. **59**: p. 997-1007.
28. Wyncke, B. and F. Brehat, *Far-infrared reflectivity spectroscopy of cuprous chloride, cuprous bromide and their mixed crystals.* Journal of Physics-Condensed Matter, 2000. **12**: p. 3461-3484.
29. Kurisu, H., et al., *Exciton and biexciton properties of CuCl microcrystals in an* SiO_2 *matrix prepared by sputtering method.* Journal of Luminescence, 2000. **87-89**: p. 390-392.
30. Sasai, J., K. Tanaka, and K. Hirao, *Optical second-order nonlinearity of poled borosilicate glass containing CuCl.* Journal of Applied Physics, 2000. **88**: p. 2200-2204.
31. Ikezawa, M. and Y. Masumoto, *Observation of homogeneous broadening of confined excitons in CuCl quantum dots.* Journal of Luminescence, 2000. **87-89**: p. 482-484.
32. Masumoto, Y. and S. Ogasawara, *Photostimulated luminescence of quantum dots.* Journal of Luminescence, 2000. **87-89**: p. 360-362.
33. Ekimov, A.I., A.L. Efros, and A.A. Onushchenko, *Quantum size effect in semiconductor microcrystals.* Solid State Communications, 1985. **56**: p. 921-924.
34. Itoh, T., Y. Iwabuchi, and M. Kataoka, *Study on the size and shape of CuCl microcrytals embedded in alkali-chloride matrices and their correlation with exciton confinement.* Physica Status Solidi B-Basic Research, 1988. **145**: p. 567-577.
35. Masumoto, Y., T. Wamura, and A. Iwaki, *Homogeneous width of exciton absorption spectra in CuCl microcrystals.* Applied Physics Letters, 1989. **55**: p. 2535-2537.
36. Nakamura, A., H. Yamada, and T. Tokizaki, *Size-dependent radiative decay of excitons in CuCl semiconducting quantum spheres embedded in glasses.* Physical Review B, 1989. **40**: p. 8585-8588.
37. Yanase, A. and Y. Segawa, *Nucleation and morphology evolution in the epitaxial growth of CuCl on MgO(001) and CaF2(111).* Surface Science, 1996. **357**: p. 885-890.
38. Guo, Q., L. Gui, and N. Wu, *CuCl growth on the reconstructed surface of (0001) haematite.* Applied Surface Science, 1996. **99**: p. 229-235.
39. Yanase, A. and Y. Segawa, *Two different in-plane orientations in the growths of cuprous halides on MgO(001).* Surface Science, 1995. **329**: p. 219-226.
40. Nishida, N., K. Saiki, and A. Koma, *Heteroepitaxy of CuCl on GaAs and Si substrates.* Surface Science, 1995. **324**: p. 149-158.
41. Inoue, T., M. Kuriyama, and H. Komatsu, *Growth of CuCl single-crystals by the top seeded solution growth method.* Journal of Crystal Growth, 1991. **112**: p. 531-538.
42. J. Acker, S.K., K.M. Lewis, K. Bohmhammel, *The reactivity in the system CuCl-Si related to the activation of silicon in the Direct Synthesis.* Silicon Chemistry, 2003. **2**: p. 195-206.

43. Oliveira, L., et al., *Coupled Pairs of Cu^+ -OCN^- in KCl Studied by Optical Absorption and Thermally Stimulated Depolarization Current.* Physica Status Solidi B-Basic Research, 1992. **171**: p. 141-151.
44. Oliveira, L. and M.S. Li, *Off-center effect of Cu+-doped KCl films studied by optical absorption and thermally stimulated depolarization current.* Thin Solid Films, 1995. **268**: p. 30-34.
45. Oliveira, L., et al., *Optical and Structural Characterizations of Cu^+ Doped KCl Films.* Thin Solid Films, 1994. **250**: p. 273-278.
46. Christensen, E., R.W. Berg, and J.H. Vonbarner, *Copper(I) complex-formation in chloride melts: Raman-spectroscopic and cryoscopic study.* Polyhedron, 1989. **8**: p. 325-332.
47. O'Reilly, L., et al., *Growth and characterisation of wide-bandgap, I-VII optoelectronic materials on silicon.* Journal of Materials Science-Materials in Electronics, 2005. **16**: p. 415-419.
48. O'Reilly, L., et al., *Impact on structural, optical and electrical properties of CuCl by incorporation of Zn for n-type doping.* Journal of Crystal Growth, 2006. **287**: p. 139-144.
49. A. Cowley, et al., *UV emission on a Si substrate: Optical and structural properties of gamma-CuCl on Si grown using liquid phase epitaxy techniques.* physica status solidi (a), 2009. **206**: p. 923-926.
50. Peter Y. Yu, M.C., *Fundamentals of Semiconductors.* Springer, 2005: p. 22.
51. Barron, T.H.K., J.A. Birch, and G.K. White, *Thermal expansion and heat capacity of cuprous chloride at low temperatures.* Journal of Physics C: Solid State Physics, 1977. **10**: p. 1617-1625.
52. Yasumasa, O. and T. Yozo, *Precise determination of lattice parameter and thermal expansion coefficient of silicon between 300 and 1500 K.* Journal of Applied Physics, 1984. **56**: p. 314-320.
53. Boyce, J.B. and J.C. Mikkelsen, *On the nature of molten CuCl.* Journal of Physics C: Solid State Physics, 1977. **10**: p. L41-L43.
54. Sugawara, M., *Model for lasing oscillation due to bi-excitons and localized bi-excitons in wide-gap semiconductor quantum wells.* Japanese Journal of Applied Physics Part 1-Regular Papers Short Notes & Review Papers, 1996. **35**: p. 124-131.
55. Edamatsu, K., et al., *Generation of ultraviolet entangled photons in a semiconductor.* Nature, 2004. **431**: p. 167-170.
56. Schwab, C. and A. Goltzene, *Cuprous Halides.* Progress in Crystal Growth and Characterization of Materials, 1982. **5**: p. 233-276.
57. Goldmann, A., et al., *Density of valence states of CuCl, CuBr, CuI and AgI.* Physical Review B, 1974. **10**: p. 4388-4402.
58. Ferhat, M., et al., *The electronic structure of CuCl.* Computational Materials Science, 2001. **20**: p. 267-274.
59. Göbel, A., et al., *Effects of the isotopic composition on the fundamental gap of CuCl.* Physical Review B, 1998. **57**: p. 15183-15190.
60. Wei, S.H. and A. Zunger, *Role of metal D-states in II-VI semiconductors.* Physical Review B, 1988. **37**: p. 8958-8981.
61. Cardona, M., *Optical properties of silver and cuprous halides.* Physical Review, 1963. **129**: p. 69-78.
62. Shindo, K., A. Morita, and H. Kamimura, *Spin-orbit coupling in ionic crystals with zincblende and wurtzite structures.* Journal of the Physical Society of Japan, 1965. **20**: p. 2054-2059.

63. Aspnes, D.E. and A.A. Studna, *Chemical etching and cleaning procedures for Si, Ge, and some III-V compound semiconductors.* Applied Physics Letters, 1981. **39**: p. 316-318.
64. Lucas, F.O., *Evaluation of the microstructural, electronic and optoelectronic properties of γ-CuCl thin films and their fabrication on Si substrates.* Thesis (PhD) -- Dublin City University, 2008.
65. O'Reilly, L., *Growth and characterisation of wide-bandgap γ-CuCl on near lattice-matched Si.* Thesis (PhD) -- Dublin City University, 2006.
66. *Long-lasting nail polish.* Marie Lloyd.
67. Hull, S. and D.A. Keen, *Superionic behaviour in copper(I) chloride at high pressures and high temperatures.* Journal of Physics-Condensed Matter, 1996. **8**: p. 6191-6198.
68. Archer, D.G., *Thermodynamic properties of the KCl+H_2O system.* Journal of Physical and Chemical Reference Data, 1999. **28**: p. 1-17.
69. Etter, D.E. and C.J. Wiedenheft, *The study of KCl-CuCl eutectic fused salt as a potential intermediate temperature heat transfer and storage medium.* Solar Energy Materials, 1980. **2**: p. 423-431.
70. Laue, M.v., *International Tables for X-Ray Crystallography, Vol. I. Symmetry Groups.* 1952(Birmingham, England).
71. Ewald, P.P., *Fifty Years of X-Ray Diffraction.* Utrecht: International Union of Crystallography, 1962.
72. B.D Cullity, S.R.S., *Elements of X-Ray Diffraction.* Prentice Hall, 2001.
73. Cullity, B.D., *Elements of x-ray diffraction 2d ed.* Addison-Wesley series in metallurgy and materials Reading, Mass : Addison-Wesley Pub. Co, 1978.
74. Bragg, W.L., *The diffraction of short electromagnetic waves by a crystal.* Proc. Cambridge Philos. Soc., 1913. **17**: p. 43-57.
75. Compton, A.H., *The total reflection of X-rays.* Philosophical Magazine Series 6, 1923. **45**: p. 1121-1131.
76. James, R.W., *The Optical Principles of the Diffraction of X-rays.* G. Bell and Sons LTD, 1948. **The Crystalline State - Vol II**: p. 178.
77. http://it.iucr.org/, *International Tables for X-Ray Crystallography.* Volume D, Physical Properties of Crystals, 2006.
78. Warren, B.E., *X-Ray Diffraction.* Dover Publications Inc., New York, 1990.
79. *Basics of X-Ray Diffraction.* Scintag Incorporated, 1999.
80. Newmark, G.F., I.L. Kuskovsky, and J. H, *Wide Bandgap Light Emitting Materials and Devices.* Wiley-VCH, Germany, 2007.
81. Rashba E I and S.M. D, *Excitons.* North-Holland Publishing Company, 1982. **Volume 2**.
82. Peter Y. Yu, M.C., *Fundamentals of Semiconductors.* Springer, 2005(Third Edition).
83. Kikoin, V.I.S.a.K.A., *Excitons Bound to Impurities of 3D Elements in II-VI Compounds.* Soviet Scientific Reviews, 1989(Harwood Academic Publisher).
84. Lumb, M.D., *Luminescence Spectroscopy.* Academic Press, London, 1978: p. 88.
85. Fryar, J., et al., *Study of exciton-polariton modes in nanocrystalline thin films of ZnO using reflectance spectroscopy.* Nanotechnology, 2005. **16**: p. 2625-2632.
86. Holt, B.Y.a.D., *Cathodoluminescence Microscopy of Inorganic Solids.* 1990.
87. Murr, L.E., *Electron and Ion Microscopy and Microanalysis.* Marcel Dekker Inc, 1982: p. 293.
88. Matsuo, H., et al., *Development of a nanoprobe cathodoluminescence scanning electron microscope.* Journal of Electron Microscopy, 1996. **45**: p. 453-457.
89. Klingshirn, C.F.C.F., *Semiconductor Optics.* Berlin ; London : Springer, 2005., 2005: p. 553.
90. Kanaya, K. and S. Okayama, *Penetration and energy-loss theory of electrons in solid targets.* Journal of Physics D-Applied Physics, 1972. **5**: p. 43-58.

91. Reimer, L., *Scanning electron microscopy : physics of image formation and microanalysis.* Berlin ; New York : Springer, 1998.
92. http://www.gel.usherbrooke.ca/casino/, *CASINO (monte CArlo SImulation of electroN trajectory in sOlids).*
93. *Gatan UK Product Manual.* 2001.
94. Goodhew, P.J., J. Humphreys, and R. Beanland, *Electron Microscopy and Analysis: Third Edition.* Taylor & Francis, 2001(London and New York).
95. Lucas, F.O., et al., *Structural, optical and electrical properties of Co-evaporated CuCl/KCl films.* physica status solidi (c), 2009. **6**: p. S114-S118.
96. *X-Ray Data Booklet.* Lawrence Berkeley National Laboratory: Center for X-ray Optics and Advanced Light Source, 2011.
97. Lu, J., et al., *Synthesis and properties of ZnO films with (100) orientation by SS-CVD.* Applied Surface Science, 2003. **207**: p. 295-299.
98. Bing-Hwai, H., *Calculation and measurement of all (002) multiple diffraction peaks from a (001) silicon wafer.* Journal of Physics D: Applied Physics, 2001. **34**: p. 2469-2474.
99. Danieluk, D., et al., *Optical properties of undoped and oxygen doped CuCl films on silicon substrates.* Journal of Materials Science-Materials in Electronics, 2009. **20**: p. 76-80.
100. Gomathi, N., et al. *Structural and optoelectronic properties of sputtered copper (I) chloride.* 2005. SPIE.
101. Lucas, F.O., et al., *Evaluation of the chemical, electronic and optoelectronic properties of gamma-CuCl thin films and their fabrication on Si substrates.* Journal of Physics D-Applied Physics, 2007. **40**: p. 3461-3467.
102. O'Reilly, L., et al., *Room-temperature ultraviolet luminescence from gamma-CuCl grown on near lattice-matched silicon.* Journal of Applied Physics, 2005. **98**: p. 113512.
103. Souha, H., et al., *Reactivity of Cu_3Si of different genesis towards copper(I) chloride.* Thermochimica Acta, 2000. **351**: p. 71-77.
104. Nakayama, M., et al., *Hot excitons in CuCl and CuBr crystalline thin films grown by vacuum deposition.* Physical Review B, 1997. **55**: p. 10099-10104.
105. Natarajan, G., et al., *Growth of CuCl thin films by magnetron sputtering for ultraviolet optoelectronic applications.* Journal of Applied Physics, 2006. **100**: p. 033520.
106. Wang, Y.G., et al., *Virtual structure in luminescence profile of zinc oxide films causing discrepancy in peak identification.* Journal of Applied Physics, 2006. **100**: p. 114917.
107. Zamoryarskaya, M.V., V.I. Sokolov, and V. Plotnikov, *Cathodoluminescence study of Si/SiO_2 interface structure.* Applied Surface Science, 2004. **234**: p. 214-217.
108. Danieluk, D., et al., *Optical properties of undoped and oxygen doped CuCl films on silicon substrates.* Journal of Materials Science: Materials in Electronics, 2009. **20**: p. 76-80.
109. Knauth, P., Y. Massiani, and M. Pasquinelli, *Semiconductor properties of polycrystalline CuBr by Hall effect and capacitive measurements.* Physica Status Solidi a-Applied Research, 1998. **165**: p. 461-465.
110. Dutta, P.K., et al., *Sensing of carbon monoxide gas in reducing environments.* Sensors and Actuators B: Chemical, 2002. **84**: p. 189-193.
111. Wagner, J.B. and C. Wagner, *Electrical conductivity measurements on cuprous halides.* Journal of Chemical Physics, 1957. **26**: p. 1597-1601.
112. Certier, M., C. Wecker, and S. Nikitine, *Zeeman effect of free and bound excitons in CuCl.* Journal of Physics and Chemistry of Solids, 1969. **30**: p. 2135-2142.
113. Shuh, D.K., et al., *Line-shape and lifetime studies of exciton luminescence from confined CuCl thin films.* Physical Review B, 1991. **44**: p. 5827-5833.

114. Yano, S., et al., *Dynamics of excitons and biexcitons in CuCl nanocrystals embedded in NaCl at 2 K.* Physical Review B, 1997. **55**: p. 1667-1672.
115. Masumoto, Y., T. Kawamura, and K. Era, *Biexciton lasing in CuCl quantum dots.* Applied Physics Letters, 1993. **62**: p. 225-227.
116. Mitra, A., et al., *Optical properties of CuCl films on silicon substrates.* Physica Status Solidi B-Basic Solid State Physics, 2008. **245**: p. 2808-2814.
117. Goto, T., T. Takahashi, and M. Ueta, *Exciton Luminescence of CuCl, CuBr and CuI Single Crystals.* Journal of the Physical Society of Japan, 1968. **24**: p. 314-327.
118. Soltani, M., et al., *Application of the dead-layer model and A.B.C. conditions to the* $Z_{1,2}$ *and* Z_3 *exciton lines in CuCl.* Computational Materials Science, 1995. **4**: p. 263-268.
119. Koda, T., et al., *Effects of Uniaxial Stress on Excitons in CuCl.* Physical Review B, 1972. **5**: p. 705-718.
120. Hopfield, J.J. and D.G. Thomas, *Theoretical and experimental effects of spatial dispersion on optical properties of crystals.* Physical Review, 1963. **132**: p. 563-572.
121. http://www.mathworks.com/.
122. Pekar, S.I., *On the theory of additional electromagnetic waves in crystals in the exciton absorption region.* Soviet Physics-Solid State, 1962. **4**: p. 953-960.
123. Lagois, J., *Dielectric theory of interacting excitonic resonances.* Physical Review B, 1977. **16**: p. 1699-1705.
124. Ivhcenko, E.L., *Excitons.* Editors E I Rashba and M D Sturge Amsterdam: North-Holland, 1982: p. 141-176.
125. Akiyama, H., et al., *Radiative decay and phonon scattering of biexcitons in CuCl.* Physical Review B, 1990. **42**: p. 5621-5625.
126. Tang, Z.K., et al., *Optical Selection Rule and Oscillator Strength of Confined Exciton System in CuCl Thin Films.* Physical Review Letters, 1993. **71**: p. 1431-1434.
127. Cowley, A. and et al., *Electroluminescence of γ-CuBr thin films via vacuum evaporation depositon.* Journal of Physics D: Applied Physics, 2010. **43**: p. 165101.

Appendix: Modelling Program for Reflectance

This appendix contains the code used in MATLAB 5.3 to model the reflectance data in Chapter 5. The code shown is for model 3 with the other models requiring alterations to the matrix section only. Lines marked with "%" are comments. The initial commented section in the main program is an explanation of each of the variables used throughout. The programming format uses a main program called funcfit_tfi_model_3 to setup the initial values and then pol_cal_tfi_model_3 is called and iterated to acheive the best match with our experimental data. Finally the values which provide the best match are sent to ref_disp_tfi_model_3, which is identical to pol_cal_tfi_model_3 except for a section at the end which saves the data to a text file.

(a) Main Program

```
function [fit]=funcfit_tfi_model_3()

B=test_ip(1);

x_data=B(:,1);
y_data=B(:,2);

h_bar=(6.63e-34/(2*3.1415));

%w_l_a=input('What is the longitudinal energy of the A exciton
(eV)....?');
%w_l_b=input('What is the longitudinal energy of the B exciton
(eV)....?');
%a=input('What is the LT splitting of the A exciton(eV)....?');
%b=input('What is the LT splitting of the B exciton(eV)....?');
%c=input('What is the width/damping of the A exciton (eV)....?');
%d=input('What is the width/damping of the B exciton (eV)....?');
%e=input('What is the thickness of the film (nanometres)....?');
%f=input('What is the effective mass of the exciton A (multiples of
electron mass)....?');
%g=input('What is the effective mass of the exciton B (multiples of
electron
%mass)....?');
%h=input('What is the thickness of the dead layer
(nanometres)....?');
```

```
w_l_a=3.2078;
w_l_b=3.286;
a=0.0062617871;
b=0.02290947;
c=0.000008470875;
d=0.005229139;
e=634.1;
f=0.400059634;
g=0.157111;

w_l_a1=(w_l_a*1.6e-19)/h_bar;
w_l_b1=(w_l_b*1.6e-19)/h_bar;

a1=sqrt((a*1.6e-19)/h_bar);
b1=sqrt((b*1.6e-19)/h_bar);
c1=(c*1.6e-19)/h_bar;
d1=(d*1.6e-19)/h_bar;
e1=e*1e-9;
f1=f;
g1=g;
h1=h*1e-9;

param=[a1,b1,c1,d1,e1,f1,g1,h1];

options = optimset('TolFun', 1, 'TolX', 1, 'MaxIter', 100);

best_fit=fminsearch('pol_cal_tfi_model_3',param,options,w_l_a1,w_l_b1
,x_data,y_data);

test=ref_disp_tfi_model_3(param,w_l_a1,w_l_b1,x_data,y_data);

(best_fit(1)^2)*(1/1.6e-19)*h_bar
(best_fit(2)^2)*(1/1.6e-19)*h_bar
best_fit(3)*(1/1.6e-19)*h_bar
best_fit(4)*(1/1.6e-19)*h_bar
best_fit(5)/(1e-9)
best_fit(6)
best_fit(7)
best_fit(8)

w_o_a=w_l_a-((best_fit(1)^2)*h_bar/1.6e-19)
w_o_b=w_l_b-((best_fit(2)^2)*h_bar/1.6e-19)

var(1)=(best_fit(1)^2)*(1/1.6e-19)*h_bar;
var(2)=(best_fit(2)^2)*(1/1.6e-19)*h_bar;
var(3)=best_fit(3)*(1/1.6e-19)*h_bar;
var(4)=best_fit(4)*(1/1.6e-19)*h_bar;
var(5)=best_fit(5)/(1e-9);
var(6)=best_fit(6);
var(7)=best_fit(7);
var(8)=best_fit(8)/(1e-9);

var(9)=w_o_a;
var(10)=w_o_b;

save var_func_cucl_model_2.out var -ASCII
```

(b) Modelling section

```
Function
[error]=ref_disp_tfi_model_3(param,w_l_a,w_l_b,x_data,y_data)

warning off;

spec_range=length(x_data);

h_bar=(6.63e-34/(2*3.1415));
m_elec=9.1e-31;
e_vac=8.85e-12;
c=2.998e8;

del_a=param(1);
del_b=param(2);
gam_a=abs(param(3));
gam_b=abs(param(4));
d=abs(param(5));
m_star_a=abs(param(6));
m_star_b=abs(param(7));
e_rel_inf=3.7;
n_si=5.5;

w_o_a=w_l_a-(del_a^2);
w_o_b=w_l_b-(del_b^2);

m_eff_a=m_star_a*m_elec;
m_eff_b=m_star_b*m_elec;
beta_a=h_bar*w_o_a/m_eff_a;
beta_b=h_bar*w_o_b/m_eff_b;
alpha_a=e_rel_inf*(e_vac/(w_o_a^2))*((w_l_b^2)-(w_o_a^2))*((w_l_a^2)-
(w_o_a^2))/((w_o_b^2)-(w_o_a^2));
alpha_b=e_rel_inf*(e_vac/(w_o_b^2))*((w_l_a^2)-(w_o_b^2))*((w_l_b^2)-
(w_o_b^2))/((w_o_a^2)-(w_o_b^2));
n_inf=sqrt(e_rel_inf);

y1=zeros(spec_range,1);
y2=zeros(spec_range,1);
y3=zeros(spec_range,1);

ref=zeros(spec_range,1);

sum=0;

for count=1:spec_range

   w=(x_data(count)*1.6e-19)/h_bar;

   term1=(w_o_a^2)-(w^2)-(i*w*gam_a);
   term2=(w_o_b^2)-(w^2)-(i*w*gam_b);

   coeff=[beta_b*beta_a*(c^2)/(w^2);
      - (e_rel_inf*beta_b*beta_a)
+(term2*beta_a*(c^2)/(w^2))+(term1*beta_b*(c^2)/(w^2));
      (term1*term2*(c^2)/(w^2))-(beta_b*e_rel_inf*term1)-
(beta_a*e_rel_inf*term2)-(alpha_a*(w_o_a^2)*beta_b/e_vac)-
(alpha_b*(w_o_b^2)*beta_a/e_vac);
```

```
      -(e_rel_inf*term1*term2)-(alpha_a*(w_o_a^2)*term2/e_vac)-
(alpha_b*(w_o_b^2)*term1/e_vac)];

   k_values=sqrt(roots(coeff));

   if imag(k_values(1))>0
      k_values(1)=-k_values(1);
   else
   end

   if imag(k_values(2))>0
      k_values(2)=-k_values(2);
   else
   end

   if imag(k_values(3))>0
      k_values(3)=-k_values(3);
   else
   end

   n_a=k_values(1)*c/w;
   n_b=k_values(2)*c/w;
   n_c=k_values(3)*c/w;

   d_a=exp(i*n_a*w*d/c);
   d_b=exp(i*n_b*w*d/c);
   d_c=exp(i*n_c*w*d/c);

   d_a_1=exp(-i*n_a*w*d/c);
   d_b_1=exp(-i*n_b*w*d/c);
   d_c_1=exp(-i*n_c*w*d/c);

   a_a=(alpha_a*(w_o_a^2)/e_vac)/((w_o_a^2)-(w^2)-
(i*w*gam_a)+(beta_a*(w^2)*(n_a^2)/(c^2)));
   a_b=(alpha_a*(w_o_a^2)/e_vac)/((w_o_a^2)-(w^2)-
(i*w*gam_a)+(beta_a*(w^2)*(n_b^2)/(c^2)));
   a_c=(alpha_a*(w_o_a^2)/e_vac)/((w_o_a^2)-(w^2)-
(i*w*gam_a)+(beta_a*(w^2)*(n_c^2)/(c^2)));

   b_a=(alpha_b*(w_o_b^2)/e_vac)/((w_o_b^2)-(w^2)-
(i*w*gam_b)+(beta_b*(w^2)*(n_a^2)/(c^2)));
   b_b=(alpha_b*(w_o_b^2)/e_vac)/((w_o_b^2)-(w^2)-
(i*w*gam_b)+(beta_b*(w^2)*(n_b^2)/(c^2)));
   b_c=(alpha_b*(w_o_b^2)/e_vac)/((w_o_b^2)-(w^2)-
(i*w*gam_b)+(beta_b*(w^2)*(n_c^2)/(c^2)));


   mat=[-1,1,1,1,1,1,1,0;
      1,n_a,n_b,n_c,-n_a,-n_b,-n_c,0;
      0,d_a,d_b,d_c,d_a_1,d_b_1,d_c_1,-1;
      0,n_a*d_a,n_b*d_b,n_c*d_c,-n_a*d_a_1,-n_b*d_b_1,-n_c*d_c_1,-
n_si;
      0,a_a,a_b,a_c,a_a,a_b,a_c,0;
      0,b_a,b_b,b_c,b_a,b_b,b_c,0;
      0,d_a*a_a,d_b*a_b,d_c*a_c,d_a_1*a_a,d_b_1*a_b,d_c_1*a_c,0;
      0,d_a*b_a,d_b*b_b,d_c*b_c,d_a_1*b_a,d_b_1*b_b,d_c_1*b_c,0];

   v=[1;1;0;0;0;0;0;0];
   inmat=inv(mat);

   v1=inmat*v;
```

```
   x_data(count);

   r1=v1(1);

   ref(count)=((abs(r1))^2);

   diff=(ref(count)-y_data(count))^2;
   sum=sum+diff;

end

error=sum/spec_range;

plot(x_data,ref,x_data,y_data);

save refdata_model_3.out ref -ASCII
```